MEASUREMENT AND INTERPRETATION OF TRAVEL-TIME SHIFTS IN THE CONTEXT OF TIME-DISTANCE HELIOSEISMIC DETECTION OF MERIDIONAL FLOW

A DISSERTATION
SUBMITTED TO THE DEPARTMENT OF ELECTRICAL ENGINEERING
AND THE COMMITTEE ON GRADUATE STUDIES
OF STANFORD UNIVERSITY
IN PARTIAL FULFILLMENT OF THE REQUIREMENTS
FOR THE DEGREE OF
DOCTOR OF PHILOSOPHY

Sudeepto Chakraborty
March 2015

This dissertation is online at: http://purl.stanford.edu/js379rb8975

I certify that I have read this dissertation and that, in my opinion, it is fully adequate in scope and quality as a dissertation for the degree of Doctor of Philosophy.

Philip Scherrer, Primary Adviser

I certify that I have read this dissertation and that, in my opinion, it is fully adequate in scope and quality as a dissertation for the degree of Doctor of Philosophy.

Howard Zebker

I certify that I have read this dissertation and that, in my opinion, it is fully adequate in scope and quality as a dissertation for the degree of Doctor of Philosophy.

Thomas Duvall

Approved for the Stanford University Committee on Graduate Studies.

Patricia J. Gumport, Vice Provost for Graduate Education

This signature page was generated electronically upon submission of this dissertation in electronic format. An original signed hard copy of the signature page is on file in University Archives.

Abstract

The role of meridional circulation in maintaining the dynamo and differential rotation in the Sun is not well understood and is currently under scrutiny. Traditional flux-transport dynamo models have posited a single-cell meridional circulation with poleward flow at the photosphere and equatorward flow near the base of the convection zone. However, recent investigations seem to be revealing a discrepant picture of meridional circulation which is at least double-celled in the radial direction. In this scenario it is paramount that we continue to use and develop helioseismology in order to accurately determine the structure of meridional circulation.

Helioseismology is a powerful tool for studying the Sun. It uses the photospherically visible aspect of (acoustic, surface-gravity) waves, that propagate and interfere throughout the Sun to form standing oscillation modes, to probe the subsurface structure and flows. This work employs time-distance helioseismology which is based on measuring the travel times of wave packets moving between distinct points on the solar surface. The travel-time shift calculated from the difference in the travel times of counter-propagating waves between a pair of points on the photosphere yields information about flows on the surface and interior of the Sun. In this work time-distance techniques are applied on artificial and solar velocity images to detect meridional flow induced travel-time shift signals.

For forward modeling purposes, artificial datacubes are constructed by embedding various meridional circulation models in three-dimensional acoustic wave propagation simulators, which is then analyzed by time-distance techniques. The resulting measurements are used to discuss the interpretation of travel-time shifts in the ray-theoretic or ray approximation. The common-midpoint and the full deep-focus time-distance techniques are applied on phase-speed filtered simulated velocity data. The results show that the full deep-focus techniques yield a higher signal-to-noise

ratio and that travel-time shifts measured from the time-distance analysis of simulated data, in general, deviate quantitatively from ray-theoretic travel-time shifts. The study also characterizes the dependence of ray-theoretic travel-time shifts on different background models.

Recent work has revealed a systematic "center-to-limb" variation in the measured travel times, which must be corrected to accurately infer meridional flow velocity in the Sun. It has been proposed that the "center-to-limb" effect can be partly explained by the asymmetrical nature of solar granulation which imparts a heliocentric angle dependent phase shift on the oscillation modes. In this work spherical harmonic transform techniques are applied on Dopplergrams from the Helioseismic and Magnetic Imager (HMI) instrument aboard the Solar Dynamics Observatory (SDO) spacecraft, to reconstruct velocity images of a subset of acoustic modes relevant to meridional flow. Non-standard deep-focus time-distance techniques are applied on the reconstructed images, and the resulting travel-time shifts are compared to a simple bilinear center-to-limb phase-shift function in order to characterize the "center-to-limb" effect in the solar convection zone.

Acknowledgements

This has been a humbling and enriching experience, and certainly calls for an outpouring of gratitude.

I am grateful to P. H. Scherrer for welcoming me into the Solar Physics group at Stanford, and guiding me with a knowing and unforced hand towards the completion of this doctoral work. His vast knowledge, and not just of solar physics, his practical rationality, his compassionate and able leadership are qualities that I will always aspire to.

I would like to thank T. L. Duvall, Jr. (2014 Hale Prize winner), for his infinite patience, for his insightful supervision and collaboration, for the reasoned and lucid discussions, for all the IRAF tasks that facilitated my work, for being open to my ideas and the paths that I wanted to pursue, for nurturing my curiosity and creativity, and for transmitting his knowledge of spherical geometry, signal processing, and helioseismic analysis which I apply and present in this dissertation. I am in awe of his firm, yet gentle discipline that I hope in time to be able to cultivate.

S. M. Hanasoge and T. Hartlep provided the simulation data used in this work. S. Kholikov provided the spherical harmonic reconstruction code, and T. P. Larson taught me how to use it (along with other DRMS tricks). P. H. Scherrer, K.-C. Chu, and A. Amezcua provided crucial help with computational and database resources. The many illuminating discussions with them shaped this work in important ways. I am privileged to have them as collaborators in my research endeavors.

I am beholden to D. O. Gough for imparting his knowledge of the mathematics of stellar oscillations and ray theory to me during his summer visits at Stanford. I am also thankful to A. G. Kosovichev for his guidance with some of the theoretical subtleties in disparate topics in stellar and solar physics.

J. T. Hoeksema made my work at Wilcox Solar Observatory (WSO) less cumbersome during crunch time, and his words of wisdom made the writing of this dissertation a practical and feasible enterprise, rather than an ambitious and unattainable one. S. Ilonidis provided me all the raw materials of his dissertation to use whatever I needed to write mine. I owe a debt of gratitude to both of them for making my life easier.

Besides help with research and dissertation work there were significant acts of kindness during my time at Stanford. Tim Larson introduced me to the Solar Physics group, and to the possibility of making WSO my home, which it has been for the last 5.5 years. Xudong Sun granted my request to be a co-resident observer at WSO at a critical time. My friend Mimm Patterson "had my back" during my time of illness. Amy Duncan, the EE Graduate Degree Progress Officer, was compassionate and accommodating when I needed to extend my Ph.D. candidacy. Nancy Christiansen procured the funds for a new vehicle to replace the WSO minivan. Haruko Makitani brought me leftover cake after missed parties. The lady at DMV who released the title of my car to me after I had just arrived in the Bay Area, even though I lacked the proper documents. There were others, unnamed here, but not unacknowledged or forgotten.

I would be negligent if I did not express my gratitude to the San Francisco Bay Area for its wonderful climate and its rich diversity, to Stanford University for opening its fount of knowledge to me, to the National Aeronautics and Space Administration for providing the funding through the HMI grant that made my education and research work possible, to the Solar Physics community for all the exotic conference trips and the "wild" parties, and to Stanford Health Care for increasing my life expectancy.

Last on the list, but certainly not the least, my mother, an understated force of nature who made this life possible...to her I dedicate this work.

Contents

Abstract **v**

Acknowledgements **vii**

1 Introduction **1**

1.1 Meridional Circulation: Observations 3

1.1.1 Surface Observations 3

1.1.2 Global Helioseismic Inferences 5

1.1.3 Local Helioseismic Inferences 7

1.2 Meridional Circulation: Simulations 9

1.2.1 Mean-Field Hydrodynamical Models 10

1.2.2 Flux-Transport Dynamo Models 14

1.2.3 Three-dimensional Global Numerical Simulations 14

1.3 Dissertation Outline 16

2 Time-Distance Helioseismology **19**

2.1 Solar Oscillations 20

2.1.1 Normal Modes of Oscillation 22

2.1.2 Properties of Acoustic Modes 24

2.2 Computing Travel Times 27

2.2.1 Phase-Speed Filtering 27

2.2.2 Cross-Covariance Function 31

2.2.3 Deep-Focus Geometry 33

2.2.4 Gabor-Wavelet Fitting 37

2.2.5 Ray-Theoretic Forward Model 38

3 Forward Modeling with Ray Theory and Simulations **40**
3.1 Acoustic Wave Propagation Simulations 41
3.2 Ray-Theoretic Analysis and Results 43
3.2.1 Meridional Flow Model 44
3.2.2 Deep-Focus Geometry 47
3.2.3 Acoustic Cut-off Frequency 48
3.2.4 Convective Stability 50
3.2.5 Discussion 52
3.3 Time-Distance Analysis and Results 55
3.3.1 Common-Midpoint vs. Full Deep-Focus Technique 56
3.3.2 Meridional Travel-Time Shifts 58
3.3.3 Discussion 62

4 Computing Travel Times with HMI Data **64**
4.1 Helioseismic and Magnetic Imager 65
4.1.1 Introduction 65
4.1.2 HMI Instrument 67
4.1.3 HMI Data Products 69
4.2 Spherical Harmonic Reconstruction 70
4.2.1 Introduction 70
4.2.2 Reconstruction Code Validation 72
4.2.3 HMI Data Reconstruction 73
4.3 The "Center-to-Limb" Effect 74
4.3.1 Background 74
4.3.2 Constant Chord-length Geometry 77
4.3.3 Time-Distance Analysis and Results 82
4.3.4 Discussion 87
4.3.5 Postscript: Center-to-Limb Phase Shift 90

5 Concluding Remarks **94**
5.1 Summary 94
5.2 Strategies 95
5.2.1 Noisy Travel Times 96
5.2.2 From Rays to Waves 96
5.2.3 Systematic Errors 97

5.2.4 Inverse Problem 99
5.2.5 Interpretation Revisited 99

A Colatitudinal and Radial Travel-Time Shifts **101**

Bibliography **103**

List of Figures

1.1 Surface meridional flow with various measurement techniques 5
1.2 Global helioseismic inference of meridional flow 6
1.3 Single- vs. double-cell meridional circulation 8
1.4 Double-cell meridional flow profile 8
1.5 A model based on mean-field hydrodynamics 10
1.6 Parametrized rotation and double-cell meridional circulation 11
1.7 Mean-field rotation and double-cell meridional circulation 12
1.8 Flux-transport dynamo with multi-cell meridional circulation 13
1.9 Global hydrodynamic and MHD simulation 15

2.1 Solar oscillations with high-resolution MDI Dopplergram 21
2.2 Power spectrum of solar oscillations 23
2.3 Propagation of acoustic rays in the solar interior 26
2.4 Phase-speed filtering of simulation data 29
2.5 Phase-speed filtering of HMI data 30
2.6 Time-distance diagram and example ray paths 31
2.7 Lower turning point vs. single-skip distance 32
2.8 A simple deep-focus geometry 34
2.9 A realistic example of full deep-focus geometry 35
2.10 Shifting and averaging of cross-covariances for range of Δ 36
2.11 Gabor-wavelet fit to a cross-covariance function 37

3.1 Power spectra of wave simulation with meridional flow 42
3.2 Single-cell meridional flow model (R06) and profile 45
3.3 Single-cell meridional flow model (BC88) and profile 45
3.4 Radial double-cell meridional flow model (JB07) and profile 46
3.5 Ray-theoretic $\delta\tau_{\rm ns}$ dependence on meridional flow models 46

3.6 Ray-theoretic $\delta\tau_{\rm ns}$ dependence on deep-focus geometry 47
3.7 Ray-theoretic $\delta\tau_{\rm ns}$ dependence on acoustic cut-off frequency 49
3.8 Ray theoretic $\delta\tau_{\rm ns}$ dependence on background for R06 flow model . . 50
3.9 Ray-theoretic $\delta\tau_{\rm ns}$ dependence on background for JB07 flow model . . 51
3.10 Ray-theoretic $\delta\tau_{\rm ns}$ dependence on depth of stagnation point 52
3.11 Travel-time shift dependence on background for near-surface flow . . 54
3.12 Common-midpoint technique applied on HZK13 simulation 57
3.13 5-pairs deep-focus technique applied on HZK13 simulation 57
3.14 9-pairs deep-focus technique applied on HZK13 simulation 58
3.15 Travel-time shifts for R06 meridional flow model 59
3.16 Travel-time shifts for BC88 meridional flow model 60
3.17 Travel-time shifts for JB07 meridional flow model 61

4.1 HMI and SDO 66
4.2 Schematic of HMI optical layout 68
4.3 HMI wavelength tuning-position profiles 68
4.4 Schematic flow diagram for HMI pipeline 70
4.5 Spherical harmonic reconstruction tests on MDI data 72
4.6 Spherical harmonic reconstruction of HMI data 73
4.7 Center-to-limb correction in Zhao et al. (2012) 75
4.8 Center-to-limb correction in Zhao et al. (2013) 76
4.9 Time-distance geometry of Zhao et al. (2012, 2013) 78
4.10 Constant chord-length (CCL) geometry 79
4.11 CCL geometry on HLD06/R06 simulation data 81
4.12 $\delta\tau_{\rm ns}$ and $\delta\tau_{\rm we}$ from HMI data 84
4.13 Corrected vs. uncorrected $\delta\tau_{\rm sn}$ and the correction $\delta\tau_{\rm ew}$ 85
4.14 $\delta\tau_{\rm ns}$ at $\pm45^\circ$ longitudes from HMI data 86
4.15 $\delta\tau_{\rm we}$ at $\pm45^\circ$ latitudes from HMI data 87
4.16 Comparison of $\delta\tau_{\rm ns}$ with standard and non-standard geometry 89
4.17 Heliocentric angle dependent phase shift 91
4.18 Center-to-limb phase shift model 92
4.19 Center-to-limb model vs. "center-to-limb" effect in HMI data 93

Chapter 1

Introduction

This dissertation is about the *measurement* and *interpretation* of *travel times*, or rather, the non-vanishing *difference* between the travel times of counter-propagating solar acoustic waves between a pair of photospheric locations, in the presence of flows, specifically, *meridional flows*. In the preceding sentence the interpretation is already present—the measured quantities, the "travel time" and the "travel time difference" are due to certain well-defined wave and flow phenomena. In what sense is this an interpretation? What is it that is being interpreted? It is the measurement that is being interpreted. It is being interpreted as a "travel time" or a "travel time difference", as the case may be. How is this an interpretation? Measurements in physical science are measurements of a physical quantity; in this case the measured quantity is the travel time. It would be just that simple if it were merely a matter of opportunely placed wave detectors and clocks.

In *time-distance helioseismology* (Duvall et al., 1993; Kosovichev and Duvall, 1997), the measurement method of choice in this dissertation, the situation is complicated by a sequence of operations that is performed on a starting measured quantity—for example, temporal cross-correlation of Doppler velocity on the photosphere of the Sun, followed by curve-fitting to obtain the *time lag* at which the cross-correlation function peaks. An intermediate measured quantity is this time lag. It has units of time, but how does it relate to travel time? The time lag is *interpreted* to be a measure of the travel time of acoustic wave packets, with a well-defined trajectory, between the cross-correlated locations on the photosphere. The interpretation goes further: the time lag and the wave packet travel time are in fact identical (cf. Duvall et al., 1993; D'Silva and Duvall, 1995; D'Silva, 1996). Further interpretations follow

from this assumption: the ray-theoretic interpretation, the plane wave interpretation in the first Born approximation, etc. These subsequent interpretations permit certain theoretical constructs which are *perturbed* in well-established mathematical ways to allow the measurement or *inference* of the perturbation of interest, in this case, the flow velocity of meridional circulation cells. This dissertation investigates interpretation of travel-time shifts in the context of measuring meridional flow velocity in the solar convection zone by (i) forward modeling time-distance measurements of acoustic wave simulations in the ray approximation, and (ii) by studying the systematic "center-to-limb" phase variations in time-distance measurements of Helioseismic and Magnetic Imager (HMI) Doppler velocity data.

Meridional circulation (large-scale circulating flows along meridional planes) is believed to arise in the solar convection zone due to complex nonlinear interactions between turbulent convection, rotation and magnetism (Rempel, 2006; Miesch and Toomre, 2009). In mean-field hydrodynamic models (magnetic fields absent), meridional circulation arises with differential rotation due to anisotropic transport of angular momentum and energy resulting from the interaction between rotation and convective turbulence (Kitchatinov, 2013). In this dissertation the term *meridional circulation* is used to denote the complete (single or multiple) circulating structure(s), whereas *meridional flow* is used to denote the flow in meridional planes at particular locations. However, the term *meridional flow model* may also be read as *meridional circulation model*.

Surface meridional flow plays a causal role in surface flux-transport models (Wang et al., 1989), in the poleward transport of magnetic flux, the concentration of polar fields, polar field reversal, and the quasi-rigid rotation, despite the differential rotation, of the streams of flux spreading poleward from the activity belts. Meridional circulation is invoked in flux-transport models of the solar dynamo (flux-transport dynamo models, as distinct from surface flux-transport models) to explain the 22-year solar magnetic activity cycle (Choudhuri et al., 1995). It is one of the transport mechanisms, along with dynamo waves, convective turbulent diffusion, turbulent pumping, and magnetic buoyancy, that is believed to give rise to migrating magnetic structures. These migrating phenomena include the observed poleward movement of the trailing part of bipolar magnetic regions (while simultaneously undergoing turbulent diffusive decay), leading to the polarity reversal of the polar/poloidal field at solar-cycle minima, and also the equatorward migration of active region formation (Spörer's

law) during the course of a solar cycle. In Dikpati and Gilman (2006) a single-cell meridional circulation is described as a "conveyor belt" transporting the magnetic flux in the solar convection zone. Observations and modeling seem to indicate that the structure and strength of the meridional flow determine the strength of the Sun's polar magnetic field, and the period and intensity of current and future solar cycles (e.g., Hathaway et al., 2003; Nandy et al., 2011).

A brief survey is provided of the observations of meridional flow structure in Section 1.1. This section also highlights the importance of *helioseismology* (study of the Sun, especially the interior, using solar oscillation modes) in determining subsurface structures and processes (e.g., meridional circulation) at solar depths opaque to conventional optics. Select simulation results are covered in Section 1.2 to provide a theoretical reference for the observations. The introduction is concluded with an outline of this dissertation (Section 1.3).

1.1 Meridional Circulation: Observations

Doppler data and the tracking of discernible features allow the measurement of surface meridional flow on the Sun. Helioseismology provides an alternative to the surface measurements, and additionally, has the capability of probing flows below the photosphere. It is noted here that Hathaway et al. (2010) and Hathaway (2012a) have used cross-correlation analysis, with various time lags, to track the meridional motion of supergranules as probes of subsurface meridional circulation, based on the assertions that the larger supergranules are longer-lived, and that the supergranulation phenomenon is as deep as it is wide (Hathaway et al., 2010; Hathaway, 2012b). Whereas the former assertion is based on observations, the latter is controversial and is contrary to time-distance helioseismic findings which seem to indicate that supergranules are shallow entities with depths of 10 Mm or less (Jackiewicz et al., 2008; Duvall and Hanasoge, 2013; Duvall et al., 2014).

1.1.1 Surface Observations

The early observations of meridional flow involved two main (non-helioseismic) techniques for determining the surface velocities on the Sun: the tracer or feature-tracking method and the spectroscopic method. The first method is based on the assumption

that the long-lived magnetic structures observed at the solar surface, such as sunspots (e.g., Howard and Gilman, 1986) and polar filaments (e.g., Topka et al., 1982), play roughly the same role as tracers in fluid dynamics experiments. The second method is based on the Doppler effect measured on spectral lines observed at different locations on the solar disk (e.g., Beckers, 1978; Duvall, 1979; Howard, 1979). These early measurements varied dramatically: many suggested a poleward flow of 10–20 m/s, but in other measurements amplitudes ranged 1–100 m/s, with complex latitudinal structure comprising poleward and equatorward flows, multiple cells, and large asymmetries about the equator.

The amplitude of meridional flow at the solar surface is known from observations to be of the order of 10 m/s as compared with the rotation velocity of 2 km/s, making it relatively difficult to measure the weaker meridional flow signal. Doppler measurements of the photospheric meridional circulation by, e.g., Hathaway (1996) yielded a typical poleward flow of about 20 m/s. This mean poleward flow was found to be nearly symmetric about the equator, peaking at latitudes of about 40°. Contemporaneous estimates of the meridional circulation obtained from cross-correlation of magnetic features gave an average latitudinal flow which is poleward at low latitudes and weakly equatorward at high latitudes, with a peak amplitude of about 15 m/s (e.g., Komm et al., 1993; Snodgrass and Dailey, 1996).

More recently, Švanda et al. (2007) applied a local correlation tracking technique, which uses large-scale supergranulation patterns from averaged Doppler images as tracers for the velocity vector determination, to measure surface meridional flows. Hathaway and Rightmire (2010) measured meridional flow by following the motions of the small magnetic elements that populate the entire surface of the Sun. Hathaway et al. (2010) used the notion that supergranules are advected by meridional flow to measure the latter by performing cross-correlation analysis on Doppler features. Doppler shifts of the full solar disk obtained over the period 1986–2009 were analyzed by Ulrich (2010) to determine meridional flow velocity at the solar surface; an equatorward flow was detected in the polar regions for three successive solar minima (1986, 1996, 2008). An earlier measurement by Schou (2003) using supergranular waves (Gizon et al., 2003) as tracers in Doppler velocity data, spanning May 24–July 22, 1996 in similar latitude ranges, did not find any evidence of a reversed cell in latitude. The later measurement techniques estimated the peak surface meridional flow to be around 10–15 m/s (cf. Figure 1.1; includes time-distance helioseismic measurement of

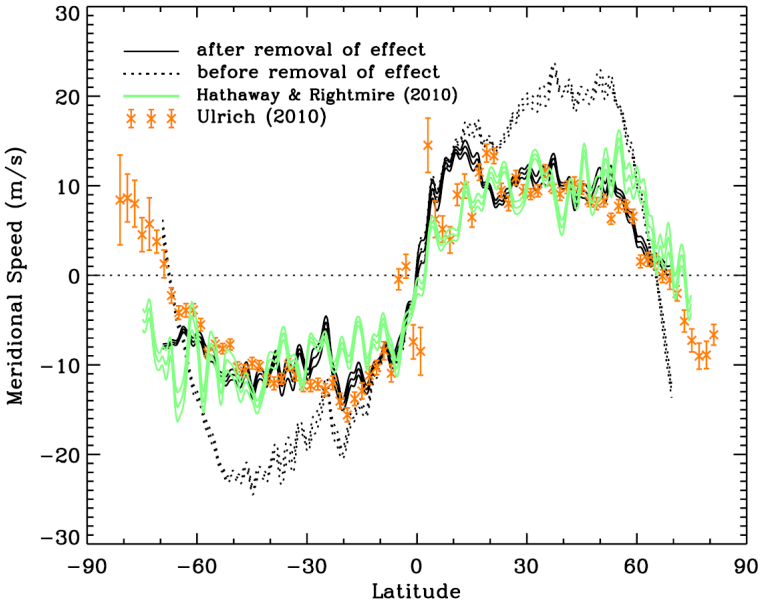

Figure 1.1: Surface meridional flow speed obtained by magnetic feature tracking (green; Hathaway and Rightmire, 2010) and from Doppler shift measurements (orange; Ulrich, 2010), and time-distance helioseismic inference (Zhao et al., 2012) for a depth of 0–1 Mm before (black dashed) and after (black solid) the removal of the systematic "center-to-limb" effect. Courtesy: Zhao et al. (2012).

surface meridional flow from Zhao et al., 2012). Roudier et al. (2012) used correlation tracking of granulation to measure meridional flow velocity; the preliminary results are consistent with the other measurement techniques.

1.1.2 Global Helioseismic Inferences

Global helioseismology is the study of the structure and dynamics of the solar interior from distortions in the normal solar oscillation modes relative to a reference solar model. Steady meridional flow does not make first-order perturbations to the frequencies of helioseismic normal modes. It does, however, Doppler shift the local wavenumber, thereby distorting the eigenfunctions (e.g., Gough and Hindman, 2010). Schad et al. (2013) applied a new global helioseismic technique based on the perturbation of eigenfunctions of low- and medium-degree solar p modes due to meridional flow (cf. Woodard, 2000; Woodard et al., 2013; Schad et al., 2011, 2012) on Michelson Doppler Imager (MDI) data (aboard the Solar and Heliospheric Observatory or SOHO spacecraft) resulting in a complex meridional flow structure with multiple cells in the

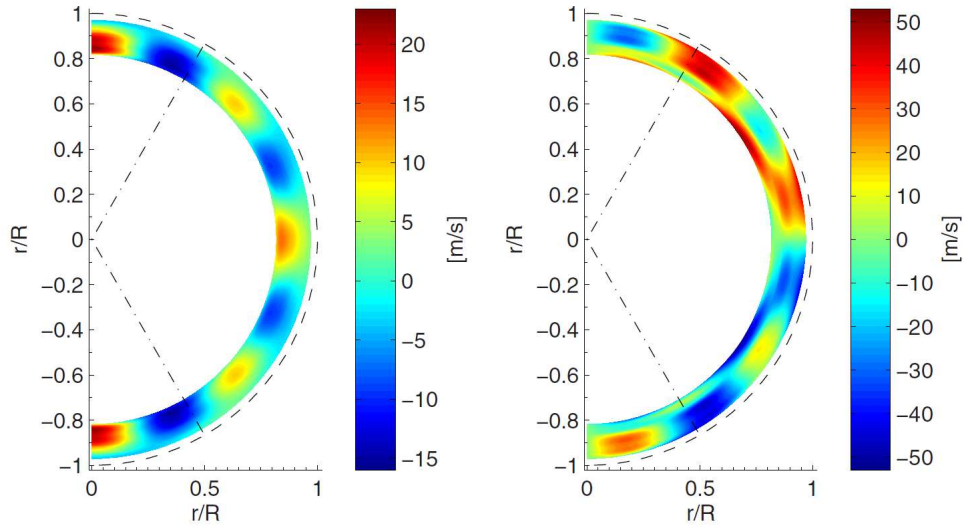

Figure 1.2: Meridional flow between $0.82R_\odot$ and $0.97R_\odot$. The solar surface is marked by a dashed semicircle. Dashed-dotted radial lines mark the $\pm 60°$ latitudes. Left: Radial flow velocity with positive (negative) values corresponding to outward (inward) directed flows. Right: Latitudinal flow velocity with positive (negative) values corresponding to northward (southward) directed flows. Courtesy: Schad et al. (2013).

radial as well as the latitudinal direction (Figure 1.2). Schad et al. (2013) wrote:

> Near the Solar surface, our flow measurements are consistent with measurements from ring-diagram analysis of GONG[1] data covering 2001–2009 (Komm et al., 2005; González Hernández et al., 2010), which show a residual small-scale modulation of the meridional flow in the Solar subsurface. This modulation is discussed as a meridional component of the torsional oscillation of the zonal flow that is present throughout the convection zone (Vorontsov et al., 2002; Howe et al., 2005). However, local helioseismic measurements were not able to probe this small-scale meridional flow component beyond the subsurface layer...Our results reveal that this subsurface modulation represents only the head of a layer of flow cells which extends throughout the whole convection zone. Therefore, we suspect a global coupling mechanism between the zonal and the meridional flow residuals.

[1]The Global Oscillation Network Group or GONG is a six-station network of velocity imagers located around the Earth to obtain nearly continuous observations of solar oscillations for helioseismic studies.

1.1.3 Local Helioseismic Inferences

Local helioseismology is the study of the solar surface and interior using the perturbations to the local acoustic wavefield due to local inhomogeneities or flows. The first helioseismic inferences of meridional flow were carried out with local helioseismic techniques using (high-degree) acoustic modes that are not sensitive to the deep interior. Giles et al. (1997) were the first to attempt this with time-distance helioseismology, followed by González Hernández et al. (1998), and Schou and Bogart (1998) using ring-diagram analysis.

Near-Surface Flows

Near the surface the local helioseismic results are generally consistent with Doppler and tracer measurements, showing poleward flow of about 20 m/s and significant asymmetry about the equator (e.g., Giles et al., 1997; Chou and Dai, 2001; Haber et al., 2002; Basu and Antia, 2003; Zhao and Kosovichev, 2004). Haber et al. (2002) have reported a flow reversal in the northern hemisphere where the circulation becomes equatorward at depths of about 3–15 Mm below the photosphere; the ring-diagram analysis spans six years (1996–2001), with the flow reversal (compare with surface measurements of Ulrich, 2010) occurring in the latter four (1998–2001). Such a flow reversal is not evident in the time-distance results of Zhao and Kosovichev (2004) who presented meridional flows averaged over depths of 3–4.5 Mm and 6–9 Mm. Komm et al. (2013) have determined the meridional flow from near-surface layers to about 16 Mm using ring-diagram analysis on data from the HMI instrument aboard the Solar Dynamics Observatory (SDO) spacecraft; the measured average meridional flow is poleward at most depths and latitudes with a maximum amplitude of about 20 m/s near 37.5° latitude.

Meridional Counterflows[2]

Since mass does not pile up at the polar regions of the Sun, it is believed that an equatorward counterflow in both hemispheres must exist somewhere in the interior to conserve mass flux. Giles et al. (1997) presented time-distance results for the upper 4% of the solar interior and concluded that the meridional flow throughout this region

[2]Figure 1.3 (left) is adapted by permission from Macmillan Publishers Ltd.: Nature, Giles et al. (1997), copyright 1997.

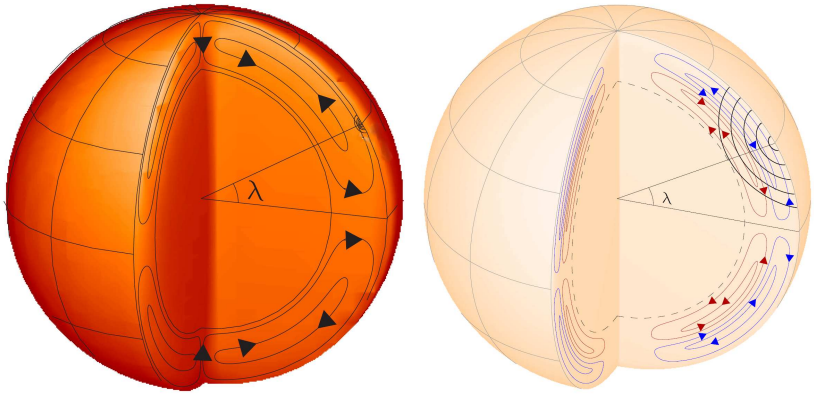

Figure 1.3: Left: Black streamlines show the schematic structure of single-cell meridional circulation inside the solar convection zone. Courtesy: Giles et al. (1997). Right: Blue (counter-clockwise cell) and red (clockwise cell) streamlines show the schematic structure of double-cell meridional circulation inside the convection zone. The common-midpoint deep-focus time-distance scheme is displayed with black curves showing some samples of acoustic wave paths. Courtesy: Zhao et al. (2013).

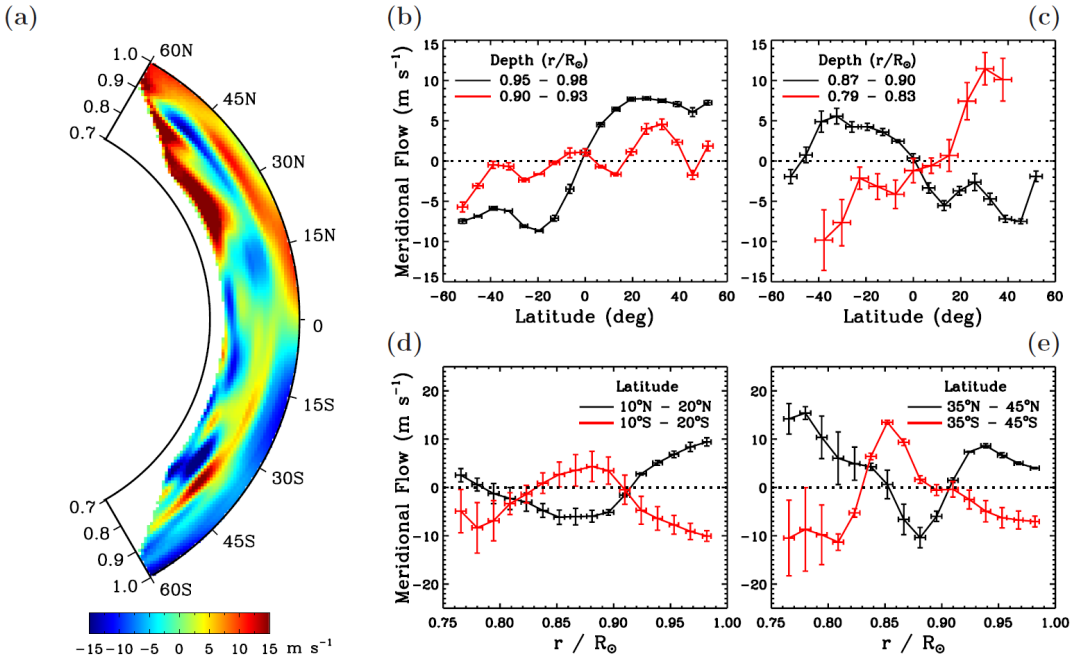

Figure 1.4: Meridional flow profile, obtained by inverting the measured acoustic travel times. (a) Meridional flow profile, with the positive velocity directed northward. (b)–(c) The inverted velocity as a function of latitude averaged over different depth ranges. (d)–(e) The velocity as a function of depth averaged over different latitude ranges. Courtesy: Zhao et al. (2013).

was poleward. By imposing a mass-conservation constraint, inversions of the time-distance measurements on MDI data suggested a single-cell meridional circulation (cf. left diagram in Figure 1.3) in the convection zone that is equatorward below about $0.8R_\odot$, with a speed of about 2 m/s at the base of the convection zone (Giles, 2000).

After correcting for a systematic "center-to-limb" effect (Zhao et al., 2012), Zhao et al. (2013) calculated from HMI data (cf. right diagram in Figure 1.3 and Figure 1.4) that the poleward meridional flow observed on the surface extends to a depth of approximately 65 Mm ($\approx 0.91R_\odot$). The flow direction, displaying substantial hemispheric asymmetry, then turns equatorward with a maximum speed of about 10 m/s, until about $0.82R_\odot$ where the flow becomes poleward again. The inversion stops at about $0.75R_\odot$ and $\pm 60^\circ$ latitudes, which allows for the possibility of more circulation cells in the radial as well as the latitudinal directions. Kholikov et al. (2014) also found evidence of multi-cell meridional circulation by applying the time-distance technique on GONG data.

In the context of helioseismic holography, Braun and Birch (2008) asserted that one of the fundamental difficulties in measuring meridional flow at the base of the convection zone is due to the poor signal-to-noise ratio of the measurements there for a flow of about 3 m/s. For comparison, the sound speed at the base of the convection zone is roughly 230 km/s. Braun and Birch (2008) concluded that the helioseismic detection of meridional flow near the base of the convection zone may not be possible using travel-time measurements spanning an interval less than a solar cycle. However, it may be possible for a flow of 10 m/s (e.g., Gough and Hindman, 2010; Pipin and Kosovichev, 2011).

1.2 Meridional Circulation: Simulations

It is not the purpose of this section to exhaustively review or critique the theoretical or simulation work done on large-scale flows in the solar interior—rather, the purpose is to illustrate some select results which, though oversimplistic, may still be used as a guide for helioseismic inferences. In the absence of accurate observations, theory is the only means at the solar physicist's disposal to determine the properties of the solar interior; theory may also provide observational strategies. In fact, as will be seen in Chapter 3, some of the models and simulations encountered in this section can be used for *forward modeling* in time-distance helioseismic analysis. Whether future

observations and inferences will corroborate or refute these theoretical constructs still remains to be seen. Future inferences will guide theoretical advances by providing ever greater observational constraints on the structure of meridional circulation. The dialectical engagement between theory and observation is the basis for the evolution of scientific knowledge.

Relevant figures are reproduced from the indicated references, and pertinent information is provided in this section and the figure captions. To obtain more details and to ascertain whether the assumptions and parametrizations involved are valid for the solar interior, the reader is referred to the indicated sources and the references therein.

1.2.1 Mean-Field Hydrodynamical Models

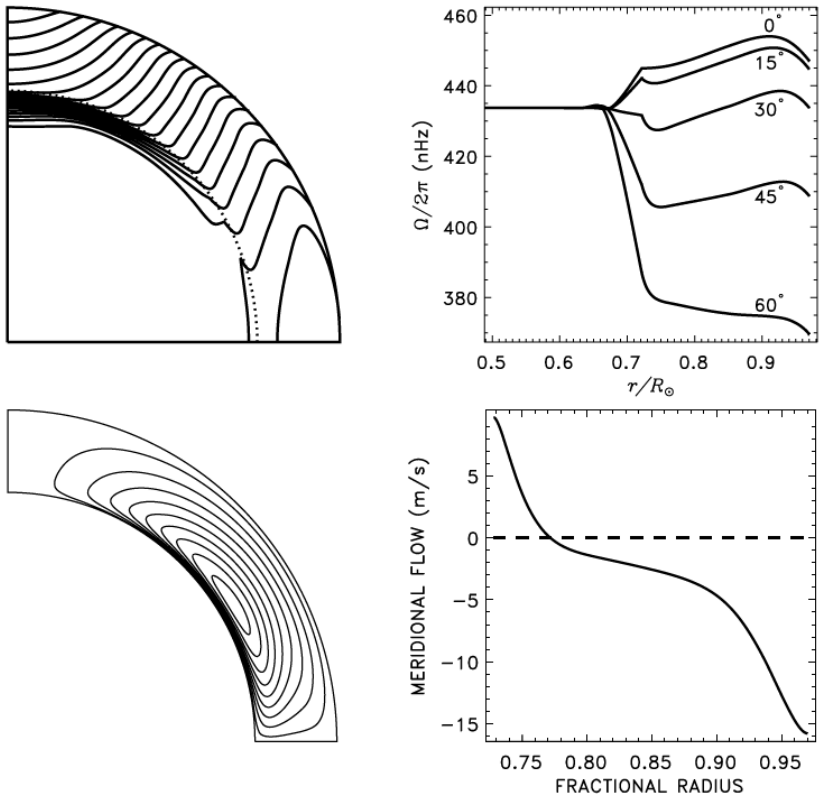

Figure 1.5: This mean-field hydrodynamical model jointly computes the differential rotation, meridional flow and heat transport in the solar convection zone. Upper panels show the angular velocity isolines (left) and the differential rotation depth profiles for several latitudes (right). Lower panels show the streamlines of meridional flow (left) and the radial profile of meridional flow velocity at 45° latitude (right). Negative velocity indicates poleward flow. Courtesy: Kitchatinov and Olemskoy (2011).

Mean-field hydrodynamical models are essentially derived from the equations of momentum and energy conservation (Rüdiger, 1989; Küker and Stix, 2001; Stix, 2004). Figure 1.5 shows a mean-field hydrodynamic model (Kitchatinov and Olemskoy, 2011) with solar-like differential rotation and single-cell meridional circulation resulting from the anisotropy of transport of angular momentum and energy due to the influence of rotation on convective turbulence. Thus far this has been the favored meridional flow model for a flux-transport dynamo. But 21st century helioseismology is putting a strain on the status quo.

Figure 1.6 shows a latitudinally stacked double-cell meridional circulation structure. Dikpati (2014) finds that the steady-state solution of the hydrodynamic model, which includes Coriolis forces and turbulent Reynolds stresses, is sensitive to the magnitude of the density decline with radius, yielding a single flow cell with poleward surface flow for density declines of less than about a factor of 4 within the convection zone, but two cells, with a reversed circulation in high latitudes, for all higher density declines, including that for the adiabatically stratified solar convection zone. Although the Dikpati (2014) model leaves out much physics, the two-cell meridional

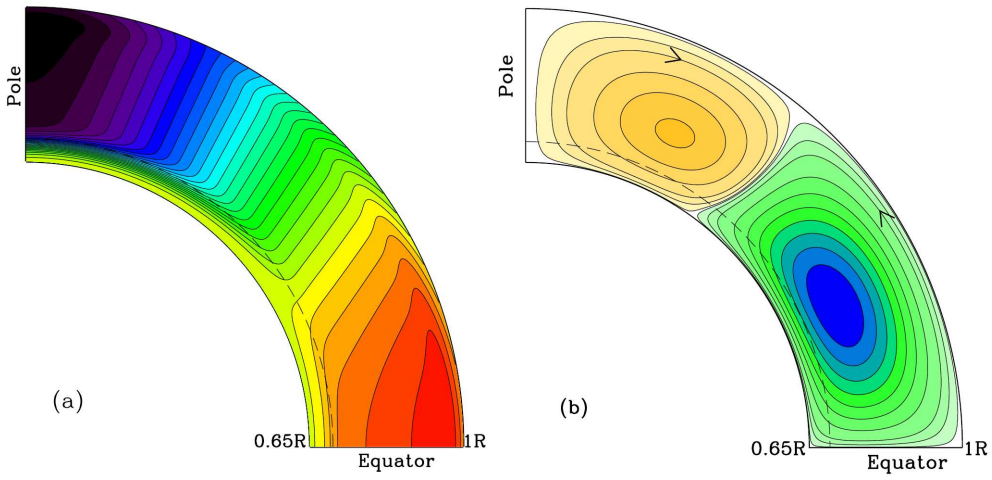

Figure 1.6: (a) Parametrized differential rotation contours obtained using a mathematical formula following Dikpati et al. (2002). Based on helioseismic observations, this is the most realistic case for the Sun. (b) Stream function for meridional flow driven by Coriolis forces associated with differential rotation profile shown in panel (a). This simulation has resulted in a latitudinal double-cell circulation, with a dominant primary cell in low and mid-latitudes, and a weaker counter cell at high latitudes, with the inter-cell boundary near 55°. Courtesy: Dikpati (2014).

circulation depicted in Figure 1.6 is consistent with the findings of an equatorward cell at high latitudes by Haber et al. (2002) and Ulrich (2010). The global helioseismic results of Schad et al. (2013) also seem to imply that such latitudinally arranged cells are possible.

The case in Figure 1.7[3] is the result of the work done before the simultaneous inclusion of anisotropy of angular momentum and heat transport in mean-field hydrodynamics became the vogue, and also before the helioseismically determined interior rotational dynamics of the Sun became the established paradigm. This result is interesting because the recent time-distance inferences of Zhao et al. (2013) seem to be endorsing the double-cell meridional circulation pattern that have emerged in the computations of Stix (1987). In this hydrodynamic model, the radially stacked double-cell circulation has properties that qualitatively match solar observations. However, the poleward flow at the base of the convection zone cannot result in solar-like dynamo behavior in the flux-transport paradigm (e.g. Jouve and Brun, 2007; Hazra et al., 2014).

[3]Figure 1.7 is reprinted with kind permission from Springer Science and Business Media: Stix (1987), D. Reidel Publishing Co.

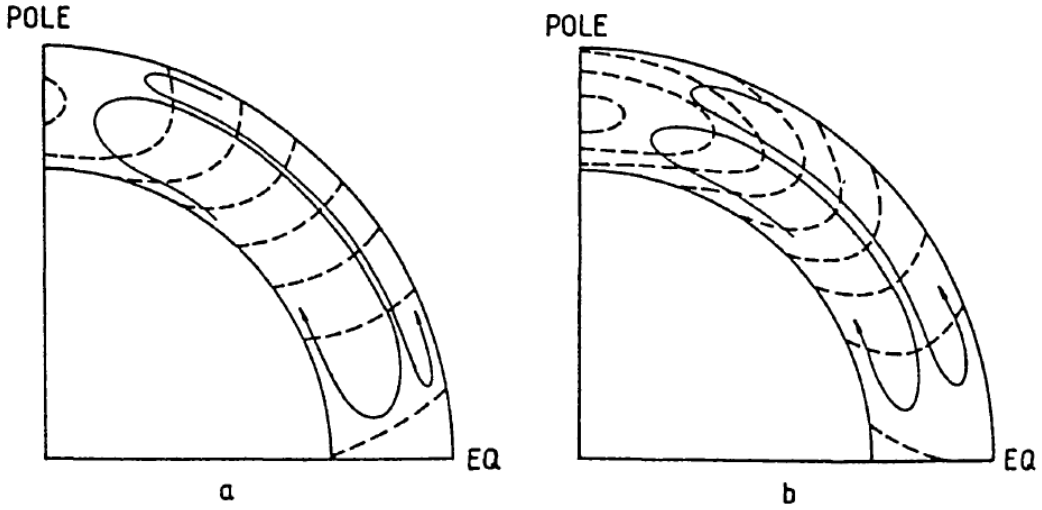

Figure 1.7: Surfaces of constant angular velocity (dashed), and streamlines of meridional circulation for (a) a model with anisotropic viscosity with pole-equator temperature difference of 1 K and flow speed of 1 m/s, and (b) a model with latitude-dependent heat transport resulting in a pole-equator temperature difference of 0.5–6 K and flow speeds of 15–36 m/s. The anisotropic viscosity and the latitude-dependent heat transport arise from the influence of rotation upon convection, generating meridional circulation and therewith differential rotation. Courtesy: Stix (1987).

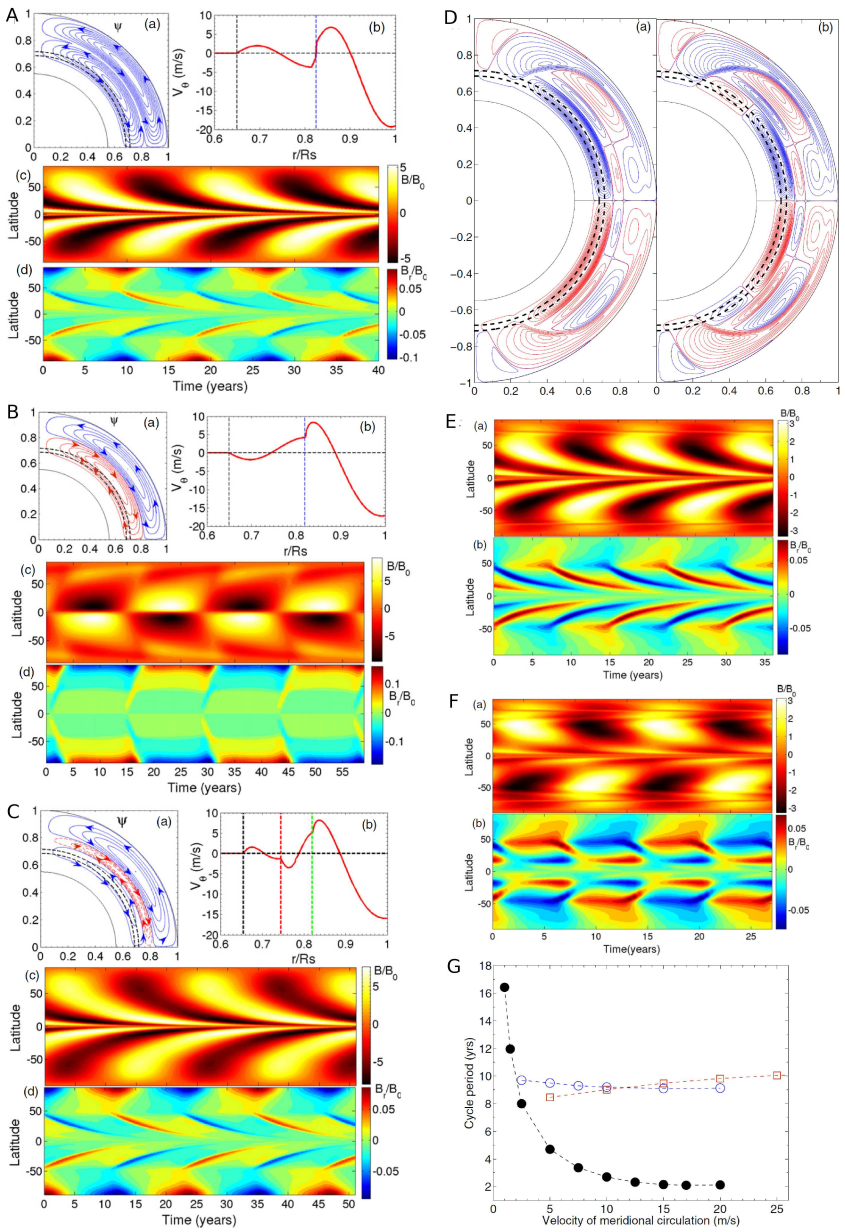

Figure 1.8: Panel A: (a) Streamlines for two radially stacked counter-clockwise cells of meridional circulation. (b) v_θ as a function of $r/R_\odot$ at 45° latitude. (c) Time-latitude plot of toroidal field at base of convection zone ($r = 0.70R_\odot$). (d) Time-latitude plot of surface radial field. Panel B: (a) Double-cell meridional circulation. Panel C: (a) Triple-cell meridional circulation. (b)–(d) in panels B and C same as in Panel A for appropriate meridional circulation. Panel D: Two complicated meridional flow models. Panel E: (a) and (b) are same as (c) and (d) in Panels A–C for model in Panel D(a). Panel F: Same as Panel E, for model in Panel D(b). Panel G: Black filled circles show variation of cycle period with flow speed of lower cell, while keeping velocities of other cells in Panel C(a) constant; blue circles show period-speed relationship of middle cell; red boxes for upper cell. Courtesy: Hazra et al. (2014).

1.2.2 Flux-Transport Dynamo Models

Flux-transport dynamo models were first outlined in Choudhuri et al. (1995). Dikpati and Gilman (2009) characterized them as follows:

> Flux-transport dynamos are just the so-called α-Ω dynamos[4] with meridional circulation. Flux-transport dynamos include three basic processes: (i) shearing of the poloidal magnetic fields to produce toroidal fields by the Sun's differential rotation (the Ω-effect), (ii) regeneration of poloidal fields by displacing and twisting the toroidal flux tubes by helical motions (the so-called α-effect), and (iii) advective transport of magnetic flux by meridional circulation, whereas an α-Ω dynamo involves only the first two. Meridional circulation acts as a conveyor belt in this class of models.

Figure 1.8 shows the flux-transport dynamo cycles for multi-cell meridional circulation. The results in Hazra et al. (2014) indicate that as long as there is a sufficiently extended equatorward flow connecting the high-latitude region to the mid- to low-latitude region at the base of the convection zone, solar-like butterfly diagrams (cf. `http://solarscience.msfc.nasa.gov/SunspotCycle.shtml`) can be obtained with a flux-transport dynamo.

1.2.3 Three-dimensional Global Numerical Simulations

In the mean-field approach the focus is on the large scales; the effects of small-scale, unresolved turbulence is parametrized. Nonlinear terms in the momentum, energy and induction equations lead to non-vanishing second order correlation terms of small-scale quantities that act as drivers for large-scale (mean) flows or as turbulent induction effects for the large-scale magnetic field. The decomposition into large- and small-scale (fluctuating) properties and the resulting correlation terms driving large-scale flows are the strength and the weakness of this approach at the same time. Also, in most mean-field flux-transport models the flow velocity is prescribed, rather than solved explicitly. The parametrization and the ad hoc flow velocity decrease the computational expense by orders of magnitude allowing for simulations covering long time scales, and for exploring wide parameter ranges. However, the results are heavily dependent on parametrization of the second order correlation terms that may be ill-suited, along with the prescribed flow velocities, for solar interiors. For a scathing criticism of the mean-field approach see Spruit (2011).

[4] α-Ω dynamos are discussed in, e.g., Parker (1955), Steenbeck et al. (1966), and Rädler (2007).

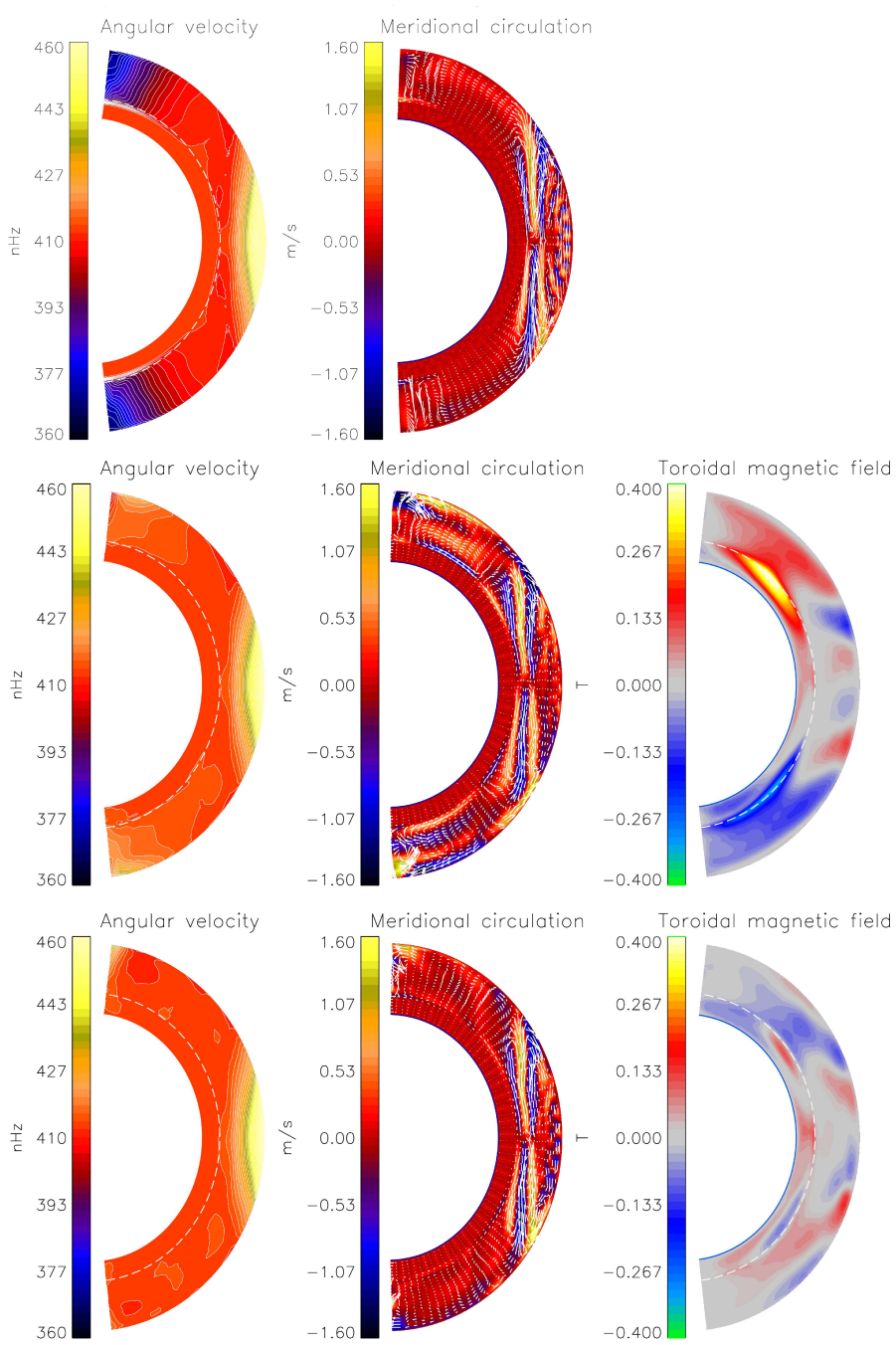

Figure 1.9: Top row shows a hydrodynamical simulation whereas the middle and bottom rows show a MHD simulation of the solar convection zone. The rows show zonally averaged angular velocity (left), and meridional flow (middle). The middle and bottom rows also show a toroidal magnetic component (right) at cycle maximum (t=16 years, middle row) and minimum (t=32 years, bottom row). The meridional flow vectors (white arrows) are superimposed on the latitudinal mean-flow v_θ. The differential rotation is steady over the duration of the simulation, whereas the meridional flow fluctuates. Courtesy: Racine et al. (2011).

According to Charbonneau (2010), "[u]ltimately, the solar dynamo problem should be tackled as a (numerical) solution of the complete set of [magnetohydrodynamic (MHD)] partial differential equations[, with the appropriate boundary conditions] in a rotating, stratified spherical domain undergoing thermally-driven turbulent convection in its outer 30% in radius." However, none of the current numerical models are able to reproduce sufficiently well the solar differential rotation and meridional circulation. In particular, the models are not able to reproduce the tachocline (the transition region between the differentially rotating convection zone and the quasi-rigidly rotating radiative interior; cf. Spiegel and Zahn, 1992) and the near-surface shear layer (NSSL: a thin region of increasing angular velocity with depth just beneath the solar surface; cf. Corbard and Thompson, 2002), and are still not able to adequately reproduce the solar activity cycles. Despite the fast developments of computer capabilities, all global simulations are far from realistically modeling the Sun. In particular, modeling solar convection is a formidable challenge. Abrupt changes in the stratification give rise to relatively small-scale granulation near the surface and convective penetration into the stably-stratified radiative interior underlying the convection zone. The range of dynamical scales present is tremendous: from the depth of the convection zone, 2×10^{10} cm, to the viscous dissipation scale which is estimated to be of order 1 cm (e.g., Miesch, 2005).

The MHD situation is more complicated than that of pure hydrodynamics. A dynamically significant magnetic field which varies cyclically, introduces nonlinear time dependent effects into the system via the Lorentz force capable of influencing the conducting fluid flow (cf. Charbonneau, 2010). As can be seen in Figure 1.9, compared to the hydrodynamic case the latitudinal differential rotation is suppressed in the MHD case, and the meridional circulation is enhanced during the magnetic cycle maximum (cycle period roughly 30 years). In both the hydrodynamical and MHD case, the angular velocity profile is solar-like and the meridional flow structure is multi-celled and messy.

1.3 Dissertation Outline

This dissertation further refines the interpretation of travel-time shifts in the context of time-distance helioseismic measurement of meridional flow. In fact, travel-time shifts are measured, and meridional flow velocities are inferred from the travel-time

shifts by *inversion*.

Chapter 1 briefly overviews the observed, or rather, inferred structure of meridional circulation, and the expected structure from a theoretical standpoint. Chapter 2 covers aspects of solar oscillations and time-distance helioseismology relevant for the material covered in this dissertation. Chapters 3 and 4 contain original research done by the author and thus constitute the main substance of this dissertation.

Chapter 3 explores forward modeling in the ray approximation with simulations. For accurate inversion of travel-time shifts to obtain flow velocities, the travel-time shifts have to be accurately interpreted or forward modeled. The forward modeling is done in the ray-theoretic approximation, whereby the travel times are interpreted as the travel times of waves propagating according to the rules of ray geometry, and non-vanishing travel-time shifts of counter-propagating waves are perturbations due to Doppler shifts induced by meridional flow. This interpretation is tested against time-distance analysis of two independent three-dimensional acoustic wave simulation data (Hanasoge et al., 2006; Hartlep et al., 2013) perturbed by single- and double-cell meridional flow models. A systematic effort is made for the first time in the context of meridional flow (for supergranulation cf. Duvall and Hanasoge, 2013; Duvall et al., 2014) to incorporate some of the physics of the simulations into the ray-theoretic computations. The full deep-focus scheme is used for the first time to measure meridional flow induced travel-time shifts on phase-speed filtered simulation data. Notwithstanding, in this work ray theory could not be established as an adequate model for interpreting meridional flow induced travel-time shifts. Since the *sensitivity kernel* (cf. Gizon and Birch, 2005) needed for accurate inversions is derived from a robust forward model, this work casts doubts (not for the first time; e.g., Bogdan, 1997; Birch and Gizon, 2007) on the reliability of the traditional ray-theoretic kernels.

Chapter 4 builds on the techniques developed for use in Chapter 3, and applies them to HMI data. Travel-time shifts are measured for the first time on spherical harmonic reconstructed and phase-speed filtered HMI data using the full deep-focus technique. The main target here is the "center-to-limb" effect that contaminates the measurement of travel-time shifts due to meridional flow. Baldner and Schou (2012) provided a plausible physical basis for this effect, but it is not yet a firmly established theory. A new method is devised, using non-standard time-distance geometry and a model center-to-limb phase-shift function, to characterize the "center-to-limb" effect, to test if it is a true heliocentric angle dependent phase function. The test is

theoretically sound, but is unsuccessful due to the noise level in the travel-time shift measurements.

Chapter 5 summarizes the dissertation, and concludes with a few remarks on future directions and strategies.

Appendix A derives the correct expression for the travel-time shift due to radial flow since Equation (2.43) in Giles (2000) for the aforementioned quantity is incorrect. According to Giles (2000) if the radial flow is uniform everywhere, then the travel-time shift due to the radial velocity should be zero, as counter-propagating rays will experience the same net flow; Equation (2.43) in Giles (2000) does not reflect that fact. This derivation is connected to the work done in, for example, Duvall and Hanasoge (2013) and Duvall et al. (2014) to compute the travel-time shifts due to vertical flows in supergranules.

Chapter 2

Time-Distance Helioseismology

The deep interior of the Sun was one of the least accessible regions to scientific investigation until about 50 years ago. Early attempts to probe the solar interior were mainly confined to spectroscopic studies of the surface layers. With the advent of observations of solar oscillations it became possible to infer the internal structure of the Sun by using the measured eigenfrequencies of solar oscillation modes—this method was among the early techniques of helioseismology. These helioseismic techniques examined the longitude independent global properties of the Sun that were symmetrical about the equatorial plane. The *global* helioseismic techniques had limited ability to study the properties of local regions, or spherically asymmetric effects other than rotation, and had limited sensitivity to complex flows. These limitations were overcome with *local* helioseismic techniques that rely on the interaction of traveling acoustic waves with small perturbations to the background state.

Time-distance helioseismology (aka helioseismic tomography or telechronohelioseismology), a powerful local helioseismic technique, was introduced by Duvall et al. (1993). The basic idea is to measure the time it takes for a wave to travel from one point on the solar surface to another. Since the excitation of solar acoustic waves is stochastic, and it is not possible to isolate individual sources, Duvall et al. (1993) suggested that wave travel times can be measured by computing the temporal cross-covariance of the signal at a point on the solar surface with the signal at another point. The rationale behind this idea is that in a local, horizontally invariant region, the cross-covariance function is the Fourier transform of the solar oscillation power spectrum. This implies that changes in the local power spectrum due to inhomogeneities or flows affects the cross-covariance function.

With time-distance measurements it is possible to infer subsurface properties at a high spatial resolution (a few megameters can be achieved near the surface; the limit is set by the smallest available horizontal wavelength of high-frequency f modes). Detailed three-dimensional maps of vector flows in the upper convection zone have provided new insights into the structure, evolution, and organization of magnetic active regions (e.g., Kosovichev et al., 2000; Zhao et al., 2010) and convective flows (e.g., Jackiewicz et al., 2008; Duvall and Hanasoge, 2013; Duvall et al., 2014). The time-distance method has been used to measure large-scale zonal and meridional flows in the solar convection zone (e.g., Giles, 2000; Zhao et al., 2013), and to detect active regions on the farside of the Sun (Zhao, 2007). This technique has also proven capable of detecting signatures of emerging sunspot regions in the solar interior before their appearance at the surface (Ilonidis et al., 2011, 2013).

Since the time-distance technique is used in this dissertation, this chapter reviews some basic material: Section 2.1 discusses properties of solar acoustic oscillations, and Section 2.2 details the relevant aspects of travel-time computation.

2.1 Solar Oscillations

Solar oscillations (cf. Figure 2.1) with a period of about 5 minutes were first observed in 1960 (Leighton, 1960; Leighton et al., 1962) by a spectroheliographic technique at Mount Wilson Observatory (MWO). Ulrich (1970) and Leibacher and Stein (1971) explained the observed oscillatory motions by invoking standing acoustic waves in the solar interior. Several other studies (Deubner, 1975; Rhodes et al., 1977; Claverie et al., 1979; Duvall and Harvey, 1983) confirmed this interpretation and found a ridge structure in the power spectra which was consistent with the standing waves interpretation. Solar oscillations are believed to arise due to excitation by turbulent convective motions near the surface of the Sun (Goldreich and Keeley, 1977), mainly in the vicinity of the intergranular lanes (Stein and Norlund, 2001).

The solar surface is in continual motion due to the interference of millions of wave modes, and due to convective turbulence. The amplitude of a single mode is about 30 cm/s, and the interference of 10 million or more oscillation modes with randomly distributed phases results in oscillation amplitudes of 0.5–1 km/s or larger in extreme cases. In the Sun, detected waves that possess diagnostic value are either surface gravity or acoustic modes. While surface gravity modes are restricted to the surface

Figure 2.1: MDI single Dopplergram, with a mean solar velocity image averaged over 45 minutes subtracted. The surface motions associated with sound waves traveling through the Sun's interior are discernible. The small-scale light and dark regions represent the upward and downward motions, respectively, of the plasma near the solar surface. The patterns fade towards the limb because of the primarily radial displacement of the acoustic waves. Courtesy: SOI/MDI Team.

layers, acoustic modes penetrate the depths of the solar interior and resurface altered by the structure and dynamics of the traversed interior. Because the Sun is stratified such that the sound speed monotonically increases with depth, acoustic waves near the photosphere that are directed towards the interior, propagate some distance while refracting away from the center. Eventually they undergo total internal reflection and return to the surface. Because of the sharp density decline in the near-surface regions, acoustic wave modes below a certain characteristic "cut-off" frequency are reflected back toward the solar interior where they remain trapped in a resonant cavity until they are damped out by convective, radiative and other processes. The typical timescale of large wavelength modes is about 5-7 days while the smaller wavelengths are damped out much more quickly and replaced by other waves continually generated by the overturning convective cells (known as granules) at the solar surface.

2.1.1 Normal Modes of Oscillation

The solar oscillations are reasonably well approximated by the equations of linear adiabatic oscillations of a spherically symmetric (ignoring the effects of rotation and magnetic fields) star (e.g., Aerts et al., 2010). Assuming a spherically symmetric and time-independent equilibrium enables the solution to the equations of adiabatic stellar oscillations to be separable in the radial and angular coordinates, and in time. Along with the boundary conditions, they define an eigenvalue problem which has solutions only at discrete values of frequency or *eigenfrequencies*. The observed oscillation signal $f(r, \theta, \phi, t)$ being, roughly, the radial component of the solution, can be represented as a sum of normal modes (e.g., Kosovichev and Duvall, 1997):

$$f(r, \theta, \phi, t) = \sum_{n,l} \sum_{m=-l}^{m=l} A_{nlm} \xi_{nl}(r) Y_{lm}(\theta, \phi) \exp[i(\omega_{nlm} t + \alpha_{nlm})], \tag{2.1}$$

where the three integers n, l, m are the radial order, angular degree, and azimuthal order respectively, A_{nlm} is the mode amplitude, ξ_{nl} is the radial eigenfunction, Y_{lm} is the spherical harmonic, ω_{nlm} is the eigenfrequency, and α_{nlm} is the phase of the mode. The spherical harmonics have the form

$$Y_l^m(\theta, \phi) = a_{lm} P_l^m(\cos\theta) \exp(im\phi), \tag{2.2}$$

where P_l^m is the associated Legendre polynomial, and a_{lm} is a normalization factor. The radial order n corresponds to the number of nodes of the radial eigenfunction, the angular degree l gives the total number of node circles on the sphere, and the azimuthal order m indicates how many of these node circles cross the equator. In a spherical system with no preferred axis of symmetry, the eigenfrequencies do not depend on m. Since solar rotation defines a particular axis of symmetry, the oscillation frequencies show a weak dependence on m.

It follows from the above that the surface manifestation of solar oscillations can be decomposed into a sum of spherical harmonics for each instant of observation—this is also the basis for spherical harmonic reconstruction (Section 4.5). The resulting eigenfrequencies ω_{nlm} of the solar oscillations are measured from the resonant peaks in the power spectrum (cf. Figure 2.2), and used as a diagnostic of the solar interior. In Figure 2.2 the acoustic power is concentrated in ridges in wavenumber-frequency or k-ω space, with maximal amplitude around 3 mHz. The first ridge (radial order

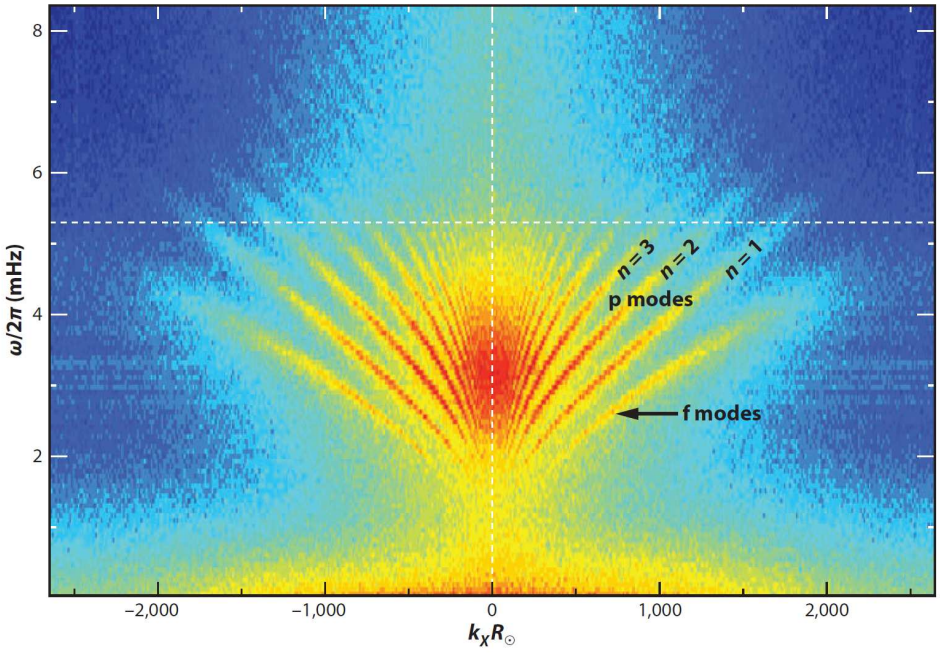

Figure 2.2: Cut at $k_y = 0$ through an average power spectrum of MDI Doppler velocity data as a function of frequency and $k_x R_\odot$. The horizontal dashed line indicates the acoustic cut-off frequency. The power below 1.5 mHz is due to convective phenomena such as granulation and supergranulation. Courtesy: Gizon et al. (2010).

$n = 0$) at low frequencies is due to the *fundamental* or f modes or surface gravity waves. All other ridges correspond to *pressure* or p modes or acoustic waves. The existence of discrete ridges with $n > 0$ reflects the fact that p modes are trapped in the radial direction. The power above 5.3 mHz is attenuated; this marks the acoustic cut-off frequency above which the acoustic waves escape into the solar atmosphere. The frequency-width of a ridge is inversely proportional to the mode lifetime.

2.1.2 Properties of Acoustic Modes[1]

As discussed above, the acoustic modes are uniquely identified by the spherical harmonic degree l, azimuthal order m, and radial order n. For a non-rotating star the modes are degenerate in m. An asymptotic description of the equations of adiabatic stellar oscillations can be obtained by approximating the modes locally by plane sound waves satisfying the dispersion relation:

$$\omega^2 = c^2|\mathbf{k}|^2, \tag{2.3}$$

where ω is the frequency, c the sound speed, and $\mathbf{k}$ is the vector wavenumber. When the ideal gas law is satisfied, the sound speed is given by

$$c^2 = \frac{\Gamma_1 k_\mathrm{B} T}{\mu m_\mathrm{u}}, \tag{2.4}$$

where Γ_1 is the first adiabatic exponent, k_B is Boltzmann's constant, m_u is the atomic mass unit, and μ is the mean molecular weight which is determined solely by the composition.

Lower Turning Point

According to Equation (2.4) the sound speed is essentially determined by T/μ. Because of the increase in sound speed with depth (due to temperature rising with depth), waves that are propagating toward the interior refract continually until they undergo total internal reflection at some depth and eventually return to the surface. At the point of total internal reflection, also known as the lower turning point (and in the context of common-midpoint time-distance technique, the focal-depth; cf. Section

[1] All the equations and derivations in this section are essentially reproduced from Aerts et al. (2010).

2.2.3), the wave is propagating essentially horizontally, i.e., its radial component is zero. To determine the location of the lower turning point $\mathbf{k}$ is decomposed into a radial ($k_r\hat{\mathbf{r}}$) and a horizontal ($\mathbf{k}_\mathrm{h}$) component:

$$\mathbf{k} = k_r\hat{\mathbf{r}} + \mathbf{k}_\mathrm{h}. \tag{2.5}$$

Equations (2.3) and (2.5) yield

$$k_r^2 + k_\mathrm{h}^2 = \frac{\omega^2}{c^2}, \tag{2.6}$$

where $k_\mathrm{h} = |\mathbf{k}_\mathrm{h}|$ is the horizontal wavenumber:

$$k_\mathrm{h}(r) = \frac{\sqrt{l(l+1)}}{r}, \tag{2.7}$$

which is obtained from the solution for the angular component of the equations of adiabatic stellar oscillations. At the lower turning point $r = r_\mathrm{t}$, $k_r = 0$ since the wave is propagating horizontally, and the sound speed is equal to the horizontal phase speed of the mode: $c(r_\mathrm{t}) = \omega/k_\mathrm{h}(r_\mathrm{t})$, or

$$\frac{c(r_\mathrm{t})}{r_\mathrm{t}} = \frac{\omega}{\sqrt{l(l+1)}}. \tag{2.8}$$

Equation (2.8) provides the means to calculate the penetration depth of each wave mode. It also allows the determination of the frequency and wavenumber (or spherical harmonic degree l) of waves that can reach a given depth.

Equation (2.8) implies that oscillation modes with large l are confined within relatively shallow cavities below the surface, while the lower l modes propagate deeper. For a given $l \neq 0$, the depth of penetration increases with frequency and also with radial order n. All modes with a similar horizontal phase speed (a straight line through the origin in Figure 2.2) have a similar lower turning point and probe essentially the same layers of the Sun (the rationale behind phase-speed filtering; cf. Section 2.2.1). As various modes are trapped in different regions of the solar interior, they sample the thermodynamic properties of the entrapping resonant cavity. Thus the oscillation frequencies of different modes reflect different parts of the Sun, and permit a detailed inversion for the interior properties as a function of position. Figure 2.3 shows a schematic diagram of propagating acoustic waves in the solar interior.

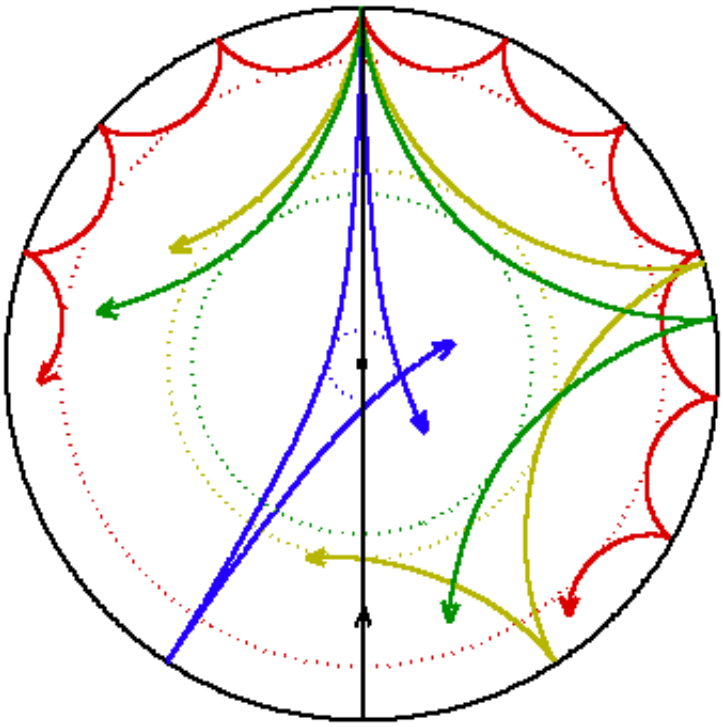

Figure 2.3: Propagation of the rays of sound in a cross-section of the solar interior. The acoustic paths are bent by the increase in sound speed with depth until they reach the lower turning point (indicated by the dotted circles) where they undergo total internal reflection. The acoustic waves are reflected at the surface by the sharp drop in density. The rays shown corresponding to modes of frequency 3000 μHz and degrees (in order of increasing penetration depth) $l = 75$ (red), 25 (olive green), 20 (dark green) and 2 (blue); the black line passing through the center schematically illustrates the behavior of a radial mode ($l = 0$). Courtesy: SOI/MDI Team.

Upper Turning Point

The acoustic cut-off frequency in the near-surface layers of the convection zone determines the upper reflective boundary of the solar acoustic waves. The expression for this quantity depends on the background solar model and the oscillation equations. In this work the more commonly used expressions for the acoustic cut-off frequency are reproduced (e.g., Deubner and Gough, 1984; Aerts et al., 2010).

The generalized acoustic cut-off frequency is given by

$$\omega_{\rm ac}^2 = \frac{c^2}{4H^2}\left(1 - 2\frac{{\rm d}H}{{\rm d}r}\right), \tag{2.9}$$

where H is the density scale height:

$$H^{-1} = -\frac{{\rm d}\ln\rho}{{\rm d}r}. \tag{2.10}$$

In the case of an isothermal atmosphere $H = H_p$ is constant, where H_p is the pressure scale height defined as

$$H_p^{-1} = -\frac{{\rm d}\ln p}{{\rm d}r}, \tag{2.11}$$

and the generalized cut-off frequency simplifies to the isothermal acoustic cut-off frequency:

$$\omega_{\rm ac} = \frac{c}{2H_p}. \tag{2.12}$$

Physically, this corresponds to the reflection of the waves into the solar interior where the acoustic wavelength becomes comparable to the local density or pressure scale height, as the case may be. Modes with frequencies exceeding the atmospheric value of the acoustic cut-off frequency are only partially trapped and mostly escape into the atmospheric layers.

2.2 Computing Travel Times

This section is not intended to be a comprehensive review or critique of time-distance techniques; rather, it is an overview of the techniques applied in this dissertation to compute travel times and travel-time shifts. The curious reader is referred to the excellent review papers that exist on the subject, e.g., Gizon and Birch (2005), Gizon et al. (2010), Kosovichev (2011), and the references therein.

2.2.1 Phase-Speed Filtering

The rationale for phase-speed filtering is that waves with similar horizontal phase speeds follow approximately the same trajectory in the solar interior. More importantly, for the purposes of this dissertation, the waves access similar depths; this permits the possibility of extracting information about meridional flows at those depths

from the observed travel times of the "iso-phase-speed" waves. Phase-speed filters enable the selection of wave packets with a specific phase speed containing relevant information, filtering out irrelevant information or "noise", thus increasing the signal-to-noise ratio of the temporal cross-covariance functions, and consequently, of the travel-time maps.

In the plane-parallel or Cartesian geometry, phase-speed filtering amounts to a multiplication in the Fourier or $\mathbf{k}$-ω domain (e.g., Couvidat and Birch, 2006):

$$\tilde{\phi}(\mathbf{k},\omega) = F(k,\omega;\Delta)\tilde{f}(\mathbf{k},\omega), \tag{2.13}$$

where $\mathbf{k}$ is the horizontal wave vector, $k = |\mathbf{k}|$, ω is the angular frequency, and $\tilde{f}$ is the Fourier transform of the signal in Equation (2.1), representing say, the line-of-sight Doppler velocity data. In spherical geometry, spherical harmonic transforms are involved.

The phase-speed filters F generally have the Gaussian form:

$$F(k,\omega;\Delta) = \exp\left\{-\frac{[\omega/k - v(\Delta)]^2}{2\delta v^2}\right\}, \tag{2.14}$$

where $v(\Delta)$ is the phase speed at the lower turning point of a wave with single-skip distance Δ, and δv is the full width at half maximum (FWHM) of the filter. The FWHM δv of the phase-speed filters used in this dissertation were chosen empirically. Various filter widths were experimented with, and it was found that for a reasonably wide range of filter widths the time-distance computations of the travel-time shifts due to meridional flow yielded similar results within error bars. This is to be expected from theoretical considerations: meridional flow signals are relatively unchanging in time and homogeneous in horizontal space compared to the acoustic modes, causing the signal to be relatively independent of filter width in frequency and horizontal wavenumber (or l). This is certainly not true for supergranulation (cf. Duvall and Hanasoge, 2013).

The author picked the following filter width scheme:

$$\delta v = 10 r_t, \tag{2.15}$$

where δv is in m/s, and r_t is the lower turning point (measured from the solar center in Mm) of waves with a given phase speed. Under this scheme, the phase-speed

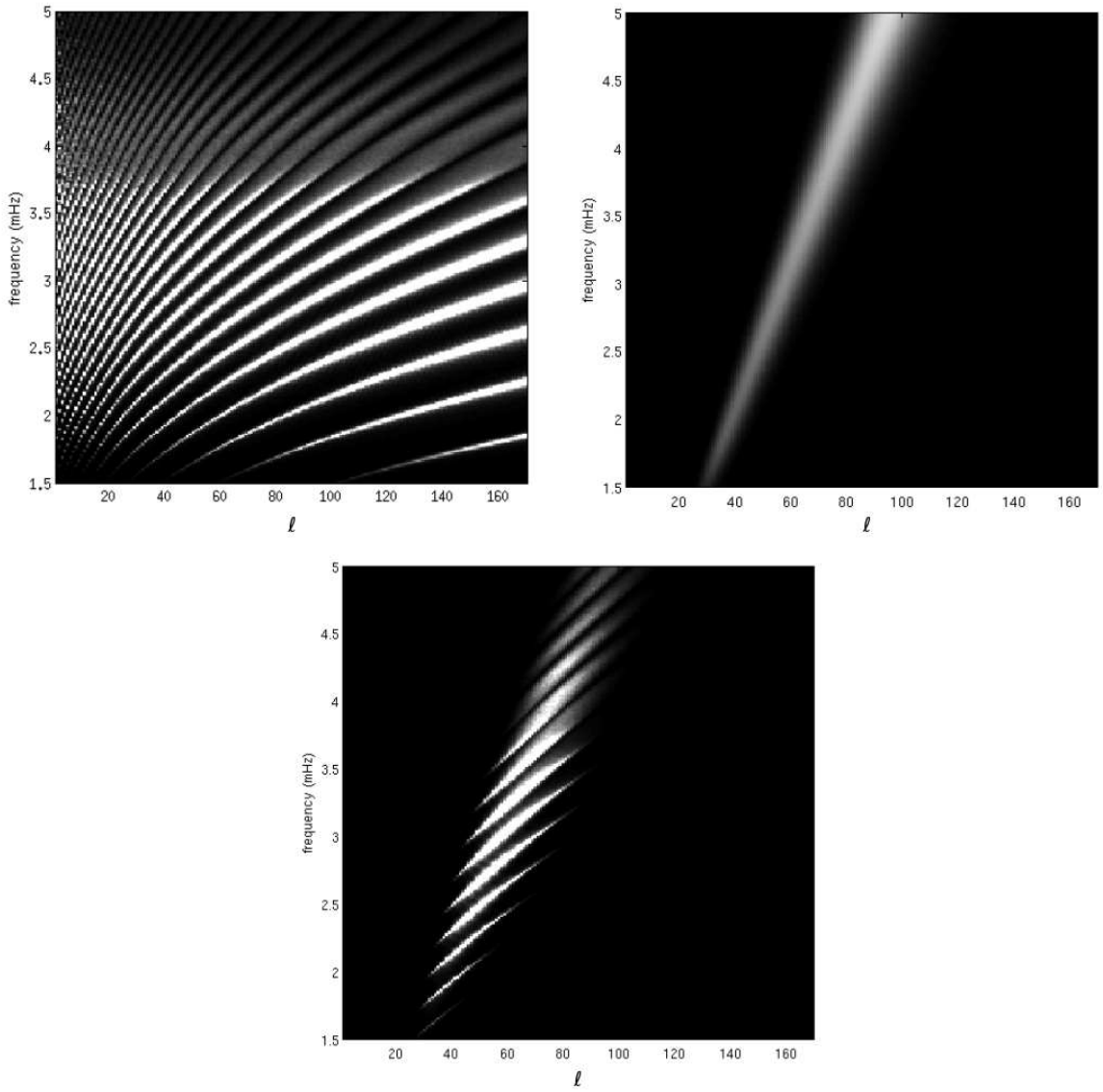

Figure 2.4: Top left panel shows power spectrum of unfiltered acoustic wave simulation data (Hartlep et al., 2013) with embedded meridional flow (Rempel, 2006) as a function of frequency and spherical harmonic degree l. Top right panel shows power spectrum of a phase-speed filter centered at skip distance $\Delta = 22.8°$ or solar radius $0.86R_\odot$ with a FWHM of 7° in skip distance or $0.05R_\odot$ in solar radius. Bottom panel shows power spectrum of filtered acoustic wave simulation data resulting from the product of the power spectra in the top panels.

filter width narrows with increasing phase speed or increasing focal-depth. Thus, the increased noise level in the measurements at larger focal-depths is compensated by the decrease in filter width. The constant in Equation (2.15) was chosen empirically so that the narrowest filter did not exclude too much signal, and the broadest filter was not too permissive. This filtering scheme was compared to another with a constant width in l regardless of the phase speed, and the results of the filtering by both schemes were consistent within error bars. Though important, these results are not directly relevant to this dissertation and are not presented here. They will be part of future work where the author attempts a more systematic filter design.

Some results of phase-speed filtering of simulation and solar data used in this dissertation are presented in Figures 2.4 and 2.5 respectively. Figure 2.4 shows the effect of phase-speed filtering on the power spectra of the acoustic wave simulation (Hartlep et al., 2013) with embedded meridional flow (Rempel, 2006), and Figure 2.5 compares the north-south travel-time shifts from time-distance analysis of 10 days of unfiltered and phase-speed filtered HMI data.

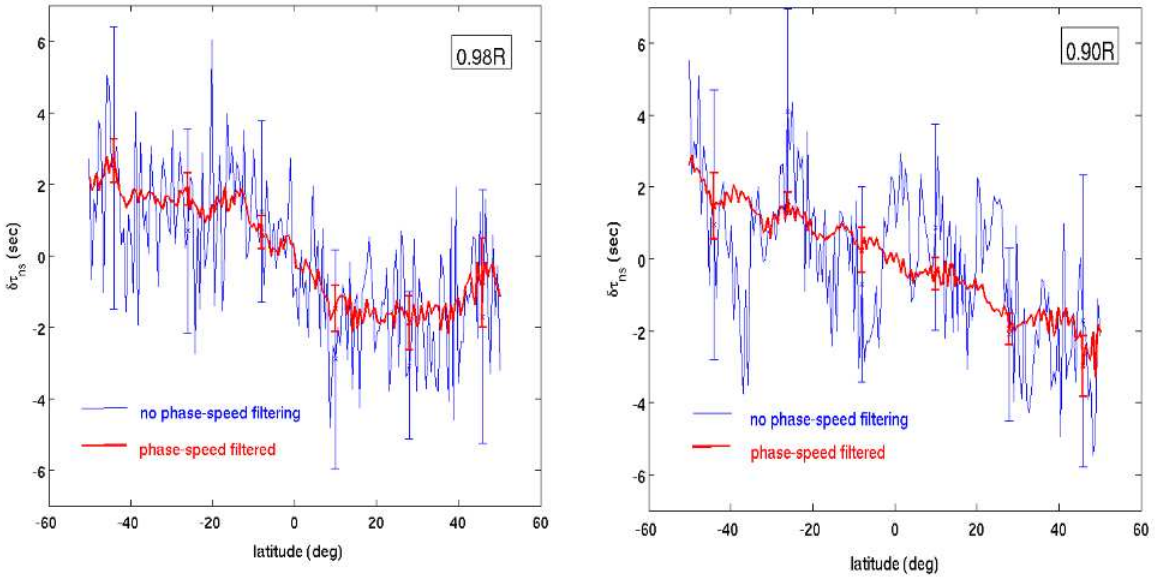

Figure 2.5: Plots of north-south travel-time shifts ($\delta\tau_{\rm ns}$) obtained from time-distance analysis of HMI data (10 days in May 2010) with quadrant 5-pairs deep-focus geometry, as a function of latitude, for the phase-speed filtered (red) and unfiltered case (blue), at focal depths of $0.98R_\odot$ (left) and $0.90R_\odot$ (right).

2.2.2 Cross-Covariance Function

The wave distortions can be measured as perturbations of wave travel times, which can be used as a diagnostic for perturbations or inhomogeneities along the wave travel path. However, because of the stochastic nature of solar waves it is impossible to track individual wave fronts or identify distinct wave sources. Instead, a cross-covariance function is used that provides a statistical measure of the wave distortion (e.g., Kosovichev and Duvall, 1997; Giles, 2000; Gizon et al., 2010):

$$\psi(\mathbf{r}_1, \mathbf{r}_2, \tau) = \int_0^T \phi(\mathbf{r}_1, t)\phi^*(\mathbf{r}_2, t+\tau)\mathrm{d}t, \tag{2.16}$$

where ϕ is the inverse Fourier transform of the filtered (Fourier-domain) signal in Equation (2.13), the two points $\mathbf{r}_1$ and $\mathbf{r}_2$ are coordinates on the solar surface, T is the total duration of observations. The time delay or time lag τ measures the

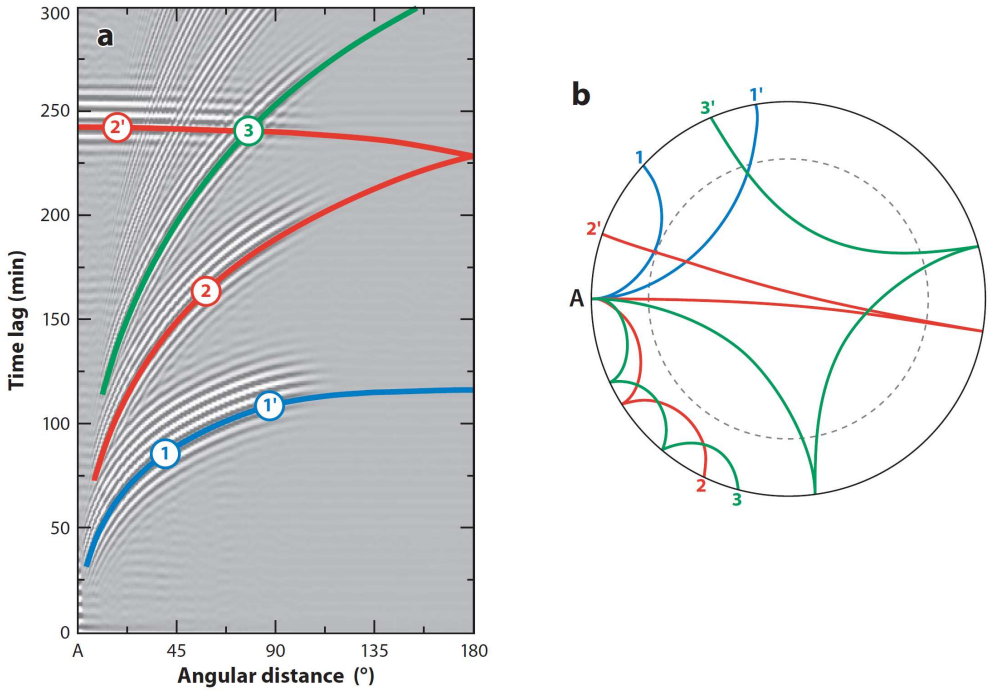

Figure 2.6: (a) Time-distance diagram for MDI medium-l data as a function of angular-separation distance and time lag. Positive values are white; negative values are black. The observation duration is 144 days starting in May 1996. (b) Ray paths for acoustic wave packets computed for solar Model S (Christensen-Dalsgaard et al., 1996). In (a) and (b), the blue lines correspond to single-skip ray paths, the red lines to two-skip ray paths, and the green lines to three-skip ray paths. Courtesy: Gizon et al. (2010).

amount that one signal is temporally shifted relative to the other. Figure 2.6(a) shows a cross-covariance function (time-distance diagram) measured from 144 days of MDI medium-l data. It provides a way to measure the wave travel time between two surface locations.

Ray paths reasonably approximate the propagation of wave energy if the wavelength is assumed to be much smaller than the length scales associated with the variations in the background solar model. Figure 2.6(b) shows ray paths computed from a standard solar model (see also Figure 2.3). The ridges in the time-distance diagram in Figure 2.6(a) correspond to different paths that the wave packet takes between pairs of observation points. For example, the blue line corresponds to single-skip arrivals (i.e., waves that visit their lower turning points once between the two observation points). The fine structure of the ridges reflects the band-limited nature of the power spectrum. Since most of the wave power is concentrated in the 3 mHz range, the cross-covariance function shows fine structure with a period of about 5 minutes. The other ridges seen in the time-distance diagram correspond to multiple skips. As can be seen in the ray paths in Figure 2.6(b), the depth of the lower turning point increases with the distance the ray travels in a single skip. Figure 2.7 shows the relationship to be almost linear, so that either quantity can be used as a proxy for the other when plotting travel-time shifts, at least within the convection zone of the Sun.

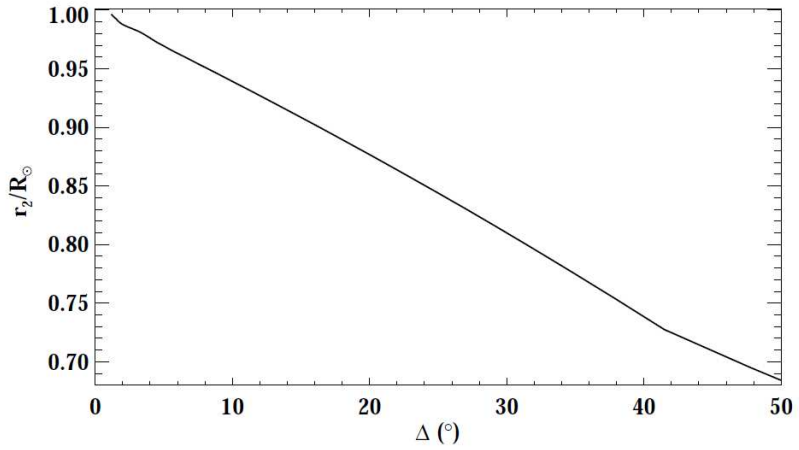

Figure 2.7: Plot of the nearly linear relationship between the single-skip distance or angular-separation distance and the lower turning point for acoustic rays with a frequency of 3.1 mHz. Courtesy: Giles (2000).

2.2.3 Deep-Focus Geometry

Duvall (1995) discussed for the first time the application of the deep-focusing scheme in time-distance analysis of deep subsurface structures. In Duvall and Kosovichev (2001) this scheme was carried out by cross-correlating points that are located on opposite sides of a circle with the map point as the center, to measure sound-speed perturbations below active regions. Duvall (2003) divided up the circle into quadrants oriented in the cardinal directions, to measure subsurface flows in those directions by cross-correlating diametrically opposite points in opposite quadrants (cf. Figures 2.8 and 2.9). In Figure 2.8, diametrically opposite points in the arcs A and A$'$ are cross-correlated in time, and then again in arcs A$'$ and A—the order of the cross-correlation is important for the determination of flows in opposite directions. The positive and negative time-lag branches also give information about opposite flow directions. The reader is referred to Figure 2.8 and the caption therein to understand how points in the various arcs are cross-correlated. Figure 2.9 nicely illustrates the quadrant deep-focus geometry with respect to the spherical Sun.

The following nomenclature is adopted in this work: if there are N pairs of arcs, where N must be an odd positive integer, the configuration is referred to as the *N-pairs* deep-focus geometry. The simplest case, the 1-pair geometry is just the common-midpoint case. In full deep-focus geometry, the rays intersect at the lower turning point of the common-midpoint ray. This point is called the *focal-depth*, the depth of observation of the perturbation of interest, e.g., meridional flow. Thus, not only the waves that have the same lower turning point as the focal-depth contribute to the travel time signal, but potentially all waves with ray paths intersecting at the focal-depth can contribute to the travel-time signal, greatly improving the signal-to-noise ratio. A limit may be set to the number of ray paths to include in time-distance analysis of meridional flow by the consideration that ray paths that are closer to being radial at the focal depth are less sensitive to meridional flows, and hence contribute less to the meridional flow induced travel-time shift.

The cross-covariance function computed between two spatial points is in general very noisy. Spatial averaging is applied to improve the signal-to-noise ratio. This is done by averaging the cross-covariance functions of the individual pairs of points over the arcs. For the common-midpoint case this is simply accomplished for there is only one pair of arcs and a single separation distance to consider; so one ends up with two cross-covariance functions (after the spatial averaging) that constitute

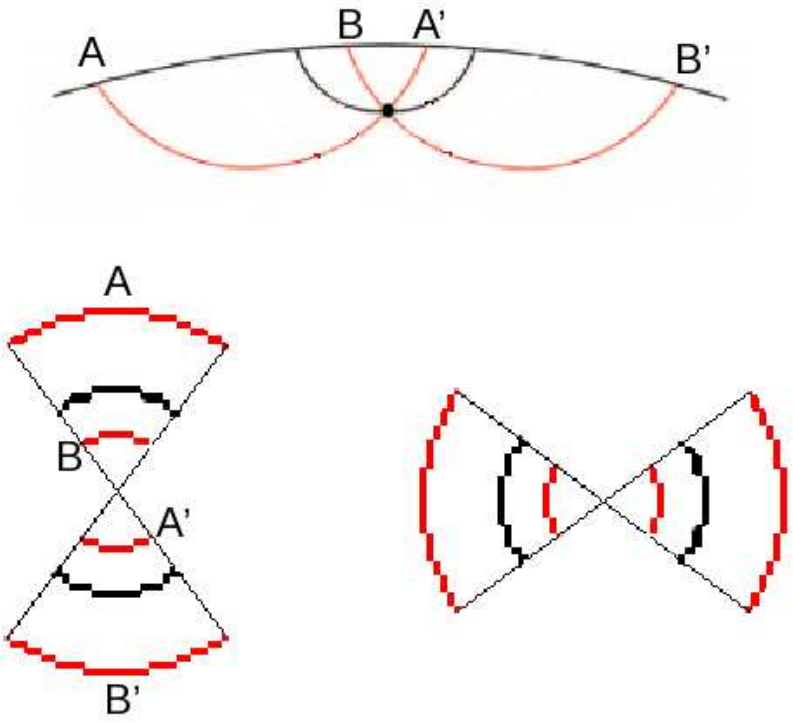

Figure 2.8: A simple example of the deep-focus geometry to illustrate the common-midpoint and full deep-focus schemes. Top: Radial view with subsurface ray paths. The point where the rays intersect is the *focal-depth*, the depth where the perturbation of interest is being measured. Bottom: Surface view in the north-south (left) and east-west (right) orientations. The figures also illustrate the fact that the common-midpoint deep-focus geometry (black; not including the surface which is also in black in the top figure) is a special case of the full deep-focus geometry (the red and the black). The full deep-focus geometry has 3 pairs of arcs, and is thus referred to as the *3-pairs* deep-focus geometry (or N-pairs as the case may be, where N is an odd number). The sector angles are unspecified, but for the quadrant geometry they are 90°. Referring to bottom left scheme: diametrically opposite points or pixels in the arcs [black(up)-black(down), A-A′, B-B′, black(down)-black(up), A′-A, B′-B] are cross-correlated. The first three give information about southward flow at $t > 0$ and northward flow at $t < 0$, and just the reverse for the second three. The cross-covariances A-A′ and B-B′ can be averaged together to improve the signal-to-noise since they are not only oriented in the same direction (southward for $t > 0$, northward for $t < 0$), they also comprise pixels in opposite arcs with the same separation distance. So on and so forth for the other pairs of arcs. The positive and negative time-lag branches are kept separate until all the spatial averaging has been carried out, at which point they are fit with Gabor wavelet functions and the extracted travel times differenced (Section 2.2.4).

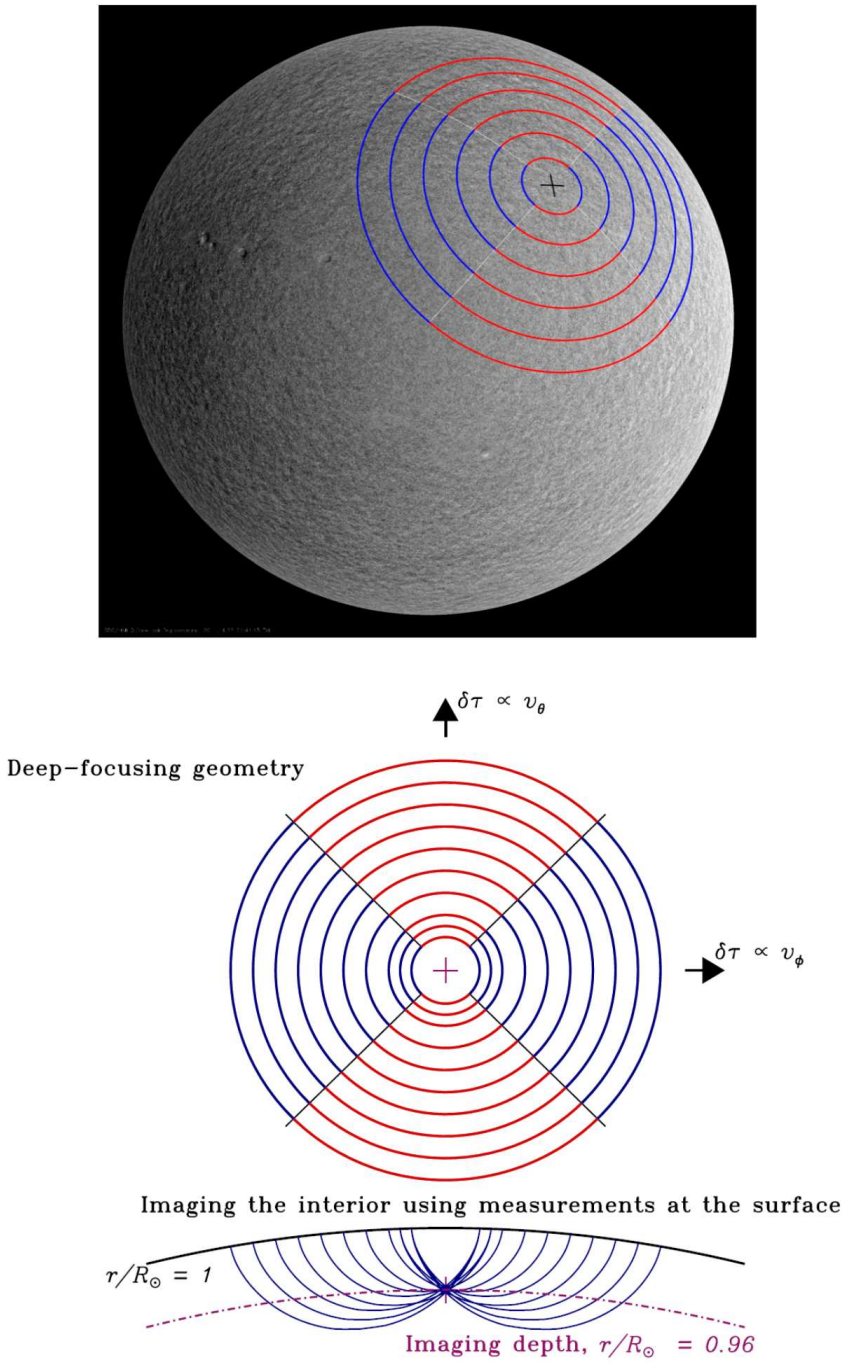

Figure 2.9: Top: A realistic example of a full deep-focusing scheme applied to a line-of-sight HMI Dopplergram. Bottom: Projections in the horizontal and radial planes of a deep-focusing scheme with a focal-depth of $0.96R_\odot$. Courtesy: Hanasoge et al. (2012).

the positive and negative time-lag branches which are then fit with Gabor wavelet functions and the extracted travel times differenced as described in Section 2.2.4. For the more complicated full deep-focus case, there are several pairs of arcs each at different separation distances. The cross-covariances of the different distances cannot be averaged directly. A model travel-time curve is used to estimate the travel time of the mean of the different distances. Then the different cross-covariance functions at the different distances are shifted by the difference between the estimated travel time for the different distances and the estimated travel time for the mean distance. The shifted cross-covariance functions are then averaged together. This shifting and averaging operation is illustrated in Figure 2.10 for surface gravity f modes and for the *surface*-focusing scheme (cf. Duvall and Kosovichev, 2001), but these operations can also be carried out on p-mode data with the full deep-focus technique.

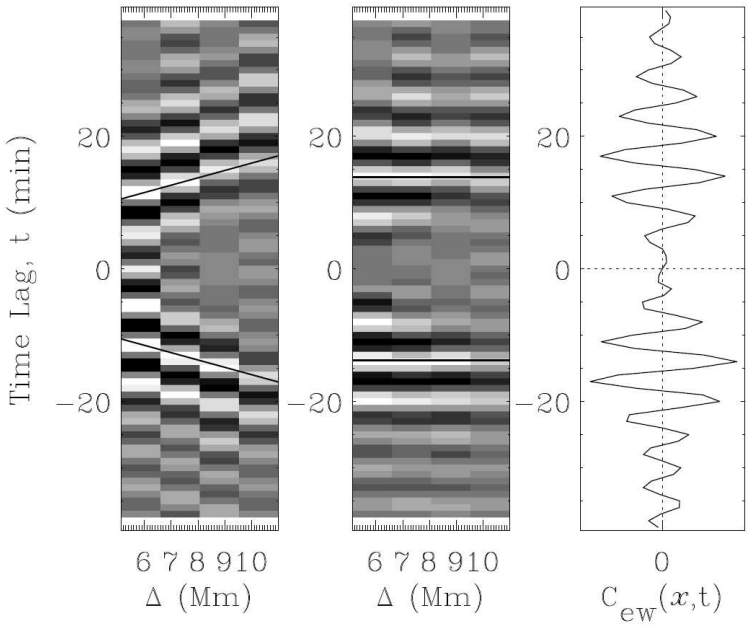

Figure 2.10: Left: Cross-covariance functions $C_{\rm ew}(x, \Delta, t)$ for f modes, measured at pixel position x and for distances in the range 5.1 Mm $< \Delta <$ 11 Mm, using a surface-focusing technique, obtained from 8 hours of full-disk MDI data. Middle: Cross-covariance functions are shifted along a line of constant phase for averaging over the specified range of Δ. Right: Average cross-covariance $C_{\rm ew}(x, t)$ calculated from shifted cross-covariances in middle panel. This type of shifting and averaging is routinely carried out on cross-covariances calculated from p-mode data using the deep-focusing technique. Courtesy: Hindman et al. (2004).

2.2.4 Gabor-Wavelet Fitting

From the cross-covariance function it is possible to make estimates of the acoustic travel times between pairs of locations on the solar surface. In this dissertation the Gabor-wavelet fitting method is used for travel-time measurements.

The Gabor-wavelet function has the form (cf. Kosovichev and Duvall, 1997; Kosovichev, 2011; Giles, 2000):

$$G_{\pm}(\tau) = A\cos[\omega_0(\tau - \tau_{\pm})]\exp\left[-\frac{\delta\omega^2}{4}(\tau - \tau_{\rm g})^2\right]. \tag{2.17}$$

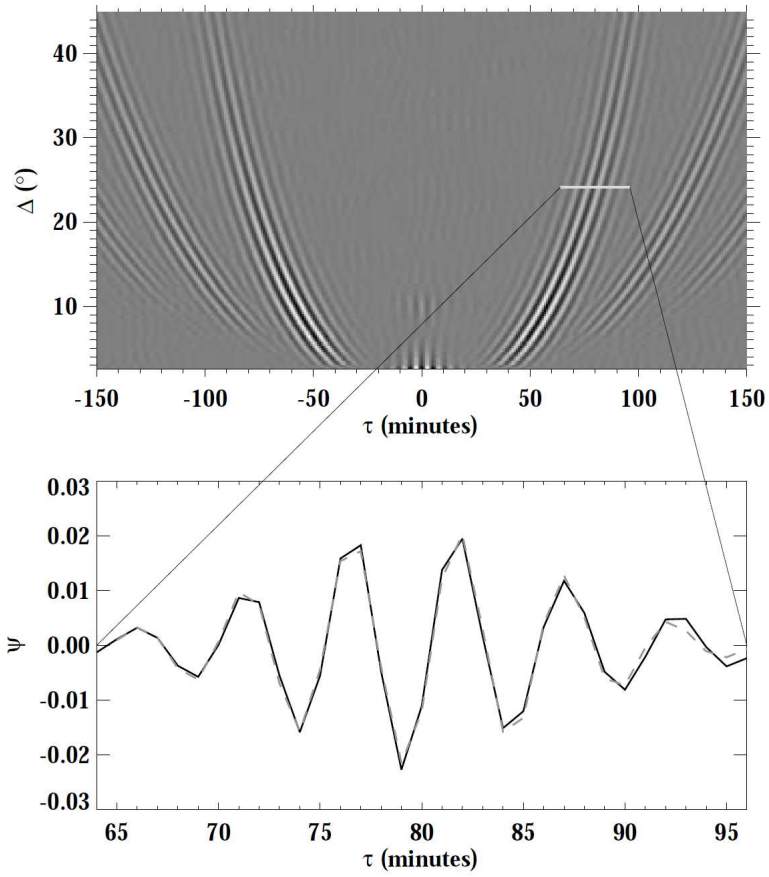

Figure 2.11: A time-distance diagram with typical cross-covariances is displayed. In the upper plot the cross-covariance amplitude is displayed as a function of time lag τ and skip distance Δ. The lower plot shows the cross-covariance function (solid line) in the positive time-lag branch, for skip distance $\Delta = 24.1^\circ$ along the cut indicated in the upper plot. The lower plot also shows the Gabor-wavelet fit $G_+(\tau)$ (dashed line). Courtesy: Giles (2000).

$G_+(\tau)$ and $G_-(\tau)$ are fit to the positive and negative time-lag branches, respectively (Figure 2.11). The fit parameters are the amplitude A, the central frequency ω_0, the frequency bandwidth $\delta\omega$, the group travel time $\tau_{\rm g}$, and the phase travel times of the positive and the negative branches τ_+ and τ_-, respectively. The phase travel times are significantly less noisy than the group travel times, and therefore, it is customary to use the phase travel time measurements, although the group travel time is the truer measure of travel time of a wave packet. The other fit parameters can potentially provide pertinent information when acoustic waves interact with magnetic fields, such as in the vicinity of active regions.

The travel-time differences or travel-time shifts $\delta\tau_{\rm diff} = \tau_+ - \tau_-$ are mostly sensitive to flows while the mean travel times $\delta\tau_{\rm mean} = (\tau_- + \tau_+)/2$ are sensitive to sound-speed perturbations. Since this dissertation is concerned with flows, only the travel-time shifts are relevant.

2.2.5 Ray-Theoretic Forward Model

The wavefield in a given region of the solar surface is affected by the properties of that region, which include the subsurface layers down to the depth of penetration determined by the lower turning point of the waves. By analyzing the properties of such local waves it is possible to infer the local three-dimensional structures and flows beneath the solar surface. A basic difficulty with time-distance helioseismology, which has not yet been fully solved, is the treatment of the *forward* problem, i.e., the calculation of the wave field and the resulting observables for a given subsurface structure and flow. As a result, the inferences made through time-distance analysis are somewhat difficult to interpret, in terms of their resolution and the extent to which they reflect the true properties of the solar interior.

The ray-theoretic forward model or the ray approximation, in which the wavelength is small compared to the other length scales in the problem (e.g., the scale heights of the reference model, and the length scales of the perturbations), has been used extensively in time-distance helioseismology (e.g., Kosovichev, 1996; Giles, 2000; Hartlep et al., 2013; Zhao et al., 2013; Duvall and Hanasoge, 2013; Duvall et al., 2014) to compute travel-time sensitivity kernels and travel-time shifts, in spite of known deficiencies (e.g., Bogdan, 1997; Birch and Gizon, 2007).

It was shown by (Kosovichev and Duvall, 1997), assuming that the travel times

are only sensitive to perturbations along the ray path, to first-order approximation the travel-time difference due to flow velocity $\mathbf{v}$, and the mean of the reciprocal travel time perturbations due to structural inhomogeneities are given by

$$\delta\tau_{\mathrm{diff}} = -2\int_{\Gamma_0} \frac{\mathbf{v}\cdot\hat{\mathbf{n}}}{c^2}\mathrm{d}s, \tag{2.18}$$

$$\delta\tau_{\mathrm{mean}} = -\int_{\Gamma_0}\left[\frac{\delta c}{c}\frac{k}{\omega} + \frac{\delta\omega_{\mathrm{ac}}}{\omega_{\mathrm{ac}}}\frac{\omega_{\mathrm{ac}}^2}{c^2\omega^2}\frac{\omega}{k} + \frac{1}{2}\left(\frac{c_{\mathrm{A}}^2}{c^2} - \frac{(\mathbf{k}\cdot\mathbf{c}_{\mathrm{A}})^2}{k^2c^2}\right)\frac{k}{\omega}\right]\mathrm{d}s, \tag{2.19}$$

respectively, where c is the adiabatic sound speed, $\hat{\mathbf{n}}$ is a unit vector tangent to the ray path, s is the distance along the ray, ω_{ac} is the acoustic cut-off frequency, $\mathbf{c}_{\mathrm{A}} = \mathbf{B}/\sqrt{4\pi\rho}$ is the Alfvén velocity, $\mathbf{B}$ is the magnetic field, and ρ is the plasma density. The integration is performed along the unperturbed ray path Γ_0 according to Fermat's principle (cf. Gough, 1993). Since this dissertation is solely concerned with the measurement of flows, only travel-time differences or shifts due to flows will be of relevance in the rest of this work.

Chapter 3

Forward Modeling with Ray Theory and Simulations

Inferring meridional flow velocity from travel times measured on the photosphere, i.e., the *inverse* problem, is a difficult affair given that the solar convection zone is a hotbed of complex turbulent magnetohydrodynamic processes. The difficulty lies in interpreting the time lags calculated from cross-correlating pixels of Doppler velocity datacubes without an accurate model of the relevant processes in the solar interior that are manifested in the images. Conversely, it is hoped that the model will be obtained, or at least constrained, by this very cross-correlation technique of time-distance helioseismology. The way out of this circularity is to hypothesize a model, such as, the time lags correspond to travel times of propagating acoustic waves that are affected in certain predictable and preferably linear ways by other phenomena, such as, magnetic fields, plasma flows, etc. in the solar convection zone. Incidentally, these latter phenomena may be nonlinearly coupled, potentially making it difficult, if not impossible, to disentangle them with travel-time measurements. The theoretic values are eventually compared with the observed values, and the residue between them, if significant, is accounted for by introducing additional complexity or phenomena or systematic errors in the current model, or even by substituting alternate models. This process is carried out until reasonable agreement is obtained between the theoretic and the observed values. In the face of such unwieldy prospects, it is often expedient to postulate simple relationships and to experiment with simple objects, thus allowing for the assessment of the basic theory underlying a measurement technique without getting lost in the intricacies.

In this work the correspondence between cross-correlation time delays and wave travel times, and their modification by meridional flow is modeled by ray theory, which is then tested against time lags calculated from three-dimensional numerical simulations of acoustic wave propagation in a spherical domain with embedded axisymmetric meridional flow (Section 3.1). The numerical simulation is an oversimplified non-magnetic model of the interaction between solar oscillations and meridional flow which allows for a convenient way to validate the correspondence between the time lags or time-distance measurements and the ray-theoretic travel times of acoustic waves in the presence of meridional flow. More accurately, the ray-theoretic travel-time differences or travel-time shifts of counter-propagating waves in the presence of meridional flow are compared with the differences between the positive and negative cross-correlation time lags, or time-lag shifts, in an effort to validate the time-distance helioseismic technique, without drowning in the turbulent magnetohydrodynamic details of the solar convection zone. Thus, the *forward* problem is formulated, wherein the meridional flow velocity is known beforehand and is used to determine the travel-time shift via ray theory (Section 3.2), which is then compared to the travel-time shift computed by time-distance (cross-correlation) analysis of simulated "observations" containing information about the same meridional flow (Section 3.3).

3.1 Acoustic Wave Propagation Simulations

Two different implementations of three-dimensional numerical simulations of acoustic wave propagation in a spherical domain are used in order to objectively evaluate ray theory as a model for interpreting travel-time shifts due to meridional flow. They are described in Hanasoge et al. (2006) (henceforth referred to as HLD06) and Hartlep et al. (2013) (henceforth referred to as HZK13) respectively, and their power spectra are shown in Figure 3.1. Both HLD06 and HZK13 solve the three-dimensional Euler equations of fluid motion in a spherical geometry, linearized around a spherically symmetric and stationary background state characterized by density, pressure or sound speed, mass flows, and acceleration due to gravity. In both cases the wave propagation is assumed to be adiabatic, and the source of wave excitation is random which peaks about a couple of hundred kilometers below the upper boundary. Also, in both cases absorbing buffer layers are implemented at the boundaries to effect non-reflecting boundary conditions.

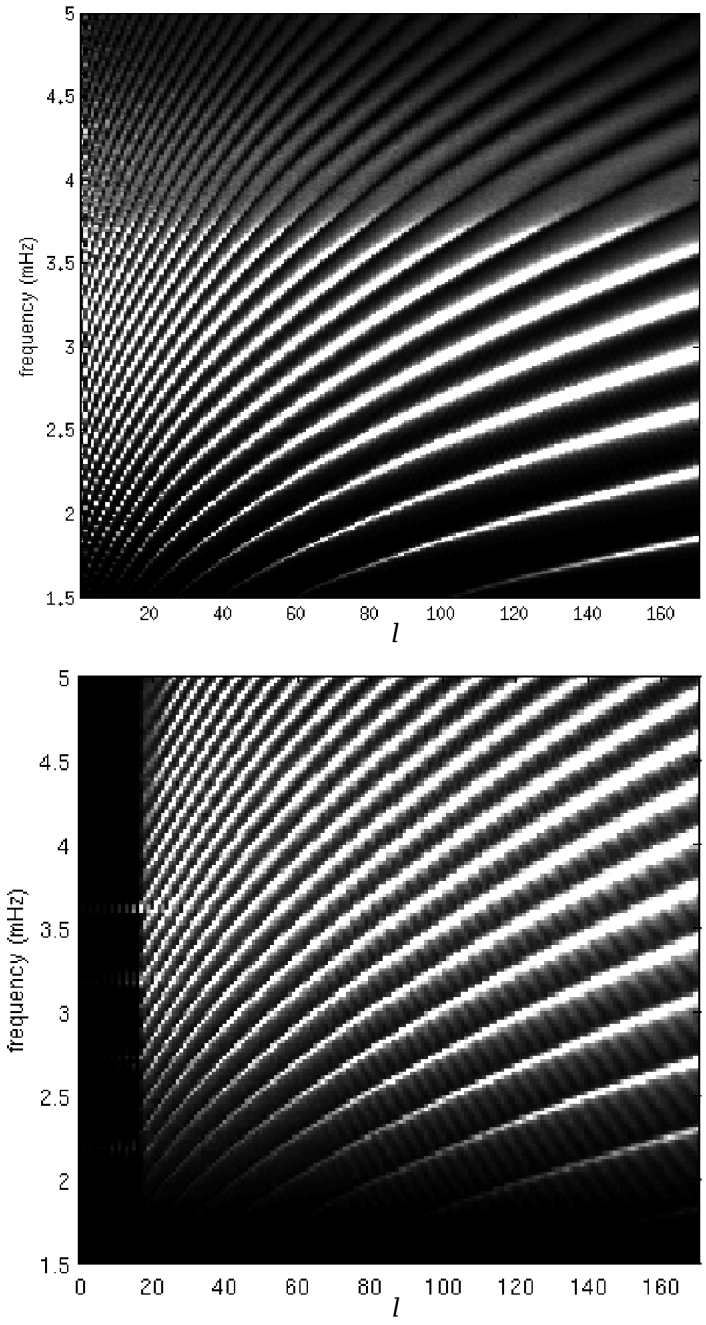

Figure 3.1: Power spectra (vertical axis: frequency in mHz; horizontal axis: spherical harmonic degree l) of simulated acoustic wave propagation in spherical geometry with single-cell R06 (Rempel, 2006) meridional flow (max. flow speed = 500 m/s). Top: HZK13 (Hartlep et al., 2013); Bottom: HLD06 (Hanasoge et al., 2006). The HLD06 spectra extends in spherical harmonic degree to a maximum of $l = 255$, but is not shown in figure to keep the same scale as the HZK13 spectra which only extends to a maximum of $l = 170$. Also apparent is the lower acoustic cut-off frequency in the HZK13 spectra (reduced power above about 3.7 mHz).

There are, however, important differences. Both HLD06 and HZK13 employ Model S (Christensen-Dalsgaard et al., 1996) as the background solar model (for the most part), which is convectively unstable in the near-surface layers of the convection zone. But they take different approaches to achieve convective stability: HLD06 ensures stability in the outer convective envelope by replacing the near-surface layers (above $0.98R_\odot$) by an alternative empirical description that satisfies the requirements of hydrostatic consistency and convective stability, and also preserves the reflective property of the solar atmosphere, whereas HZK13 sets the entropy gradient, or the Brunt-Väisälä frequency, to zero everywhere in the computational domain to make the linearized Euler equations convectively stable. Two consequences follow from the latter approach: the acoustic cut-off frequency is slightly reduced (cf. Figure 3.1), and no separate energy equation needs to be solved. Other differences include: HLD06 has a lower boundary at $0.2R_\odot$, HZK13 does not; HLD06 introduces a radially directed dipole source in the equation of momentum, HZK13 introduces a source that is random in time and horizontal space in the equation of continuity to mimic the excitation of acoustic perturbations; HLD06 resolves spherical harmonic degrees from 20 to 255, HZK13 resolves spherical harmonic degrees from 0 to 170. For further details on each of these implementations, especially the computational aspects, the reader is referred to Hanasoge et al. (2006), Hanasoge and Duvall (2007), Hartlep et al. (2008), and Hartlep et al. (2013).

3.2 Ray-Theoretic Analysis and Results

In order to characterize the ray-theoretic travel-time shifts, it is necessary to check the sensitivity of the computed values to changes in time-distance geometry, relevant parameters (e.g., acoustic cut-off frequency, Brunt-Väisälä frequency) or background states (e.g., background solar model, meridional flow model). In the following, the deep-focus time-distance geometry, the meridional flow model, seismic parameters such as the acoustic cut-off frequency and the Brunt-Väisälä frequency, and the background solar model are varied to determine the ramifications for ray-theoretic travel-time shifts.

The ray-theoretic travel-time shift due to flow velocity $\mathbf{v}$ is discussed in Section

2.2.5, and Equation (2.18) is reproduced here for the reader's convenience:

$$\delta\tau = -2 \int_{\Gamma_0} \frac{\mathbf{v} \cdot \hat{\mathbf{n}}}{c^2} \mathrm{d}s, \tag{3.1}$$

where c is the sound speed, Γ_0 is the unperturbed (absence of flow) ray path, $\hat{\mathbf{n}}$ is a unit vector tangent to the ray path, and s is the distance along the ray. The ray generation and integrations along the ray path in spherical geometry to compute travel-time shifts are performed using code developed and discussed by Giles (2000). This code was extended by T. L. Duvall, Jr. to integrate ray paths in quadrant/annulus surface-focus/deep-focus geometries for three-dimensional flow models and sound-speed perturbation models. The code is further extended by the author to include various definitions of acoustic cut-off frequency, different background solar models, and generating and integrating ray paths in Cartesian geometry.

3.2.1 Meridional Flow Model

Three different meridional flow models are chosen for differences in flow structure, such as, flow velocity gradients, double-cell vs. single-cell structure, to study the effect of these structural differences on travel-time shifts. These models are depicted in Figures 3.2–3.4 with the maximum flow speed adjusted to 15 m/s. The flow model in Figure 3.2 is a single-cell meridional flow resulting from the combined mean-field hydrodynamic and dynamo equations in Rempel (2006) (henceforth R06). The model in Figure 3.3 is another single-cell meridional flow model generated using Equations (58–61) in van Ballegooijen and Choudhuri (1988) (henceforth BC88). Figure 3.4 shows a radial double-cell meridional flow model generated using the stream function given in Section 3.2.1 of Jouve and Brun (2007) (henceforth JB07). Both the single-cell models have the stagnation point at about $0.8R_\odot$. The double-cell model has the shallower stagnation point at about $0.91R_\odot$, and the deeper one at about $0.72R_\odot$.

Ray-theoretic computations of travel-time shifts on these meridional flow models are carried out with the common-midpoint deep-focusing technique, using the isothermal acoustic cut-off frequency (cf. Section 2.1.2 or 3.2.3) and Model S as the background solar model. The results of these computations, the north-south or meridional travel-time shifts ($\delta\tau_{\mathrm{ns}}$), are shown as a function of focal depth ($r/R_\odot$) at 45°S latitude in Figure 3.5.

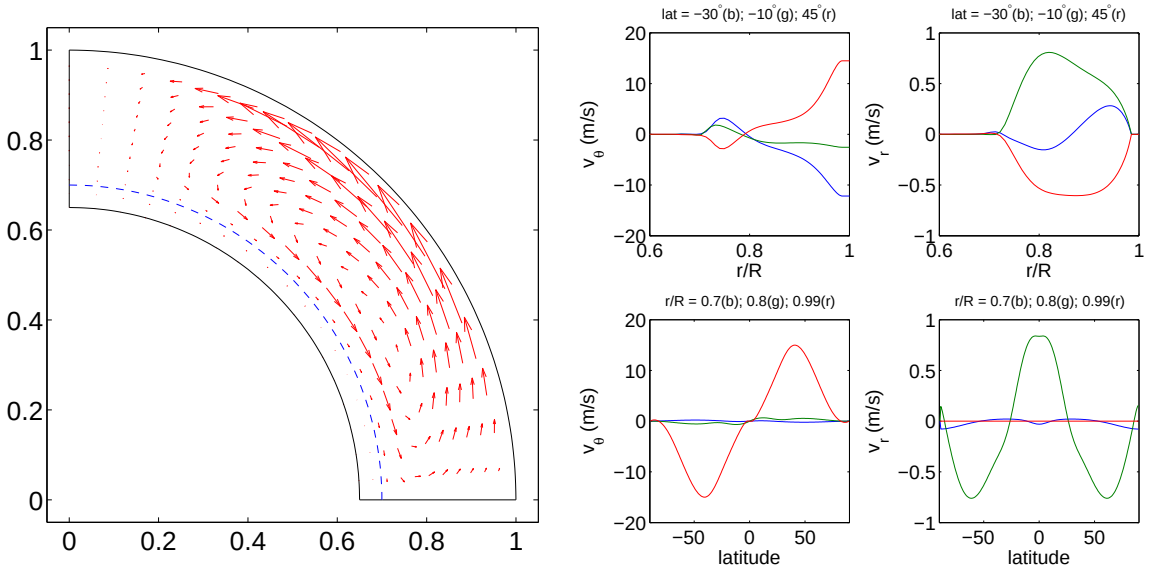

Figure 3.2: Left: Single-cell meridional flow model (R06) resulting from combined mean-field hydrodynamic and dynamo equations in Rempel (2006). Blue dashed line marks the base of the convection zone. Right: Colatitudinal (v_θ) and radial (v_r) components of meridional flow in left panel at select latitudes (30°S: blue; 10°S: green; 45°N: red) and radii ($0.7R$: blue; $0.8R$: green; $0.99R$: red) as functions of depth (r/R, $R = R_\odot$) and latitude. The maximum flow speed is set to 15 m/s.

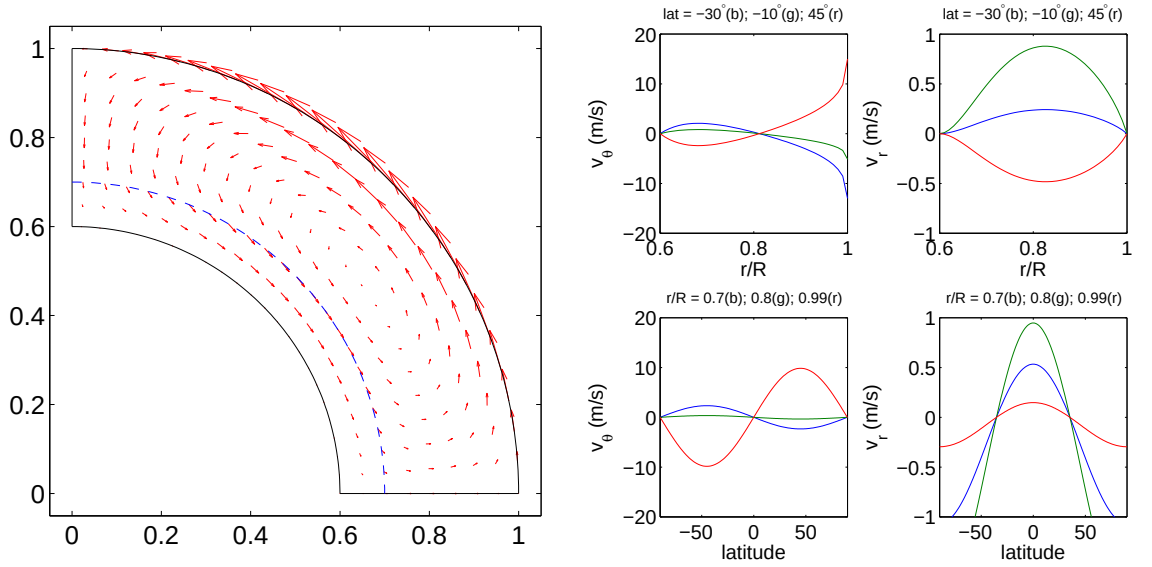

Figure 3.3: Left: Single-cell meridional flow model (BC88) generated using Equations (58–61) in van Ballegooijen and Choudhuri (1988). Blue dashed line marks the base of the convection zone. Right: Colatitudinal (v_θ) and radial (v_r) components of meridional flow in left panel at select latitudes (30°S: blue; 10°S: green; 45°N: red) and radii ($0.7R$: blue; $0.8R$: green; $0.99R$: red) as functions of depth (r/R, $R = R_\odot$) and latitude. The maximum flow speed is set to 15 m/s.

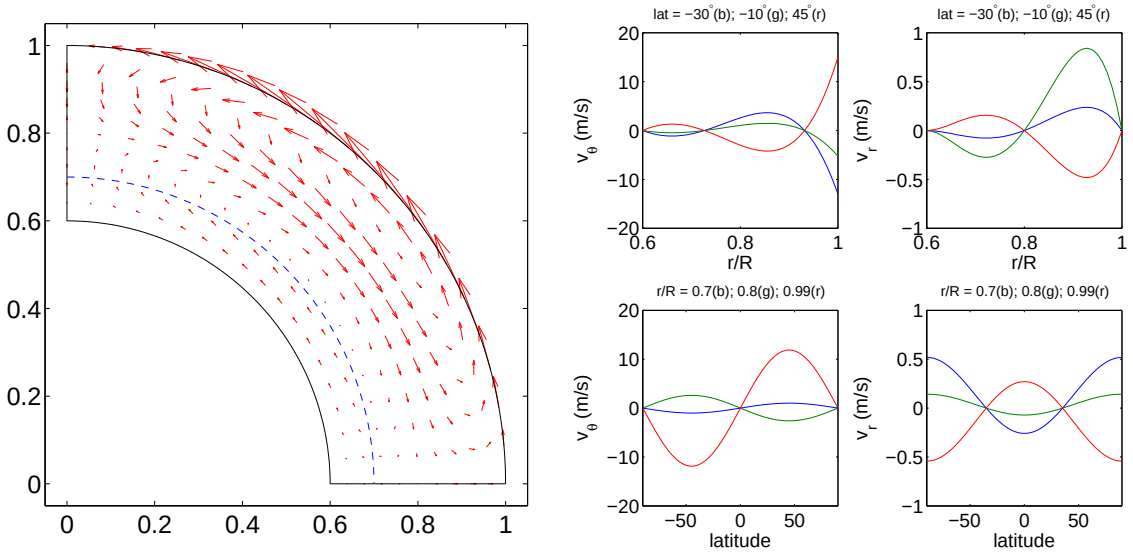

Figure 3.4: Left: Double-cell (in radius) meridional flow model (JB07) generated using the stream function given in Section 3.2.1 of Jouve and Brun (2007). Right: Colatitudinal (v_θ) and radial (v_r) components of meridional flow in left panel at select latitudes (30°S: blue; 10°S: green; 45°N: red) and radii ($0.7R$: blue; $0.8R$: green; $0.99R$: red) as functions of depth and latitude. Max. flow speed is set to 15 m/s.

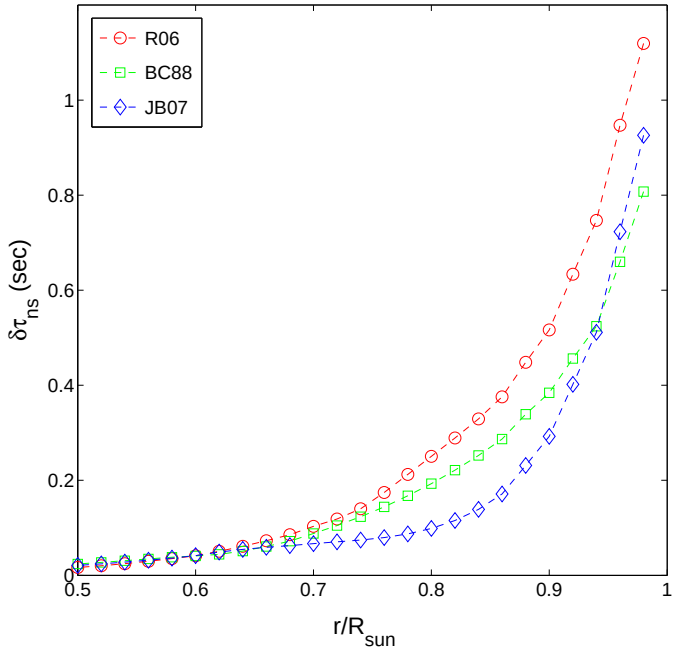

Figure 3.5: Ray-theoretic meridional travel-time shift ($\delta\tau_{\rm ns}$), in seconds, as a function of focal depth ($r/R_{\rm sun}$) at 45°S latitude, computed with the common-midpoint geometry. Ray paths are computed using the isothermal acoustic cut-off frequency ($\omega_{\rm ac} = c/2H_p$) and background solar Model S for different meridional flow models (max. flow speed = 13.5 m/s): single-cell R06 (red circles); single-cell BC88 (green squares); radial double-cell JB07 (blue diamonds).

3.2.2 Deep-Focus Geometry

The deep-focus geometry used in this work is discussed in Section 2.2.3. Various geometries are tested in the ray approximation: common-midpoint deep-focus, 3-pairs deep-focus, 5-pairs deep-focus, 9-pairs deep-focus, and 19-pairs deep-focus. The ray paths are calculated using the isothermal acoustic cut-off frequency and the background Model S, with the Brunt-Väisälä frequency set to zero in the dispersion equation used to generate the ray paths. The results of the meridional travel-time shift calculations for the various deep-focus geometries are shown in Figure 3.6.

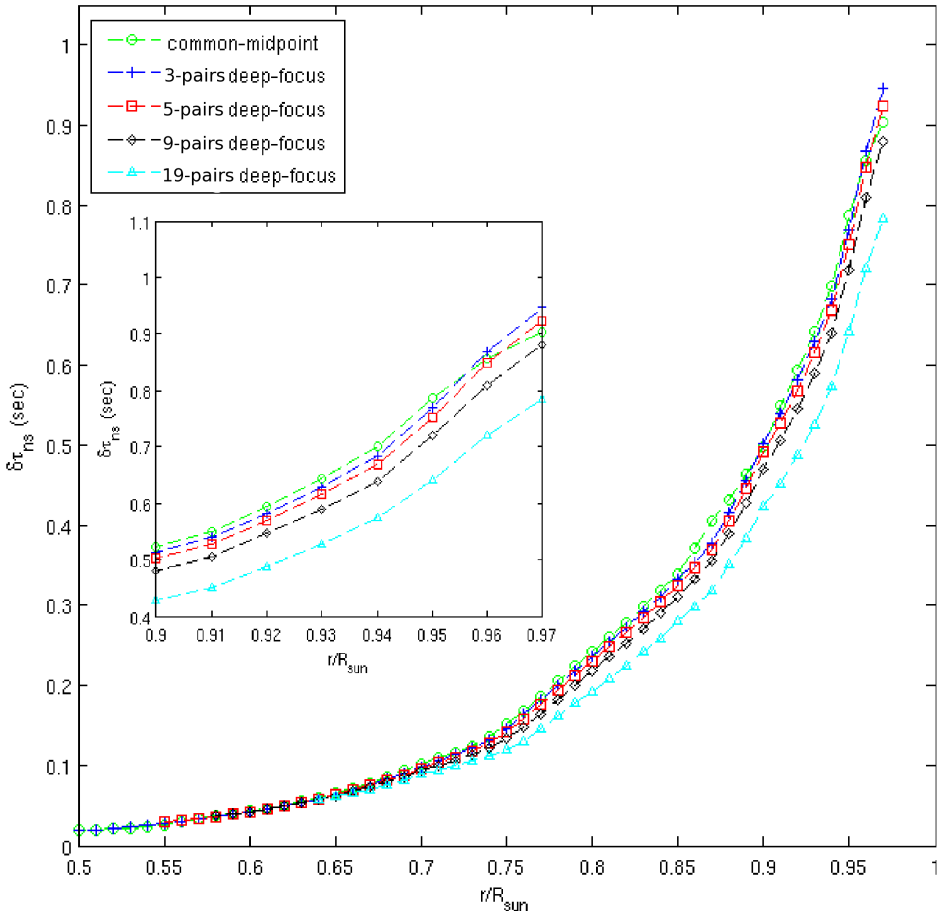

Figure 3.6: Ray-theoretic meridional travel-time shift ($\delta\tau_{\rm ns}$) as a function of focal depth ($r/R_{\rm sun}$) for single-cell R06 flow model (max. flow speed = 13.5 m/s) at 45°S latitude. Ray paths are computed using the isothermal acoustic cut-off frequency ($\omega_{\rm ac} = c/2H_p$) and the background Model S, with the Brunt-Väisälä frequency set to zero, for different quadrant geometries: common-midpoint (green circle); 3-pairs deep-focus (blue plus); 5-pairs deep-focus (red square); 9-pairs deep-focus (black diamond); 19-pairs deep-focus (cyan triangle). Inset expands the near-surface region.

3.2.3 Acoustic Cut-off Frequency

The acoustic cut-off frequency in near-surface layers of the convection zone determines the upper reflective boundary of the solar acoustic waves. The expression for this quantity depends on the background solar model and the oscillation equations. In this work the more common expressions for the acoustic cut-off frequency are used (e.g., Deubner and Gough, 1984; Aerts et al., 2010), and although this is discussed in Section 2.1.2, the formulas are reproduced here for the reader's convenience.

The generalized acoustic cut-off frequency is given by

$$\omega_{\rm ac}^2 = \frac{c^2}{4H^2}\left(1 - 2\frac{{\rm d}H}{{\rm d}r}\right), \tag{3.2}$$

where H is the density scale height:

$$H^{-1} = -\frac{{\rm d}\ln\rho}{{\rm d}r}. \tag{3.3}$$

In the case of an isothermal atmosphere $H = H_p$ is constant, where H_p is the pressure scale height defined as

$$H_p^{-1} = -\frac{{\rm d}\ln p}{{\rm d}r}, \tag{3.4}$$

and the generalized acoustic cut-off frequency reduces to the isothermal acoustic cut-off frequency:

$$\omega_{\rm ac} = \frac{c}{2H_p}. \tag{3.5}$$

To show the relevance of the acoustic cut-off frequency, the local dispersion equation used in the computation of ray paths is reproduced here (e.g., Deubner and Gough, 1984; Gough, 1993; D'Silva and Duvall, 1995):

$$k_r^2 = \frac{1}{c^2}(\omega^2 - \omega_{\rm ac}^2) - k_{\rm h}^2\left(1 - \frac{N^2}{\omega^2}\right), \tag{3.6}$$

where k_r is the radial wavenumber, $k_{\rm h} = \sqrt{l(l+1)}/r$ is the horizontal wavenumber with the spherical harmonic degree l, and N is the Brunt-Väisälä frequency given by (e.g., D'Silva and Duvall, 1995; Giles, 2000; Aerts et al., 2010)

$$N^2 = g\left(\frac{1}{\Gamma_1}\frac{{\rm d}\ln p}{{\rm d}r} - \frac{{\rm d}\ln\rho}{{\rm d}r}\right), \tag{3.7}$$

where $\Gamma_1 = (\partial \ln p / \partial \ln \rho)_s$ is the adiabatic index, the derivative taken at constant specific entropy s, and g is the acceleration due to gravity.

The effect of using the different cut-off frequencies for ray path computation on the meridional travel-time shifts is examined in Figure 3.7. Background Model S is used to calculate the ray paths, and the travel-time shifts are computed with the common-midpoint geometry.

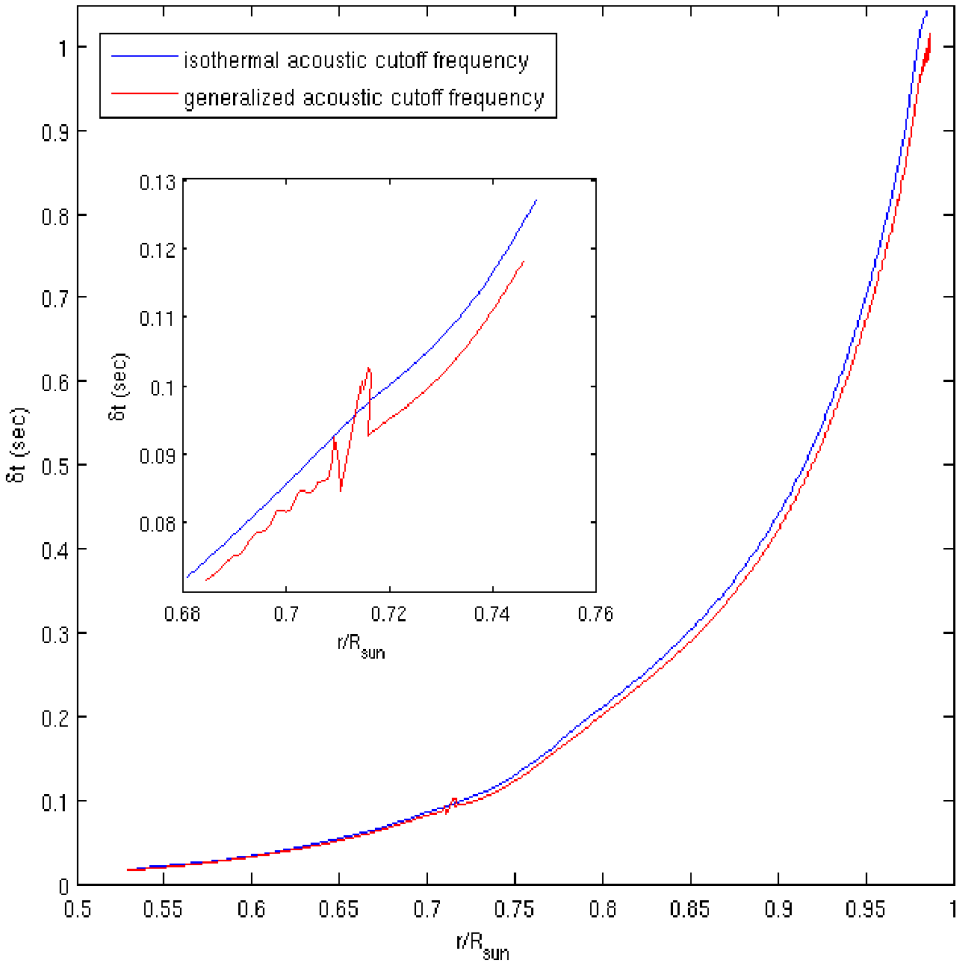

Figure 3.7: Ray-theoretic meridional travel-time shift (δt), in seconds, as a function of focal depth ($r/R_{\rm sun}$) for single-cell R06 flow model (max. flow speed = 13.5 m/s) at 45°S latitude, computed with the common-midpoint geometry. Ray paths are computed using the background Model S for different definitions of the acoustic cut-off frequencies: isothermal acoustic cut-off frequency ($\omega_{\rm ac} = c/2H_p$; blue curve), and generalized acoustic cut-off frequency ($\omega_{\rm ac} = c/2H\sqrt{1 - 2{\rm d}H/{\rm d}r}$; red curve). The bump in the red curve (see inset) is due to a subtle change in ${\rm d}\rho/{\rm d}r$ at the base of the convection zone in Model S affecting the ${\rm d}H/{\rm d}r \propto ({\rm d}^2\rho/{\rm d}r^2)\rho - 3({\rm d}\rho/{\rm d}r)^{-2}$ term in $\omega_{\rm ac}$.

3.2.4 Convective Stability

As discussed in Section 3.1, the different simulation codes have different approaches to ensuring convective stability. Both implementations use Model S as the background solar model for the most part. But whereas HLD06 modifies Model S in the outer convective layers above $0.98R_\odot$, HZK13 sets the Brunt-Väisälä frequency to zero, thus making the linearized Euler equations convectively stable. To make an effective comparison between ray-theoretic travel-time shifts of the flow models and time-distance measurement of travel-time shifts of the HLD06 and HZK13 simulations,

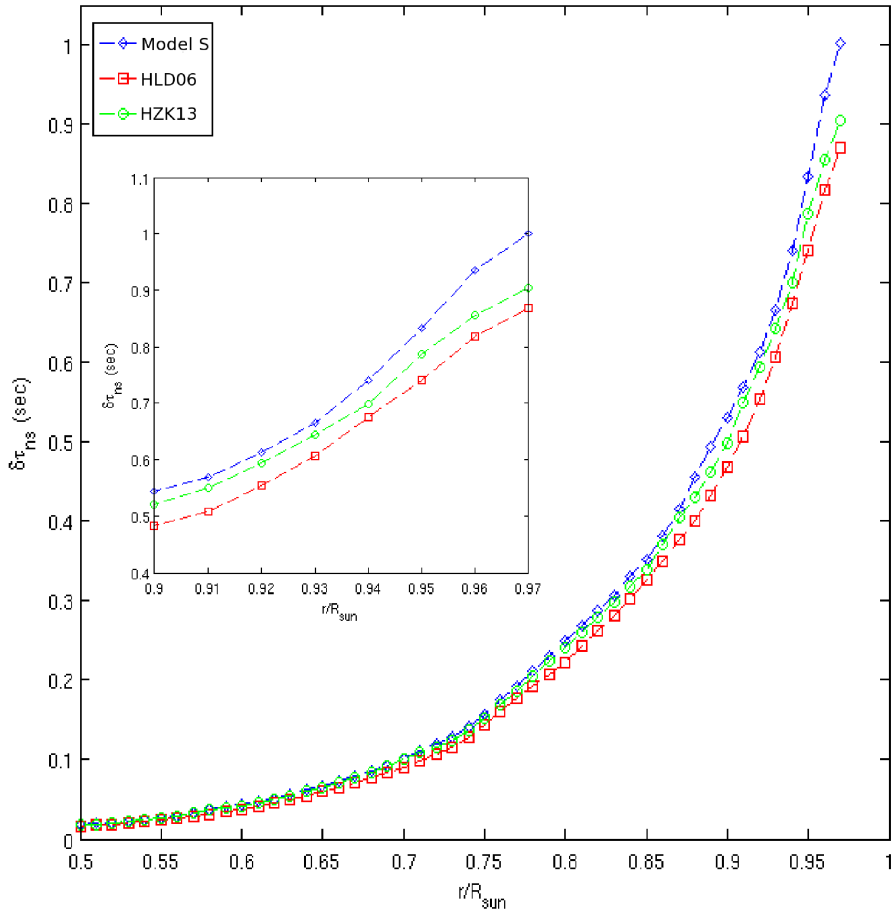

Figure 3.8: Ray-theoretic meridional travel-time shift ($\delta\tau_{\rm ns}$) as a function of focal depth ($r/R_{\rm sun}$) for single-cell R06 flow (max. flow speed = 13.5 m/s) at 45°S latitude, computed with the common-midpoint geometry. Ray paths are computed using the isothermal acoustic cut-off frequency for different cases: Model S (blue diamond); HLD06 (red square) where Model S is modified in the outer convective layers (above $0.98R_\odot$); HZK13 (green circle) where the Brunt-Väisälä frequency is set to zero in the dispersion equation used to calculate the ray paths. Inset expands the near-surface region.

these modifications need to be incorporated into the computation of ray paths.

The relevance of the Brunt-Väisälä frequency (N) can be seen in Equation (3.6) which is the local dispersion relation determining the ray paths. The impact on the meridional travel-time shifts due to the modification of the background solar model in the case of HLD06, and of the dispersion relation in the case of HZK13 are shown and compared to the regular case ($N \neq 0$) with Model S as the background model, for the single-cell R06 meridional flow and the double-cell JB07 meridional flow, in Figures 3.8 and 3.9 respectively. The ray paths are computed using the isothermal cut-off frequency and the travel-time shifts are computed with the common-midpoint geometry.

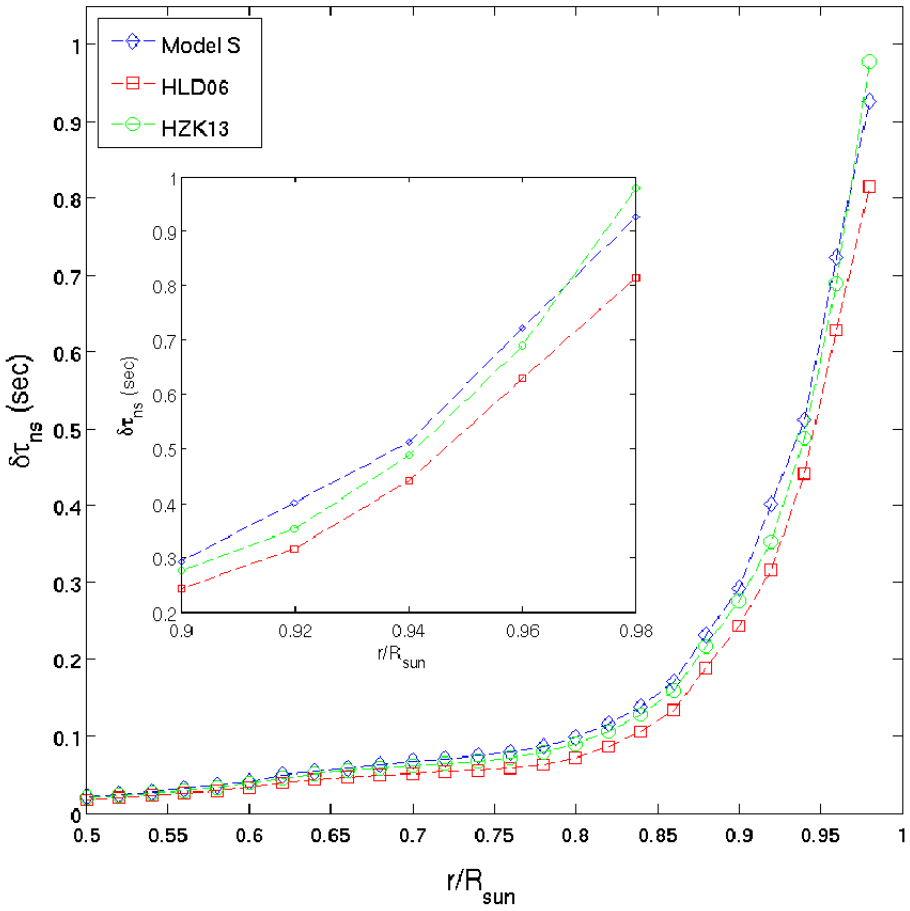

Figure 3.9: Ray-theoretic meridional travel-time shift ($\delta\tau_{\rm ns}$) as a function of focal depth for double-cell JB07 flow model (max. flow speed = 13.5 m/s) at 45°S latitude, computed with the common-midpoint geometry. Ray paths are computed using the isothermal acoustic cut-off frequency for: Model S (blue diamond); HLD06 (red square) ; HZK13 (green circle). Inset expands the near-surface region.

3.2.5 Discussion

The ray-theoretic north-south travel-time shifts for the different meridional flow models (Figure 3.5) show certain distinctive features in relation to flow velocity gradients and stagnation depths. The higher flow gradient of single-cell BC88 flow model compared to the single-cell R06 flow model results in a lower travel-time shift in the former in the bulk of the convection zone, even though the maximum flow velocity at the surface is the same for both models. This makes sense in the light of Equation (3.1), since the flow velocity is integrated along the ray path, and the smaller velocities make smaller contributions to the net travel-time shift. The meridional travel-time shift due to the double-cell JB07 flow model exhibits a sharper decline than both the single-cell models due to the shallower stagnation point. However, the near-surface travel-time shift is in between the single-cell travel-time shifts, since the JB07 flow model has a near-surface flow velocity gradient that is also in between those of both the single-cell models. In this connection Figure 3.10 represents work done by the author in the early stages of his research work, where the depth of the single-cell

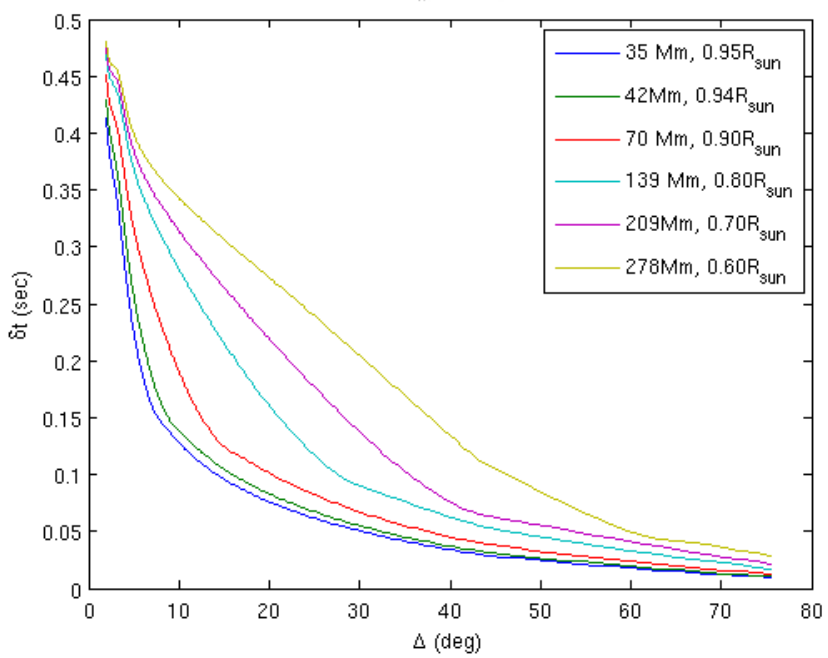

Figure 3.10: Ray-theoretic meridional travel-time shift (δt) at 45°S latitude as a function of skip distance (Δ), computed with common-midpoint geometry for various total depths (indicated in the legend), or alternatively stagnation depths, of the single-cell BC88 meridional flow model. Ray paths are computed using the isothermal acoustic cut-off frequency and background Model S.

BC88 flow model is varied to examine the corresponding change in the travel-time shift. The travel-time shifts are plotted as a function of skip distance (Δ) which has a nearly linear relationship with the focal depth ($\approx \Delta/\pi$, measured from the surface; cf. Giles et al., 1997, also discussed in Section 2.2.2) of a single-skip ray path in the bulk of the convection zone. Thus the skip distance may be used as a proxy for focal depth in the convection zone, the smaller skip-distances denoting smaller depths, etc. Evidently, the shallower the stagnation depth, the steeper the decline in the meridional travel-time shift. This is, potentially, an important diagnostic for determining the structure of meridional flow.

Figure 3.6 shows a steady decrease in the travel-time shift values with the inclusion of more rays intersecting the focal depth (which amounts to the same thing as including more pairs of arcs). This is due to the fact that the larger ray paths experience smaller travel-time shifts, and the net travel-time shift for the full deep-focus geometry is calculated by averaging the travel-time shifts for all the ray paths constituting the deep-focus geometry. This causes the mean travel-time shift to reduce in value for a particular focal depth as longer ray paths intersecting the focal depth are included.

Figure 3.7 suggests that substituting the generalized acoustic cut-off frequency for the isothermal acoustic cut-off makes a significant difference only at the surface and the base of the convection zone, since these are the locations where these quantities significantly differ from each other. For the bulk of the convection zone, it makes little difference to the computation of ray paths. In fact, Jefferies et al. (1994) suggested that due to the derivatives present in Equation (3.2), the generalized cut-off frequency exhibits rapid variation near the surface, and since the JWKB approximation necessary for ray theory loses validity where the underlying equilibrium state varies rapidly in depth, a simpler expression for the acoustic cut-off frequency is the preferred option for calculating acoustic travel times. It was, however, brought to the author's attention independently by A. G. Kosovichev and K. V. Parchevsky (private communication) that the expression for the cut-off frequency derived from the HZK13 linearized Euler equations is different from the conventional ones—this is the mathematical reason behind the lower acoustic cut-off frequency mentioned in Section 3.1 and visible in Figure 3.1. It is unknown how the inclusion of the HZK13 cut-off frequency will alter the ray-theoretic results.

The generalized cut-off frequency also exhibits strange behavior near the base of

the convection zone due to the presence of an inflection point in the density gradient there in solar Model S, which causes $\mathrm{d}^2\rho/\mathrm{d}r^2$ included in the expression for the generalized cut-off frequency to exhibit a bump, thus affecting the ray paths and the associated travel-time shifts in funny ways as displayed in the inset in Figure 3.7.

Finally, incorporating the HLD06 and HZK13 convective stability modifications into the ray-theoretic computations result in non-negligible changes (compared to the discrepancies and error bars in Figures 3.15–3.17) in the convection zone (cf. Figures 3.8 and 3.9). The Model S and HZK13 results are very similar. Care must especially be taken when dealing with predominantly surface phenomena, e.g., possibly supergranulation. Figure 3.11[1] shows the remarkable agreement achieved between HLD06 simulation and ray-theory due to the incorporation of the HLD06 convectively stable

[1]Figure 3.11 is reprinted with kind permission from Springer Science and Business Media: Solar Physics, Duvall and Hanasoge (2013), and Duvall et al. (2014).

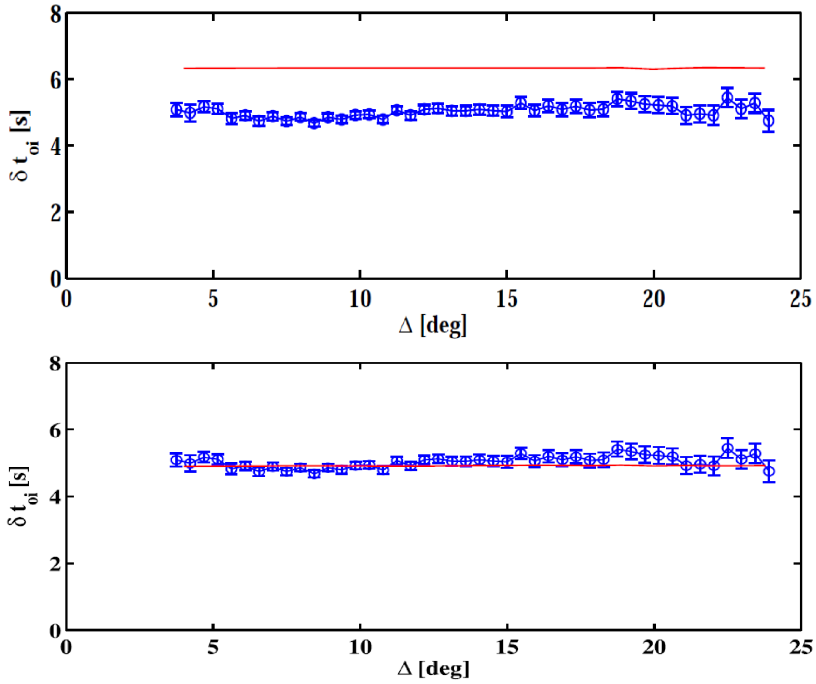

Figure 3.11: Comparison of center-annulus travel-time shifts (δt_{oi}) computed from the HLD06 simulation with embedded flow perturbations (blue circles) with ray-theoretic travel-time shifts with the same flow perturbations (red line). The flow perturbation consists of Gaussian features with vertical flow (peak flow = 6.3 m/s) centered at a depth of $z_0 = 2.30$ Mm with $\sigma_z = 0.82$ Mm and with horizontal $\sigma_{\mathrm{h}} = 5.1$ Mm. 500 of these features are placed at random locations at depth z_0. Top (Duvall and Hanasoge, 2013): Ray theory with background solar model, Model S; Bottom (Duvall et al., 2014): Ray theory with convectively stable background model HLD06.

background model in the ray-theoretic computations (cf. Duvall and Hanasoge, 2013; Duvall et al., 2014). This was made possible due to the extension of the existing ray-path generation code by the author, to include the HLD06 convectively stable background model. The embedded flow perturbation in this case was 500 randomly located Gaussian features with vertical flow centered at a depth of $z_0 = 2.30$ Mm with $\sigma_z = 0.82$ Mm and with horizontal $\sigma_{\rm h} = 5.1$ Mm, all of them located at a depth of $z_0 = 2.30$ Mm. In this case the modification of the background solar model mattered for the ray-theoretic computations because the phenomena of interest lay in the region where the stability modifications were made (above $0.98R_\odot$).

3.3 Time-Distance Analysis and Results

The meridional flow models (R06, BC88, JB07) discussed in Section 3.2.1 are interpolated to the HLD06 and HZK13 simulator grids and then incorporated into the respective simulators as the background flow (no rotation or zonal flow was included). To improve the signal-to-noise ratio of the travel-time shift measurements, and to reduce the simulation run time, T. L. Duvall, Jr. (private communication) suggested that the meridional flow speed amplitude should be amplified while staying within the linear regime of low Mach number, i.e., $v_\theta/c \ll 1$. Following his suggestion, the maximum (surface) flow speed of all the models embedded into the simulators is amplified to 500 m/s. Due to the linear relationship between the travel-time shift and the flow velocity (cf. Equation (3.1)), the computed travel-time shifts can be simply scaled down to represent more realistic meridional flow speeds.

The resulting simulation data extends over all longitudes and latitudes on 768×384 and 512×256 grid points for the HLD06 and HZK13 case, respectively. The datacubes obtained are images of radial velocity (approximating line-of-sight projection of oscillatory motion) of various temporal extent, ranging from 9–20 hours, depending on simulation run time. These simulation datacubes are phase-speed filtered as described in Section 2.2.1. Subsequently, the datacubes are analyzed with the deep-focus time-distance technique to obtain north-south or meridional travel-time shifts which, after being scaled down to reflect a more realistic flow speed amplitude of 13.5 m/s, are compared with ray-theoretic travel-time shifts due to meridional flow with the same amplitude. In the following sections, various deep-focus geometries are investigated and different meridional flow models are analyzed, in an effort to

formulate a robust forward modeling procedure and to determine the efficacy of ray theory as a model for interpreting travel-time shifts computed by the time-distance technique. All the basic time-distance subroutines used in this part of the analysis were developed by T. L. Duvall, Jr. The author's original contribution lay in combining and applying these subroutines to make the first full deep-focus time-distance measurements of meridional flow induced travel-time shifts on phase-speed filtered simulated (and solar; cf. Chapter 4) velocity data, at depth ranges equivalent to the solar convection zone.

3.3.1 Common-Midpoint vs. Full Deep-Focus Technique

Various deep-focus time-distance techniques (common-midpoint, 5-pairs, 9-pairs) are applied on 19 hours of phase-speed filtered (cf. Section 2.2.1) HZK13 simulation data with embedded single-cell R06 meridional flow. For all latitude-longitude map-points (except the ones near the perimeter of the image made inaccessible due to the spatial extent of the deep-focus geometry), temporal cross-covariances are calculated 175 minutes forward and backward in time lag, for diametrically opposite pixels of the appropriate arcs within the north-south quadrants as described in Section 2.2.3. Then the cross-covariances are averaged over the quadrant and over the pairs of arcs, also as discussed in Section 2.2.3.

In order to obtain error bars the datacube is divided into five equal longitudinal strips of 72° in width. The cross-covariances are averaged over each of the longitudinal strips and then fit with the Gabor-wavelet function (Section 2.2.4) given by

$$G_{\pm}(\tau) = A\cos[\omega_0(\tau - \tau_{\pm})]\exp\left[-\frac{\delta\omega^2}{4}(\tau - \tau_{\rm g})^2\right], \tag{3.8}$$

to obtain the phase travel time where the cross-covariance function peaks, in both the positive and negative time-lag branches ($\tau_{\pm}$) . The difference between the travel times ($\delta\tau_{\rm ns} = \tau_{+} - \tau_{-}$) so obtained is the north-south travel-time shift (distinct from and yet equated to the ray-theoretic north-south travel-time shift) due to meridional flow. The travel-time shifts obtained from each longitudinal strip are then combined to obtain the mean north-south travel-time shift and the standard error of the mean. No further averaging is done over depth or latitude. The resulting meridional travel-time shifts as a function of latitude and the associated error bars for the common-midpoint, 5-pairs, and 9-pairs geometry are shown in Figures 3.12, 3.13 and 3.14 respectively.

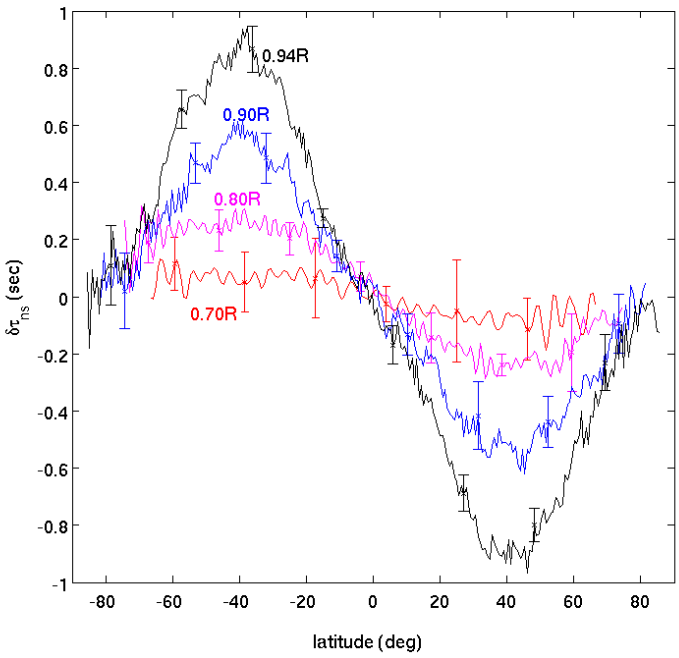

Figure 3.12: Meridional travel-time shift ($\delta\tau_{\rm ns}$) (scaled down to reflect max. flow speed of 13.5 m/s), as a function of latitude at various focal depths: $0.94R$ (black), $0.90R$ (blue), $0.80R$ (magenta), $0.70R$ (red), where $R = R_\odot = R_{\rm sun}$. Common-midpoint technique is applied on 19 hours of phase-speed filtered HZK13 simulation data with embedded single-cell R06 flow model. Error bars show excursions of twice the standard error of the mean.

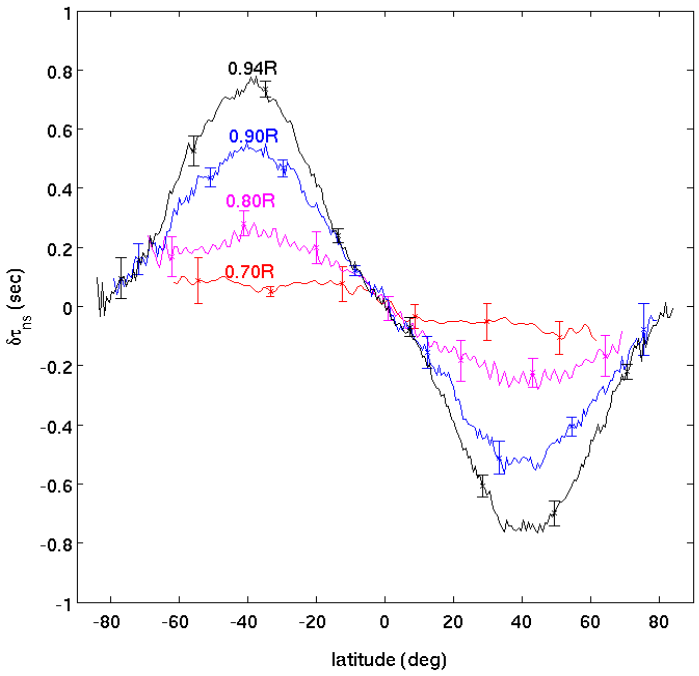

Figure 3.13: Same as in Figure 3.12 except 5-pairs deep-focus technique is applied.

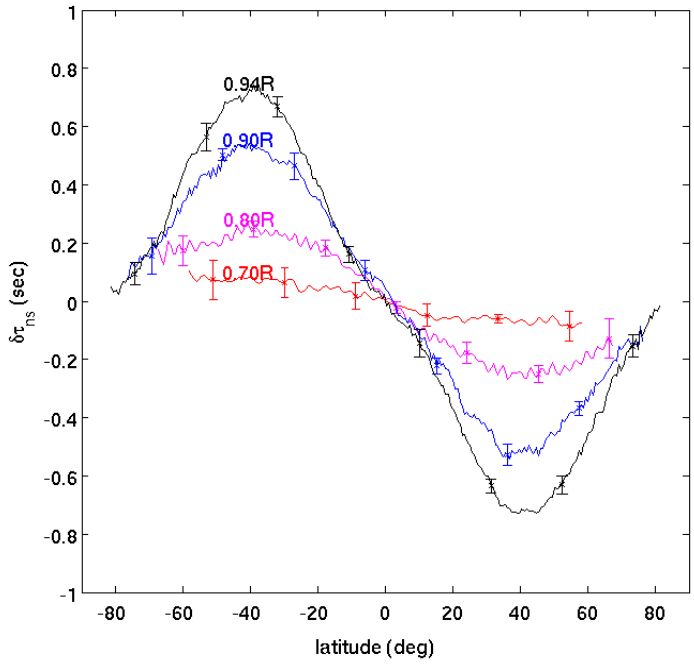

Figure 3.14: Same as in Figure 3.12 except 9-pairs deep-focus technique is applied.

3.3.2 Meridional Travel-Time Shifts

The three flows models (R06, BC88, JB07) are embedded in the HLD06 and HZK13 simulators (the HZK13 simulator was not available for the BC88 flow model) to produce datacubes of various durations depending on simulation run time (HLD06/R06: 9 hours; HZK13/R06: 19 hours; HLD06/BC88: 15 hours; HLD06/JB07: 16 hours; HZK13/JB07: 20 hours). The datacubes are time-distance analyzed (cf. Section 3.3.1). Realization noise due to source excitations is removed (except for HZK13/R06 simulation) by simulating without flow perturbation, but with the same source excitations, and then subtracting the resultant north-south travel-time shifts to obtain noise-corrected results (Hanasoge et al., 2007). Time-distance analysis to obtain travel-time shifts from the "quiet" simulations is carried out for exactly the same time intervals as their flow-embedded counterparts and following the exact same procedure. Since the simulations are slightly asymmetric in the northern and southern hemispheres, the travel-time shifts for each latitude in the northern and southern hemispheres are averaged. The north and south averaged travel-time shift is plotted as a function of focal depth at select latitudes in Figures 3.15 (HLD06+HZK13/R06), 3.16 (HLD06/BC88) and 3.17 (HLD06+HZK13/JB07), along with the ray-theoretic (Model S, convectively stable HZK13 and HLD06) travel-time shift.

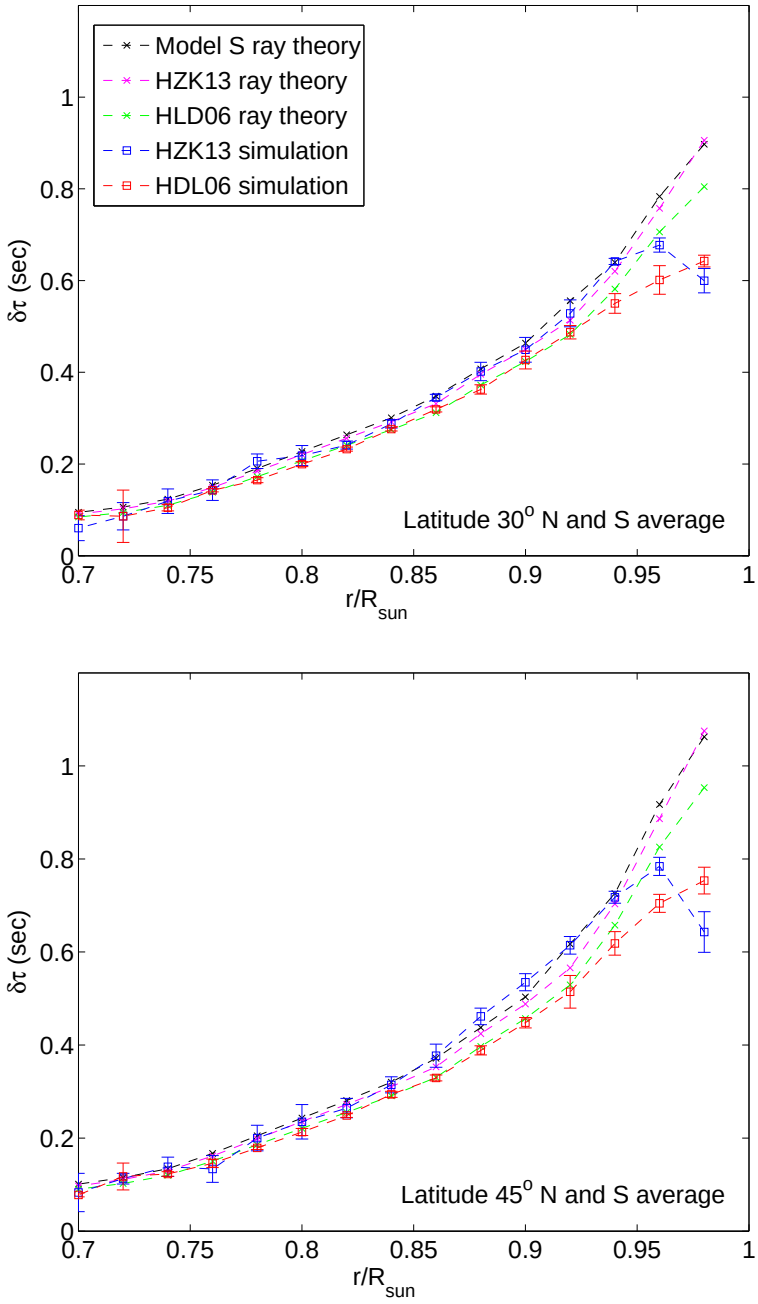

Figure 3.15: Meridional travel-time shift ($\delta\tau$), in seconds (scaled down to reflect max. flow speed of 13.5 m/s), as a function of focal depth ($r/R_{\rm sun}$), calculated using 5-pairs deep-focus geometry at 30° (top panel) and 45° (bottom panel) latitudes (N and S averaged) for the single-cell R06 meridional flow model. Each panel shows time-distance results for HLD06 (red squares), HZK13 (blue squares) simulation data, and ray-theoretic travel-time shifts (Model S: black; HZK13: magenta; HLD06: green crosses). Realization noise is subtracted from HLD06 simulation only. Error bars show excursions of twice the standard error of the mean.

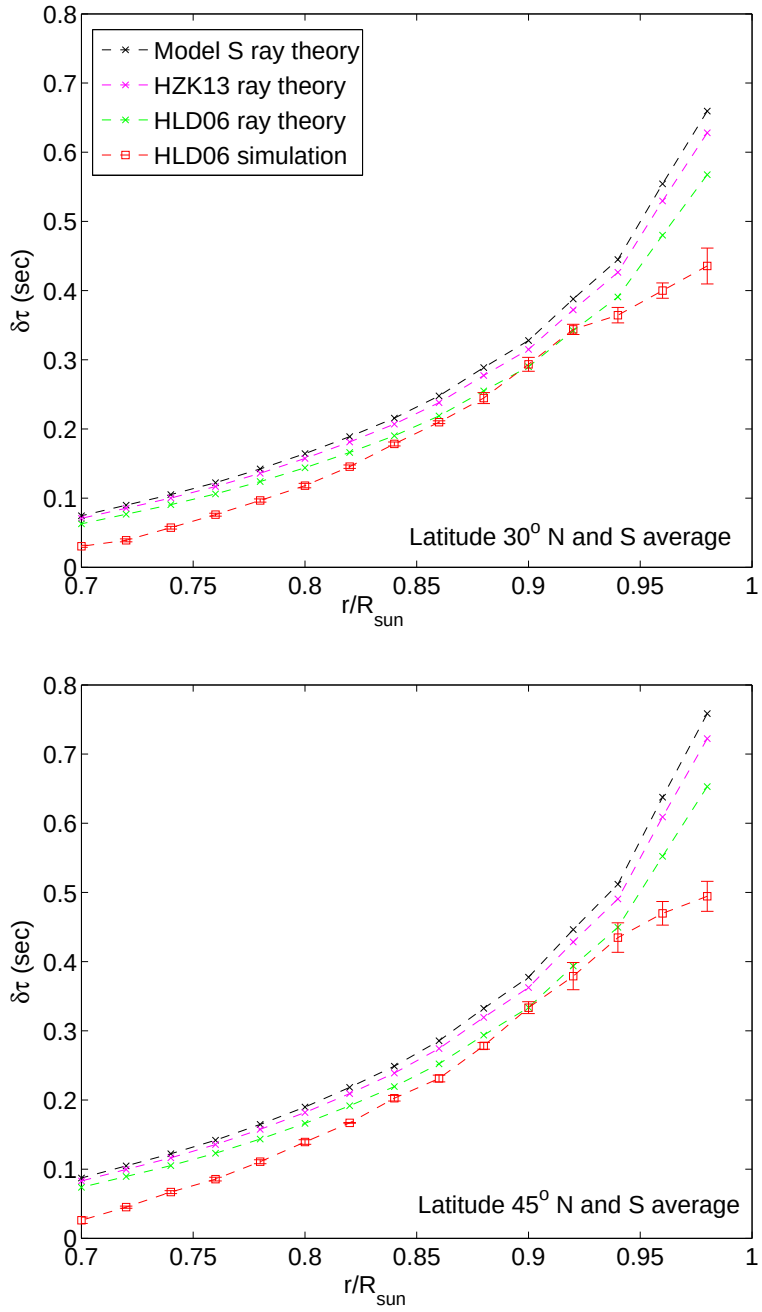

Figure 3.16: Meridional travel-time shift ($\delta\tau$), in seconds (scaled down to reflect max. flow speed of 13.5 m/s), as a function of focal depth ($r/R_{\rm sun}$), calculated using 5-pairs deep-focus geometry at 30° (top panel) and 45° (bottom panel) latitudes (N and S averaged) for the single-cell BC88 meridional flow model. Each panel shows time-distance results for HLD06 simulation data (red squares) and ray-theoretic travel-time shifts (Model S: black; HZK13: magenta; HLD06: green crosses). Realization noise is subtracted from HLD06 simulation data. HZK13 simulator was not available for this case. Error bars show excursions of twice the standard error of the mean.

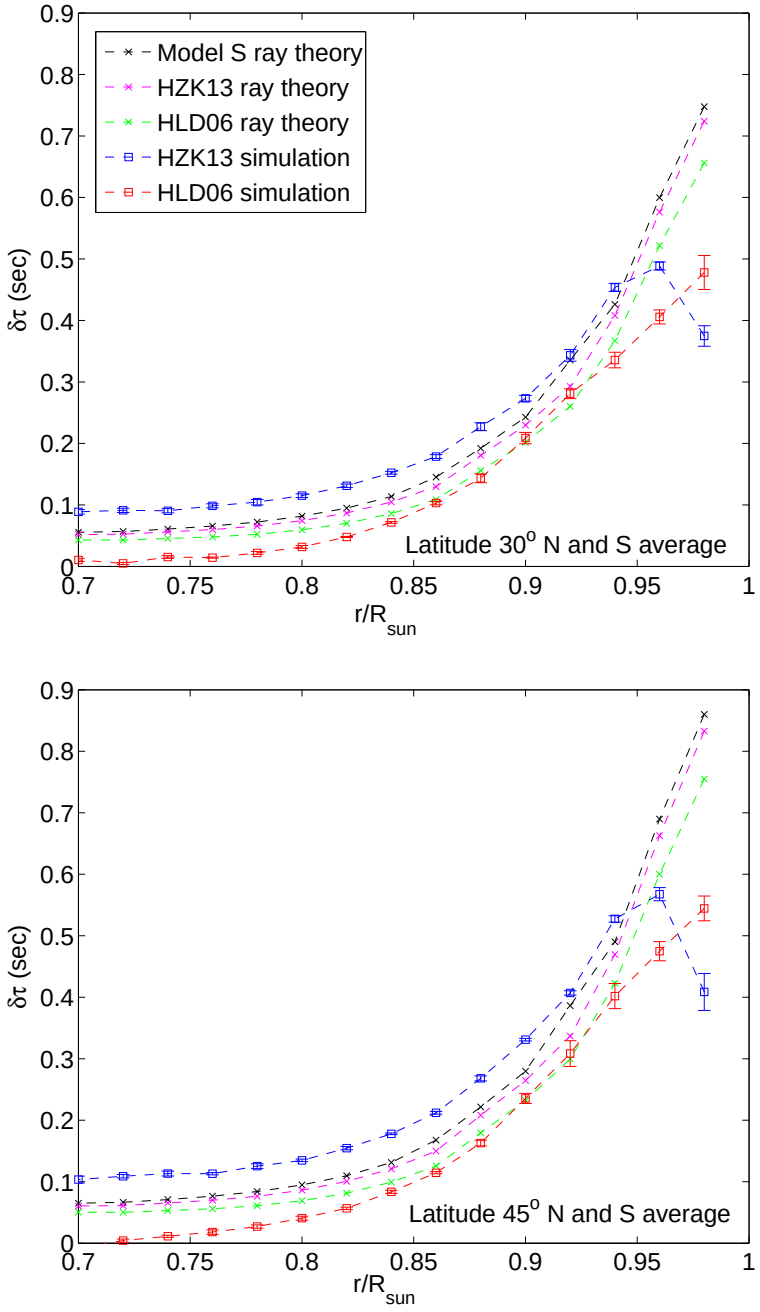

Figure 3.17: Meridional travel-time shift ($\delta\tau$), in seconds (scaled down to reflect max. flow speed of 13.5 m/s), as a function of focal depth ($r/R_{\rm sun}$), calculated using 5-pairs deep-focus geometry at 30° (top panel) and 45° (bottom panel) latitudes (N and S averaged) for the double-cell JB07 meridional flow model. Each panel shows time-distance results for HLD06 (red squares), HZK13 (blue squares) simulation data, and ray-theoretic travel-time shifts (Model S: black; HZK13: magenta; HLD06: green crosses). Realization noise is subtracted from simulation data. Error bars show excursions of twice the standard error of the mean.

3.3.3 Discussion

Time-distance computations with different deep-focus techniques (cf. Figures 3.12–3.14) indicate that including more pairs of arcs in the computations result in a cleaner travel-time shift signal at all focal depths. However, the cleaner signal comes at the expense of greater computation time, and also loss of information at higher latitudes due to the utilization of more of the image space to calculate the cross-covariance function. So a trade-off must be made between improved signal-to-noise ratio on the one hand, and both computational expense and loss of information on the other. In the case considered in this work, while 5-pairs deep-focus technique considerably improves the signal compared to the common-midpoint deep-focus case, 9-pairs deep-focus technique does not improve upon the result of the 5-pairs deep-focus case enough to warrant the higher computational expense and the loss of information at the higher latitudes.

The relatively low value of the north-south travel-time shift of the HZK13 simulation at $0.98R_\odot$ in Figures 3.15 and 3.17 is due to the lower resolution of the HZK13 simulation grid ($0.703125^\circ \times 0.703125^\circ$, as opposed to $0.46875^\circ \times 0.48675^\circ$ for the HLD06 simulator), and therefore unreliable. Other than that, the results shown in Figures 3.15–3.17 are not very well understood, especially in the unfortunate absence of HZK13 simulation data with single-cell BC88 meridional flow. While there is qualitative agreement between ray theory, the HLD06 simulation and the HZK13 simulation, quantitative agreement varies with the meridional flow model.

The applicability of ray theory to time-distance helioseismology has been called into question where the spatial variation of the perturbation is comparable to the acoustic wavelength (Bogdan, 1997), and this is certainly the case for the meridional flow models under consideration, in certain parts of the convection zone. Why then is there such remarkable agreement in Figure 3.15 between the ray-theoretic travel-time shifts and the time-distance computation of travel-time shifts from HLD06 and HZK13 simulation data in the deep convection zone? What is special about the R06 meridional flow model? Could this be a fluke? A comparison of the flow velocity scale heights (e.g., $-(\partial \ln v_\theta/\partial r)^{-1}$) with the acoustic wavelength did not reveal anything distinctive about any of the meridional flow models. Given the result in Figure 3.15, it is baffling as to why there is such substantial disagreement for the double-cell JB07 meridional flow model (Figure 3.17), between the HZK13 and HLD06 simulations and ray theory. One possible reason is the greater complexity of the double-cell

meridional flow. There may be issues such as ray theory not being sensitive to the increased vorticity present in the more complex meridional flows. However, without the HZK13 simulation with the single-cell BC88 meridional flow it is not possible to argue either for or against that reason. Also, this is certainly not the case with the HLD06 simulation as reflected in Figures 3.16 and 3.17 which shows roughly the same deviation from ray theory. Another possibility is that the different approaches to convective stability resulting in very different power spectra for the two simulations, give rise to quantitative differences in the perturbations to the acoustic modes and wavefields due to the meridional flow. This avenue is worth exploring in some detail. Some preliminary work on frequency filtering the power spectra of the simulation data did not yield any useful insights as either the travel-time shifts remain unchanged, or become too noisy due to insufficient power in the modes.

At this point the author concludes that without an in-depth analysis of the differential equations involved in the modeling and comparing them term by term, and that without an examination of the computational aspects of each of the simulators, a firm conclusion is unattainable. These theoretical and computational pursuits, though undoubtedly stimulating, are beyond the scope of this dissertation. Thus, without a robust forward model the reliability of time-distance helioseismic measurements of meridional flow in the deep convection zone cannot be adequately established. A weak case may, however, be made that if the uncertainties in the solar measurements exceed the discrepancies (≈ 100 ms), for all practical purposes, the discrepancies may be considered academic. Nevertheless, it is encouraging to see in Figures 3.15–3.17 that the different convective stabilization procedures adopted in ray theory produce results that are in closer agreement (albeit slight) with the respective convectively stable simulation data. Perhaps the inclusion of the appropriate acoustic cut-off frequencies in ray theory as discussed in Section 3.2.5 will yield more consistent results, at least between ray theory and time-distance analysis of simulations.

Chapter 4

Computing Travel Times with HMI Data

In order to achieve the goal of determining the structure of meridional circulation in the solar convection zone, the techniques developed and discussed in this dissertation thus far, need to move beyond simplistic toy problems to real-life scenarios, i.e., solar data. Solar data or images, unlike simulated data discussed in Chapter 3, are not created with equations implemented in numerical algorithms. Instead, real image-data are acquired by sophisticated instruments on ground or in space, and then subjected to a chain of processing algorithms (the data pipeline) that convert the raw images into usable data products that are analyzable by specific methods, in this case, time-distance helioseismology. The data product depends on the needs of the end user who may obtain it at various stages of the data pipeline. For instance, in this work the author uses the time series of spherical harmonic coefficients obtained from the spherical harmonic decomposition algorithm of the HMI global helioseismology pipeline (cf. Sections 4.1–4.2; also Larson and Schou, 2011).

The techniques developed and the forward models validated while addressing toy problems are intended for application to the results of time-distance analysis of solar velocity data; to derive sensitivity kernels which can be used in inverse problems to infer the physical quantities of interest (e.g., meridional flow velocity). However, there are systematic errors (e.g., the "center-to-limb" effect) that need to be taken into account in the modeling for accurate interpretation and inversion of the time-distance measurements or travel times. In this dissertation the author stops short

of inverting the travel times, and instead focuses on characterizing the "center-to-limb" effect (Zhao et al., 2012, 2013) which has hampered adequate interpretation of travel times obtained from solar images. Section 4.3 outlines a method to confirm or disconfirm the interpretation of the "center-to-limb" effect put forward by Baldner and Schou (2012).

4.1 Helioseismic and Magnetic Imager

A detailed treatment of the Helioseismic and Magnetic Imager (HMI) instrument and investigation may be obtained from Scherrer et al. (2012), Schou et al. (2012) and the references therein. A brief introduction and overview is provided for completeness' sake, since the Dopplergrams provided by the HMI instrument are the author's primary means of investigating travel times due to meridional flow in the solar convection zone, with possible contamination by systematic errors, such as the finite light travel time effect (Duvall and Hanasoge, 2009), and the more recently published "center-to-limb" effect, and other yet undiscovered anomalies. In Section 4.3 the author uses longitude-latitude velocity images that are partial (up to spherical harmonic degree of $l = 300$) spherical harmonic reconstructions of remapped HMI Dopplergrams, to examine the logical and physical consequences of a "true" center-to-limb effect.

4.1.1 Introduction

The Helioseismic and Magnetic Imager (HMI) investigation (Scherrer et al., 2012; Schou et al., 2012) is part of the 5-year NASA Solar Dynamics Observatory (SDO) mission—the first space-based mission of the NASA Living With a Star (LWS) program. The HMI investigation is jointly conducted by the W. W. Hansen Experimental Physics Laboratory (HEPL) at Stanford University, the Lockheed Martin Solar and Astrophysics Laboratory (LMSAL), the High Altitude Observatory (HAO), and others. The HMI instrument was developed and built by LMSAL in collaboration with Stanford University as part of the Stanford Lockheed Institute for Space Research (SLSIR). It is one of the instruments aboard the SDO spacecraft that was launched on February 11, 2010 and placed in geosynchronous orbit at an altitude of 36,000 km.

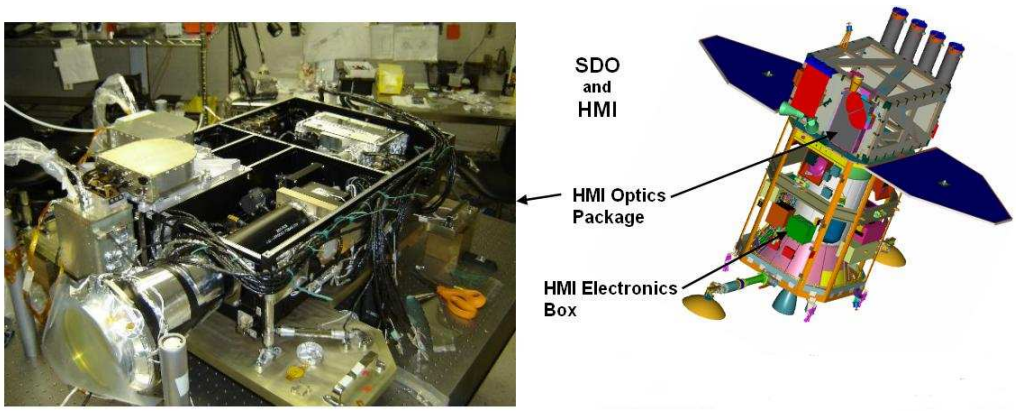

Figure 4.1: Left: HMI Optics Package; Right: Cartoon of SDO spacecraft with the HMI instrument. Courtesy: SDO/HMI Team.

The objective of SDO is to make advances in our ability to understand and predict solar events that influence the near-terrestrial space environment. The cyclic emergence and evolution of active magnetic regions on the solar photosphere drive the solar variability that induces phenomena significant for the terrestrial space environment. According to the abstract in Scherrer et al. (2012) the HMI instrument "is designed to study convection-zone dynamics and the solar dynamo, the origin and evolution of sunspots, active regions, and complexes of activity, the sources and drivers of solar magnetic activity and disturbances, links between the internal processes and dynamics of the corona and heliosphere, and precursors of solar disturbances for space-weather forecasts." As part of investigating the convection-zone dynamics and the solar dynamo, Scherrer et al. (2012) emphasized that

> Precise knowledge of meridional circulation in the convection zone is crucial for understanding the long-term variability of the Sun...To understand the global dynamics we must follow the evolution of the flow. HMI will enable the measurement of the meridional circulation to significantly higher latitudes...and will generate continuous data for detailed, 3D maps of the evolving patterns of meridional circulation providing information about how flows transport and interact with magnetic fields throughout the solar cycle.

Scherrer et al. (2012) also wrote:

> To support these objectives...[t]he HMI instrument makes measurements [in the Fe I absorption line centered at wavelength 6173 Å] of the motion of the solar photosphere to study solar oscillations and measurements of the polarization in a spectral line to study all components of the photospheric magnetic field. The HMI instrument is an enhanced version of the

Michelson Doppler Imager (MDI) instrument which is part of the Solar and Heliospheric Observatory (SOHO: Scherrer et al., 1995). HMI has significant heritage from MDI with modifications to allow higher resolution, higher cadence, and the addition of a second camera to provide additional polarization measurements without interfering with the filtergram cadence needed for helioseismology.

4.1.2 HMI Instrument[1]

As described in Schou et al. (2012) "[t]he [HMI] instrument consists of a front-window filter, a telescope, a set of waveplates for polarimetry, an image-stabilization system, a blocking filter, a five-stage Lyot filter with one tunable element, two wide-field tunable Michelson interferometers, a pair of 4096^2 pixel cameras with independent shutters, and associated electronics. Each camera takes a full-disk image roughly every 3.75 seconds" which according to Scherrer et al. (2012) allows HMI to provide "stabilized one-arcsecond resolution full-disk Doppler velocity, line-of-sight magnetic flux, and continuum proxy images every 45 seconds...The solar image nearly fills the 4096×4096 pixel CCD camera allowing 0.5 arcsecond per pixel."

The HMI Optics Package (cf. Figures 4.1 and 4.2) in brief (Schou et al., 2012): The front window is a 50 Å FWHM bandpass filter, the main purpose of which is to limit the heat input to the instrument. The main telescope is a two-element refracting telescope with a 140 mm clear aperture, giving an image with a nominal diffraction limit (λ/D) of 0.91 arcsecond. For the purpose of polarimetry, the polarization selectors rotate two of the three available quartz waveplates to convert the desired incoming polarization into a fixed linear polarization. The HMI image-stabilization system is a closed-loop system with a tip-tilt mirror to remove jitter measured at a primary image within HMI. The blocking filter is a three-period, all-dielectric, interference filter with a FWHM bandpass of 8 Å; its purpose is to reject the unwanted orders of the Lyot and Michelson filters, and to limit the heat input. The wide-field, temperature-compensated Lyot filter adds a fifth tuned element to the four-element MDI design (Scherrer et al., 1995) in order to accommodate the wide range in radial velocity due to the geosynchronous orbit of SDO. The two wide-field, tunable, solid Michelson interferometers have clear apertures of 32 mm, and 172 mÅ and 86

[1]Figures 4.2 and 4.3 are reprinted with kind permission from Springer Science and Business Media: Solar Physics, Schou et al. (2012).

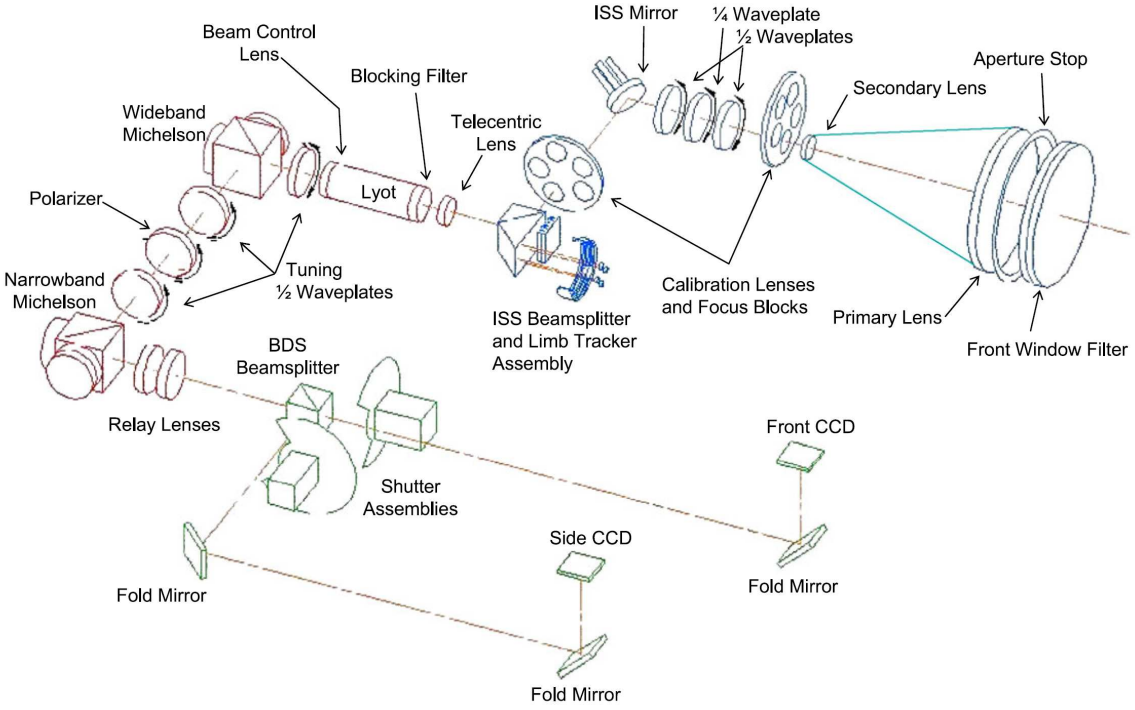

Figure 4.2: Schematic of the HMI optical layout with the various optical elements labeled, some of which are described in the text. Courtesy: Schou et al. (2012).

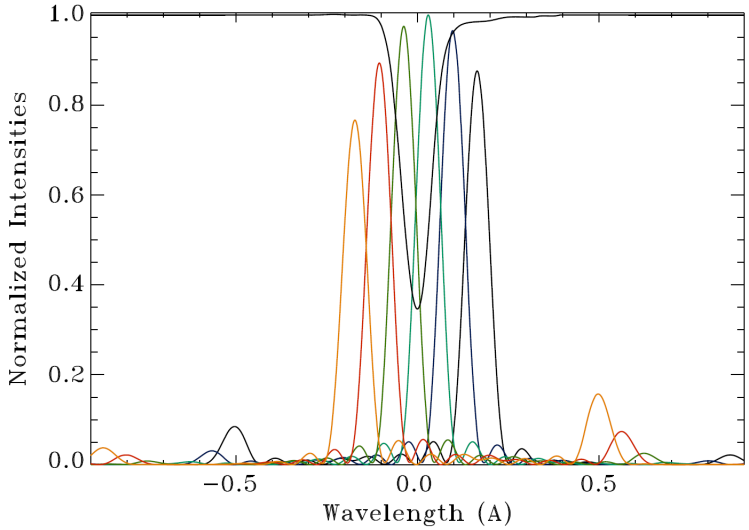

Figure 4.3: Six wavelength tuning positions are shown in different colors with respect to the Fe I solar absorption spectral line (black line) at disk center and at rest. Courtesy: Schou et al. (2012).

mÅ FWHM pass bands, respectively; tuning is accomplished by rotating a combination of a half-wave plate, a polarizer, and a half-wave plate. Thus, the HMI filter system consists of the front window, a blocking filter, a Lyot filter with a single tunable element, and two tunable Michelson interferometers. The filter system enables narrow-band filtergrams to be made across the Fe I 6173 Å spectral line (Figure 4.3) by the simultaneous tuning of the Lyot filter and the two Michelson interferometers. The filter system has a combined FWHM bandpass of 76 mÅ with a tunable range of 690 mÅ. HMI contains two identical CCD detectors, with a 4096^2 (12 μm) pixel format. During operation, a programmable number of CCD rows are first shifted rapidly to eliminate any accumulated charge, the shifting is halted while the shutter is opened, and the CCD is read out at a rate of 2 Mpixels/s.

A separate HMI Electronics Box (cf. Figure 4.1) contains the power supplies, control electronics, and data-processing electronics. The data from the CCDs are downlinked without any processing other than hardware compression and encoding carried out within the electronics box. All of the images are downlinked for processing at the Joint Science Operations Center (JSOC) at Stanford University.

4.1.3 HMI Data Products[2]

The basic science observables (cf. Figure 4.4) are full-disk Doppler velocity (Dopplergrams), Fe I line width, line depth, continuum intensity (intensitygrams), line-of-sight magnetic flux (magnetograms), and vector magnetic field (vector magnetograms). The line-of-sight observables (Couvidat et al., 2012) are available at full spatial resolution at 45-second cadence, and are computed on the ground using 12 filtergrams: images taken at 6 different wavelengths in the Fe I 6173 Å absorption line (Figure 4.3) and 2 polarizations (left-circular and right-circular polarizations). Images of observables sampled and averaged at various resolutions and cadences, sub-image samples tracked with solar rotation, time series of spherical harmonic coefficients, subsurface flow maps, farside activity maps, and other derived data products are produced in the processing pipeline (Figure 4.4), and made available on a regular basis or on request. The data product of interest for this work are the time series of spherical harmonic coefficients obtained by the spherical harmonic decomposition of Dopplergrams remapped onto a longitude-sin(latitude) grid.

[2]Figure 4.4 is reprinted with kind permission from Springer Science and Business Media: Solar Physics, Scherrer et al. (2012).

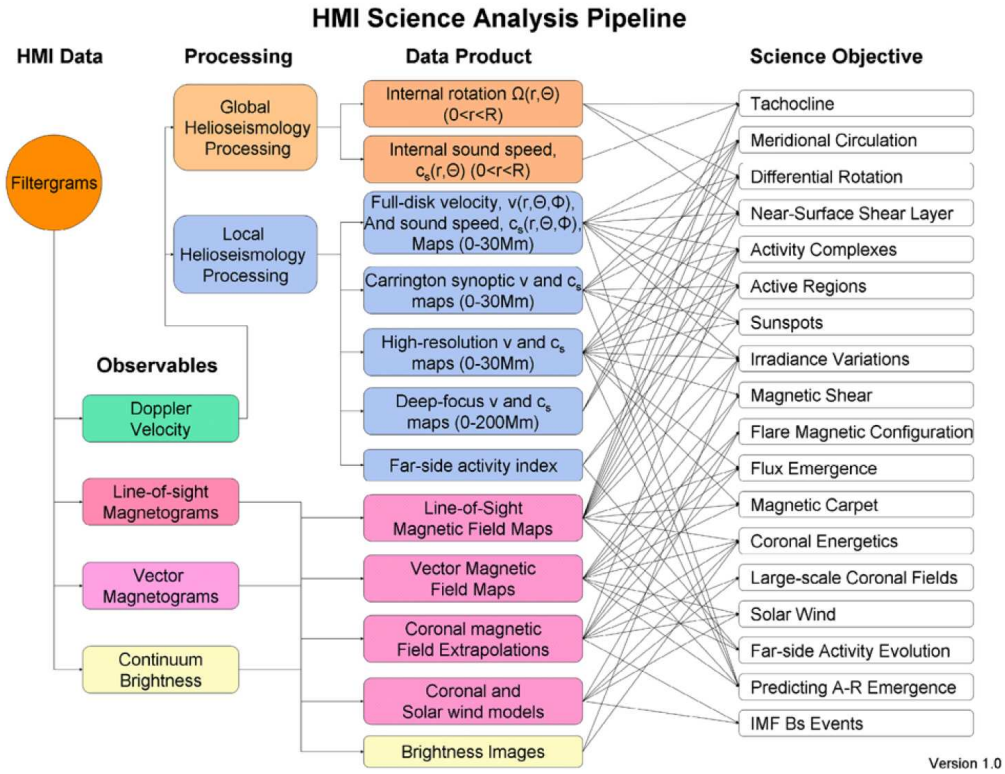

Figure 4.4: Schematic flow diagram for the HMI processing pipeline. The observables and other data products are calculated from the filtergrams and made available to the community. Derived higher-level data products such as full-disk velocity maps are to be used as data for science investigations. Courtesy: Scherrer et al. (2012).

4.2 Spherical Harmonic Reconstruction

4.2.1 Introduction

The time series of spherical harmonic coefficients mentioned in Section 4.1.3 are obtained as an intermediate data product of the HMI global helioseismology data analysis pipeline (cf. Figure 4.4) described in Larson and Schou (2011). The Carrington-inclination corrected Dopplergrams are first apodized in fractional solar radius and then remapped to a longitude-sin(latitude) grid. Subsequently, each image is decomposed into its spherical harmonic components of degree l and azimuthal order m. The fact that the entire surface of the Sun is not visible, and the consequent mode leakage and leakage matrices are of no relevance in this dissertation. Time series of the complex spherical harmonic coefficients are constructed which are retiled into 72-day chunks for each l and $-l \leq m \leq l$. Bad data points are identified and rejected: images which were taken with the image-stabilization system turned off are discarded

and a median filter is applied to reject outliers. For the purposes of detrending, discontinuities in the data are located, and then detrending is performed by polynomial subtraction, followed by gapfilling using an autoregressive algorithm. Several operations are performed in the pipeline to eventually obtain mode parameters that can be inverted for sound speed and differential rotation, but these are not relevant for this work. The author's work in this chapter begins with the 72-day time series of gapfilled and detrended spherical harmonic coefficients.

There are at least three persuasive reasons for using spherical harmonic reconstructed velocity images for time-distance analysis, the first being that the spherical harmonic time series are readily available data products of the HMI pipeline. Secondly, low resolution images (up to spherical harmonic degree $l = 300$) appropriate for the detection of meridional flow may be reconstructed without introducing random errors due to the sub-sampling and/or smoothing of higher resolution images (assuming that the decomposition and the subsequent reconstruction introduces negligible noise). Thirdly, phase-speed filtering the Fourier transform of the coefficients of a suitably chosen time interval saves computation time. This feature, however, was not implemented in this work; rather the phase-speed filtering was done after the spherical harmonic reconstruction—an inefficiency to be eliminated in future work.

The spherical harmonic reconstruction of velocity images $V(\theta, \phi, t)$ is given by (e.g., Kholikov et al., 2014)

$$V(\theta, \phi, t) = \sum_{l=0}^{l_{\max}} \sum_{m=0}^{m=l} C_l^m(t) P_l^m(\sin\theta) e^{im\phi}, \tag{4.1}$$

where $C_l^m(t)$ is the coefficient time series, P_l^m is the associated Legendre polynomials, θ denotes latitude, and ϕ longitude. The code to implement this was developed by S. Kholikov to reconstruct velocity images from spherical harmonic time series (Burtseva et al., 2008; Kholikov et al., 2014) produced by the GONG pipeline (Hill et al., 2003). The author extended this code with help from S. Kholikov, T. P. Larson, T. L. Duvall, Jr., and P. H. Scherrer to work with the spherical harmonic time series produced by the MDI and HMI pipeline, to generate reconstructed images in the longitude-sin(latitude) grid in addition to the longitude-latitude grid. The code was also modified to reconstruct images that track at the constant equatorial rate in addition to the differential rate.

4.2.2 Reconstruction Code Validation

The spherical harmonic reconstruction code was tested on retiled 1-day coefficient time series at 60 second cadence, that had not yet been detrended or gapfilled, generated from untracked vector-weighted medium-l MDI Dopplergrams regridded onto longitude-sin(latitude) coordinates. The reconstruction was found to be entirely satisfactory (Figure 4.5). The medium-l MDI velocity images were chosen because their low resolution enabled the quick generation of pre-decomposition images, quick reconstruction, and easy visual inspection and comparison.

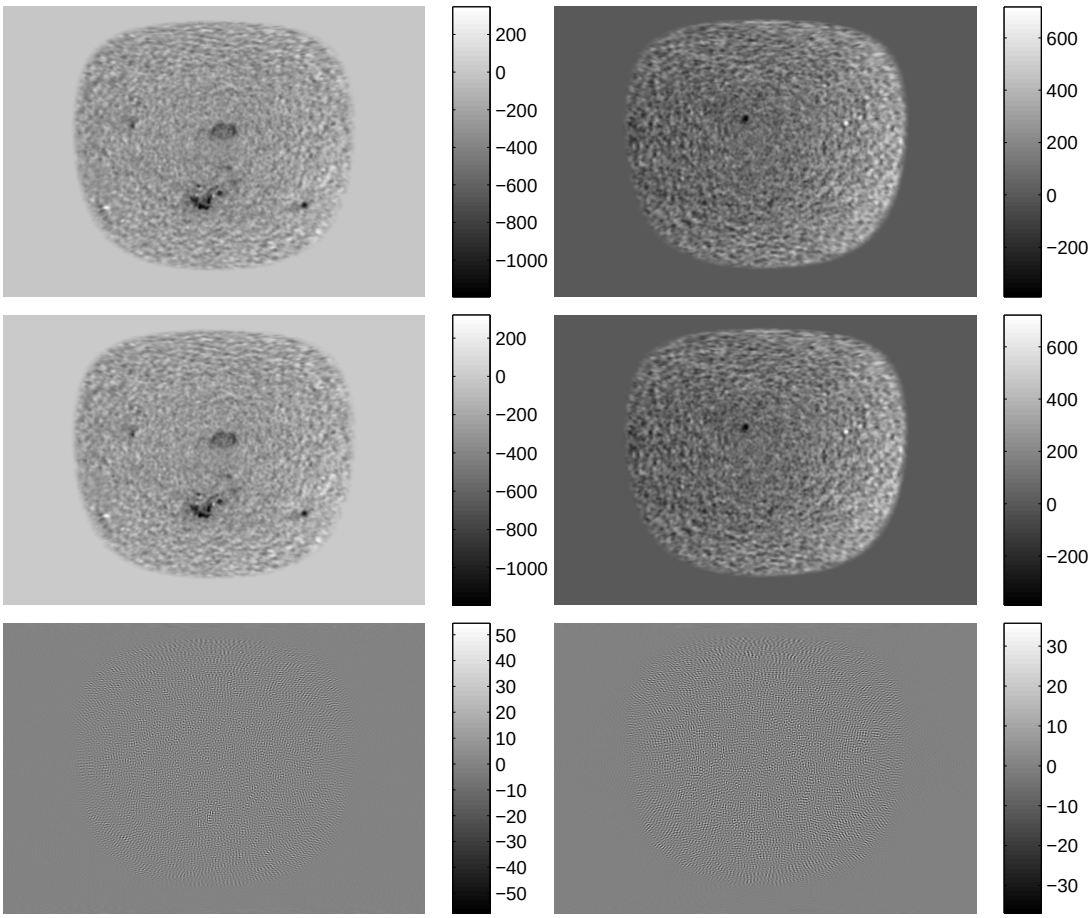

Figure 4.5: MDI velocity images on a 593 × 398 longitude-sin(latitude) grid with pixel size 0.3° × 0.005 taken at 2003.10.29_00:00:00 (left) and 2010.08.03_00:00:00 (right). Top: Input to the spherical harmonic decomposition algorithm with $l_{\max} = 600$ obtained from T. P. Larson. Root mean square (RMS) velocity of available data in the image: 109.18 m/s (left); 92.92 m/s (right). Middle: Spherical harmonic reconstructed image with $l_{\max} = 300$. RMS velocity: 108.79 m/s (left); 92.60 m/s (right). Bottom: Residue between top and bottom images. RMS velocity: 9.09 m/s (left); 7.75 m/s (right). The unit on the colorbar is m/s.

4.2.3 HMI Data Reconstruction

For time-distance analysis, Carrington inclination corrected HMI data spanning May 1, 2010–March 3, 2013 is reconstructed from 1-day long spherical harmonic time series (retiled from 72-day detrended gapfilled chunks available from the HMI global helioseismology pipeline) up to $l = 300$. The images are reconstructed on a 298×298 longitude-latitude grid (pixel size: $0.6^\circ \times 0.6^\circ$) at a 45 second cadence, that track at the equatorial rotation rate. The whole data set, spanning almost 3 years, consists of daily datacubes. The duration of a day implies an azimuthal motion of about 13.33° ($\approx 360^\circ/27$ days) which ensures that, with the available data at midday (middle of the time interval) centered in the image, there is enough data in the central portion of each image sample for robust time-distance measurements. The duration of a day also attempts to alleviate the effects of differential rotation (there is only a 4° relative azimuthal motion between the pole and the equator). A sample of a reconstructed HMI velocity image taken at midday on May 6, 2010 is displayed in Figure 4.6.

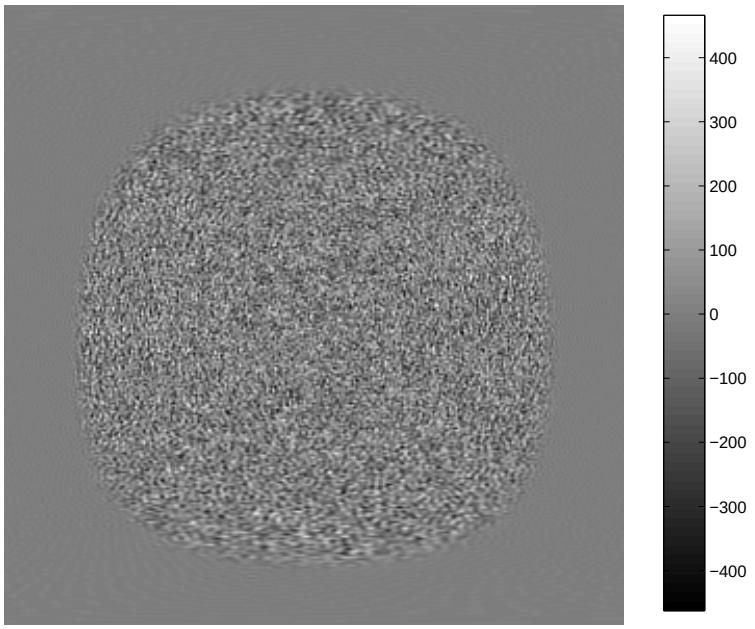

Figure 4.6: Sample of reconstructed HMI velocity image on a 298×298 longitude-latitude grid with pixel size $0.6^\circ \times 0.6^\circ$ taken at midday on May 6, 2010. The unit on the colorbar is m/s. The image is part of a datacube that is reconstructed from 1-day long spherical harmonic time series (retiled from 72-day detrended gapfilled chunks available from the HMI global helioseismology pipeline) up to spherical harmonic degree $l = 300$. RMS velocity of available data in the image is 114.24 m/s.

4.3 The "Center-to-Limb" Effect

For the accurate interpretation of any measurement, it is necessary to remove systematic errors from it. But this is easier said than done, as models must be found for the systematic errors. Mathematical models without a physical basis may suffice if the correction leads to measurements of the primary phenomenon under investigation that are consistent with established models and/or other independent measurements. In the absence of established models, however, the difficulty is compounded as the problem must now be addressed on two, perhaps, multiple fronts: accounting for the primary phenomenon, as well as the systematic errors. A physical accounting of the systematic errors often leads to the discovery of flaws in the instrument design, of unforeseen factors interfering with the experimental setup, of inadequacies of the established models, and more rarely, of new phenomena. Simplifying assumptions are routinely made, such as, the measurement can be neatly partitioned into a signal and an additive non-random "noise". This approach has endured remarkably well with a proven track record. Nonetheless, complexity and nonlinearity abound in multiplicative profusion. Additionally, to err is human.

4.3.1 Background

Between 2012 and 2013 several consequential papers were published pertaining to helioseismic measurement of meridional flow. Zhao et al. (2012) measured travel-time shifts at near-surface layer focal depths (< 14 Mm) from four HMI observables (Doppler velocity, continuum intensity, line-core intensity, and line depth) and the 1600 Å chromospheric data from Atmospheric Imaging Assembly (AIA) instrument aboard SDO. Not only were there non-negligible differences in the north-south or meridional travel-time shifts between the various observables, there was also a significant travel-time shift signal coming from the east-west direction, even after the removal of travel-time signals due to differential rotation (Figure 4.7). However, when the east-west signal was subtracted from the north-south signal, the meridional travel-time shifts computed from all the observables and instruments seemed to agree with one another. This also resulted in a roughly 10 m/s reduction in the inferred meridional flow speed, which is in closer agreement with the results obtained by magnetic feature tracking (Hathaway and Rightmire, 2010) and surface Doppler measurements (Ulrich, 2010). Such a broad level of agreement, at least in the near-surface layers of

the Sun, between different observables and instruments achieved by this "correction" seems to indicate that a mathematical means has been discovered to deal with the systematic error that is the east-west travel-time shift signal, or what is now known as the "center-to-limb" effect.

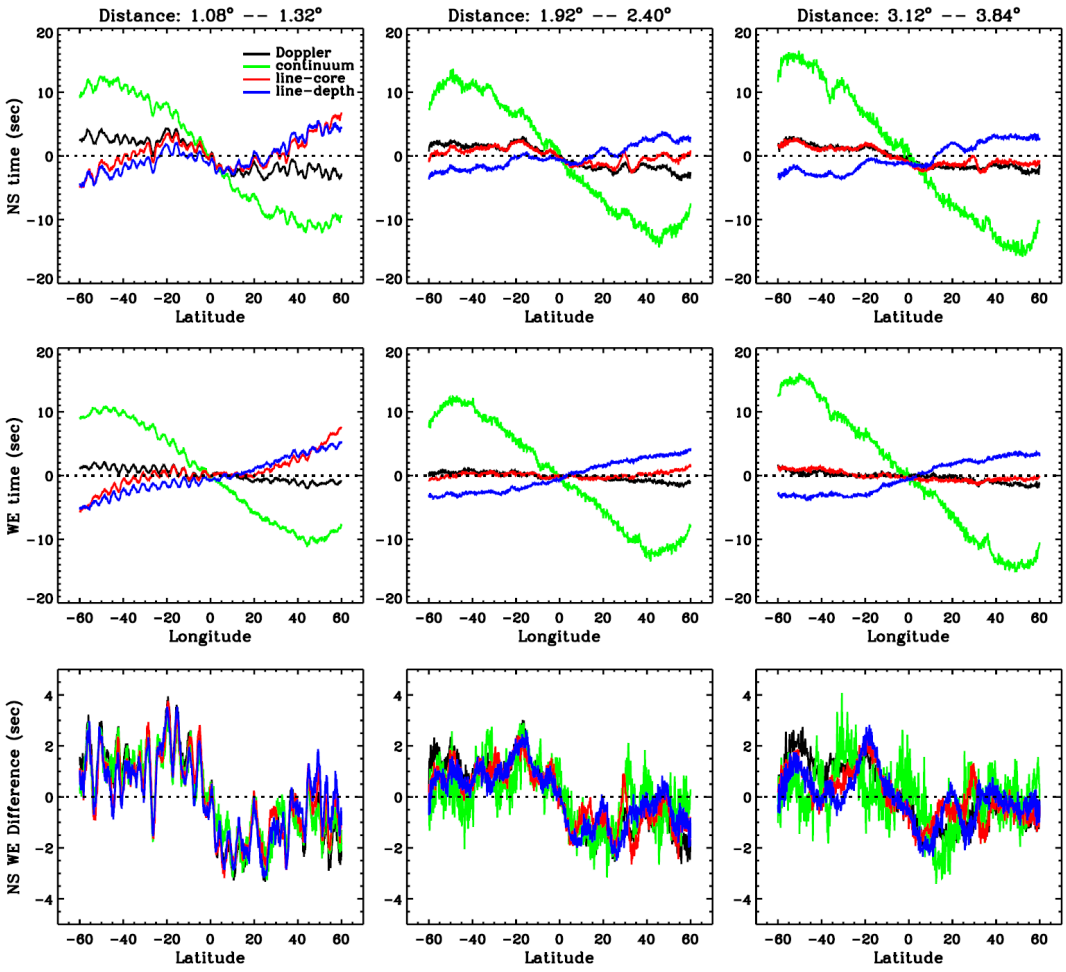

Figure 4.7: Top: Depth-averaged (indicated on top) curves of north-south travel-time shift ($\delta\tau_{\rm ns}$) as a function of latitude, obtained from different HMI observables (Doppler velocity: black; continuum intensity: green; line core: red; line depth: blue). Middle: Depth-averaged curves of west-east travel-time shift ($\delta\tau_{\rm we}$). Bottom: Differences of $\delta\tau_{\rm ns}$ and $\delta\tau_{\rm we}$. Courtesy: Zhao et al. (2012).

This work was followed up by a paper by Baldner and Schou (2012) in which they attempted to provide a physical basis for the correction by computing phase delays from a complex eigenfunction extracted from a numerical simulation of convection, and comparing them with phase shifts to theoretical eigenfunctions with an imposed vertical flow. The idea is that under normal conditions, standing acoustic waves

should have a constant phase with height; however, Baldner and Schou (2012) suggest the possibility that

> a phase variation arises from the large asymmetry between the upflows and downflows in the convection near the solar surface. In particular, the broad upflows and narrow downflows give rise to net vertical flows when horizontally averaged over length scales much smaller than the acoustic modes. As was shown by Gough and Hindman (2010) in the context of meridional flows, a flow introduces a phase shift in acoustic modes—one would expect the vertical convective flows in the Sun to introduce a phase shift with height in the solar atmosphere.

Since the observing height near the solar limb is higher up in the atmosphere compared to the disk center, a net vertical flow imparts an additive phase shift on the modes as

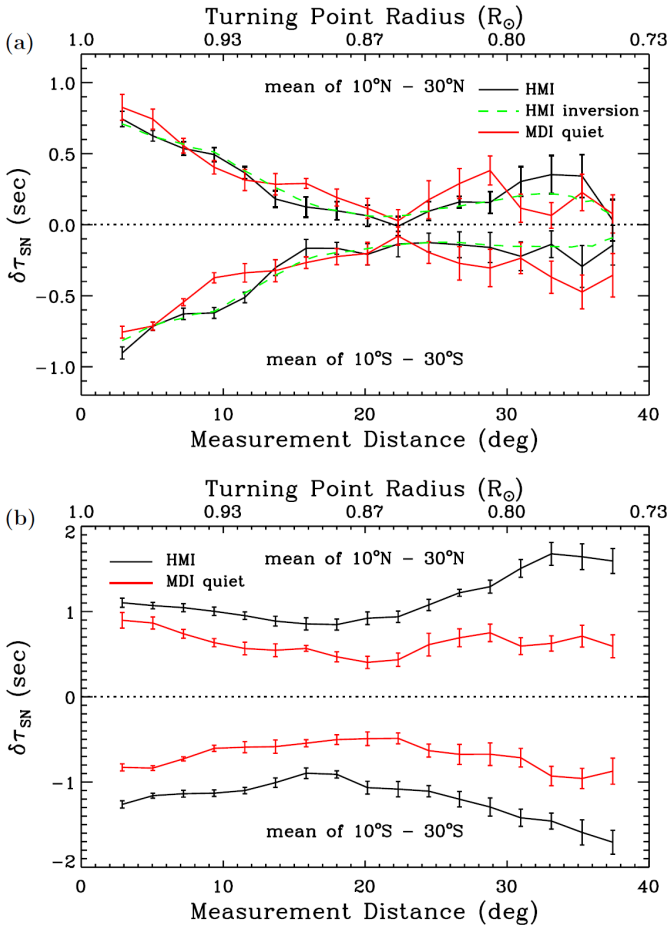

Figure 4.8: (a) Acoustic travel-time shifts ($\delta\tau_{\rm SN}$) extracted from HMI (black) and MDI (red) data after the "center-to-limb" correction, together with $\delta\tau_{\rm SN}$ calculated with ray theory (green) from the velocity inverted from the HMI measurements. (b) Same as (a) but without the correction. Courtesy: Zhao et al. (2013).

a function of observing height and thus heliocentric angle. This justifies the corrective procedure adopted in Zhao et al. (2012).

Zhao et al. (2013) used the "center-to-limb" correction to infer meridional flows down to a radius of $0.75R_\odot$ using HMI and MDI data. They used ray-approximation sensitivity kernels to invert the corrected travel-time shifts (Figure 4.8). The inversion results are shown in Figure 1.4. A poleward flow of 15 m/s extends from the surface to a depth of approximately 65 Mm ($0.91R_\odot$). Below this, the flow direction turns equatorward with a maximum speed of about 10 m/s. Farther beneath, at about $0.82R_\odot$ the flow once again turns poleward. This suggests at least a double-cell structure, radially stacked, with significant hemispheric asymmetry. Later on Schad et al. (2013) published their results on global helioseismic inferences of meridional flow using MDI data, which seemed to indicate multi-cell meridional circulation, not only in the radial direction, but also in the latitudinal direction (cf. Figure 1.2).

4.3.2 Constant Chord-length Geometry

In Zhao et al. (2012, 2013), the time-distance analysis is confined to a narrow strip (15–20°) along the central meridian or the equator (cf. Figure 4.9), and 30° common-midpoint sector geometry is used to calculate $\delta\tau_{\rm ns}$ and $\delta\tau_{\rm we}$, respectively. This was done presumably to isolate the "center-to-limb" effect from contamination due to the difference in the coordinate geometry in the north-south direction (longitudinal great-circles) compared to the east-west direction (latitudinal circles)—the idea being that sufficiently narrow strips along the central meridian and equator have roughly the same geometry. Also, restricting the time-distance measurements to narrow strips along the central meridian and the equator prevents diluting contributions to the center-to-limb variation from near-limb meridians—in a true heliocentric angle dependent center-to-limb effect, measurement along meridians that are closer to the limb are less sensitive to center-to-limb phase variations. Nevertheless, in the case of large separation angles or skip distances, even the 30° arcs used in Zhao et al. (2013) extend far beyond the 20° strip, thus introducing contaminations the innovation sought to avoid in the first place.

At first cross-correlating a single pair of pixels instead of a whole arc of them, oriented along the meridians (e.g., Giles et al., 1997), or the latitudes within the 20° strip (cf. Figure 4.9) seemed appealing since that completely eliminated the possibility

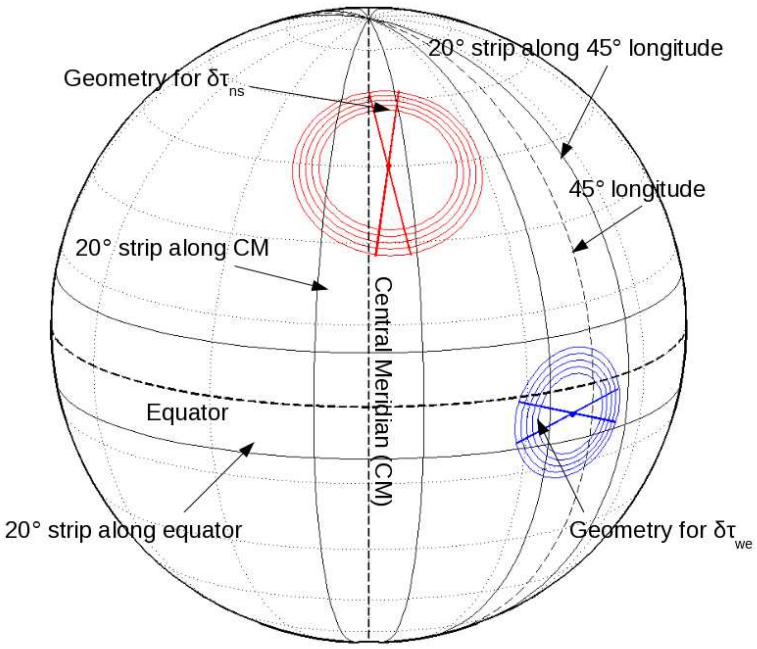

Figure 4.9: Geometry of time-distance analysis used in Zhao et al. (2012, 2013) and in this work. Shown are the strips along the central meridian, 45° longitude, and the equator where time-distance analysis is confined. Also shown are the north-south (red) and east-west (blue) deep-focus geometries. The B_0-angle is 15°.

of excursions outside the strips, besides being computationally much faster than the quadrant technique. But a few preliminary experiments deemed the method too noisy. A compromise was struck where a small, user-specified number of pixels along the arcs with a given skip distance is cross-correlated. This method too is computationally faster than the quadrant geometry due to the reduced number of pixels involved in the cross-correlations, especially at large skip distances. T. L. Duvall, Jr. made the necessary modifications to the existing time-distance code. Subsequent tests showed a significantly improved signal-to-noise over the single-pair method. The signal-to-noise, as expected, was worse compared to the standard quadrant technique (cf. Figure 4.11).

At this point it was realized that if the number of pixels were kept constant and were located at appropriate azimuthal separations along the arc for any sufficiently large skip distance, the chord-length of the arc could be kept constant regardless of the skip distance. Thus, whereas the sector angle remains constant and the chord-length changes in proportion to the skip distance in the standard sector geometry, in the constant chord-length (CCL) technique the chord-length stays constant and the sector angle changes in inverse proportion to the skip distance or separation angle

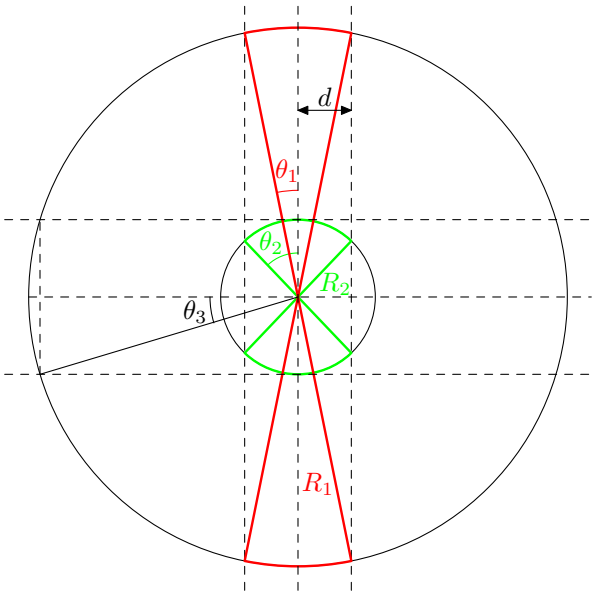

Figure 4.10: Comparison of two common-midpoint geometries with constant chord-length. The arcs of the larger (planar radius R_1 and half-angle θ_1) and smaller (planar radius R_2 and half-angle θ_2) separation distance have the same chord-length ($2d$). If the smaller annulus were located on the surface of a sphere of radius R_1, it would subtend a half-angle of θ_3 to the center of the sphere, in a plane bisecting the annulus.

(cf. Figure 4.10). This ensures that the azimuthal extent of the arc stays the same regardless of the skip distance or focal depth and confines the arcs within the strips except at very high latitudes.

In Figure 4.10, where two common-midpoint geometries with different planar radii are displayed, it can be seen that the condition for constant chord-length is satisfied if

$$d = R_2 \sin\theta_2 = R_1 \sin\theta_1, \tag{4.2}$$

where $2d$ is the chord-length, $2R_1$ and $2\theta_1$ are the planar (in the plane of the circle) separation distance (or diameter) and sector angle, respectively, of a larger common-midpoint annulus (red in Figure 4.10), and $2R_2$ and $2\theta_2$ are the planar separation distance and sector angle, respectively, of a smaller common-midpoint annulus (green in Figure 4.10). Equation (4.2) may be formulated in a more useful form, in terms of the angular separation distance $2\theta_3$ of the smaller common-midpoint annulus on the surface of a sphere of radius R_1:

$$\sin\theta_2 = \frac{\sin\theta_1}{R_2/R_1} = \frac{\sin\theta_1}{\sin\theta_3}, \tag{4.3}$$

This establishes a relationship between the half-angles (θ_1, θ_2) of two common-midpoint geometries with arcs that have the same chord-length ($2d$), and the (half) separation angle (θ_3) of the smaller common-midpoint annulus on the surface of a sphere with a diameter ($2R_1$) that equals the planar separation distance or planar diameter of the larger common-midpoint annulus. Now if θ_1 and θ_2 are "small", the relation $\theta \approx \sin\theta$ may be used to approximate Equation (4.3) as

$$\theta_2 \approx \frac{\theta_1}{\sin\theta_3}. \tag{4.4}$$

Equation (4.4) will obviously break down in cases where the chord-length and the planar diameter of the smaller common-midpoint geometry become comparable.

If $R_1 = R_\odot$ then $2\theta_3 = \Delta$, where Δ is the skip distance (separation angle on the surface of the Sun) of the smaller common-midpoint geometry, and Equation (4.4) becomes

$$\theta_2 \approx \frac{\theta_\odot}{\sin(\Delta/2)}, \tag{4.5}$$

where $2\theta_\odot$ is the sector angle of a common-midpoint annulus that coincides with circumference of the Sun, that satisfies the constant chord-length condition with the smaller common-midpoint geometry.

For a small number of pixels, and for a sufficiently large skip distance Δ, the azimuthal separation between the pixels that satisfies the constant chord-length condition with a pixel sized arc with radius $R_\odot$ can be calculated thus:

$$\text{azimuthal separation} \approx \frac{\text{mapscale or pixel size in degrees}}{\sin(\Delta/2)}. \tag{4.6}$$

In other words, the azimuthal separation calculated using Equation (4.6), along an arc with common-midpoint skip distance Δ, has roughly the same chord-length as a pixel-size azimuthal separation on an arc with radius $R_\odot$. Thus, the user-specified number of pixels along the arc roughly specifies the chord-length of the arc (strictly speaking, the arc-length) and keeps it constant across various skip distances. For a full deep-focus geometry, Δ can be chosen to be the angular separation distance of the largest annulus, thus satisfying the CCL condition for the largest arc of a particular geometry for different focal depths.

Every new technology must be calibrated against an established one (cf. Figure 4.11). One of the predictions made of the new technique was increased noise levels

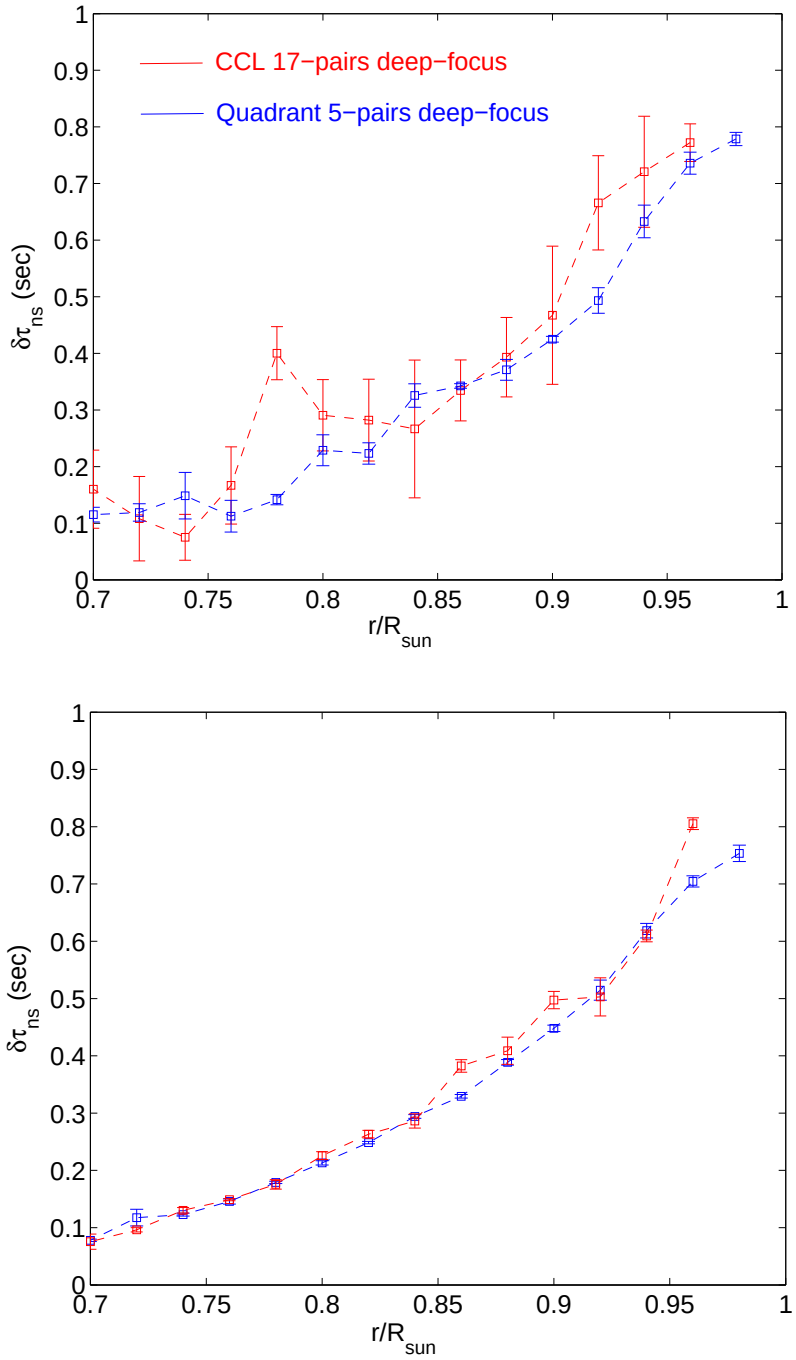

Figure 4.11: Constant chord-length (CCL) 17-pairs deep-focus geometry (red) with 9 pixels on each arc, tested on 9 hours of HLD06/R06 simulation data against 5-pairs quadrant deep-focus geometry (blue). $\delta\tau_{\rm ns}$ shown is averaged over 45° N and S longitudes. No further averaging is done over latitude or depth. The data point at $0.98R_\odot$ for the CCL case was an outlier and discarded. Top: Without noise subtraction. Bottom: With noise subtraction.

due to fewer pixels used to calculate the cross-covariances, and thus fewer samples of cross-covariances being averaged. The other concern was how the decreasing sector angle with increasing common-midpoint skip distance (or focal depth) would affect the travel-time shift values relative to the standard sector geometry. The prediction was that the narrower sectors of the CCL technique at the larger skip distances would become less sensitive to the non-north-south contributions to the meridional flow measurements, leading to a slight increase in the value of the travel-time shifts relative to the standard geometry. Testing with all the simulations discussed in Chapter 3 confirmed the former prediction. However, the travel-time shift values calculated using the standard and non-standard techniques were found to be virtually indistinguishable within error bars and in the absence of realization noise (except at the smallest distances due to a combination of inadequate resolution and failure of the CCL condition). Figure 4.11 shows the comparison results for the worst-case scenario, since the HLD06/R06 simulation spans only 9 hours—the shortest duration of all the simulation datacubes mentioned in Chapter 3. Both the noise unsubtracted (Figure 4.11, top) and subtracted (Figure 4.11, bottom) results ($\delta\tau_{\rm ns}$ in the northern and southern hemispheres are averaged together) are displayed to indicate the relative noise levels and the relative signal levels (in the absence of realization noise) of the measurements.

4.3.3 Time-Distance Analysis and Results

The *heliocentric angle* of a location on the solar disk is the angle subtended by an arc between that location and the center of the solar disk to the center of the Sun. A true center-to-limb effect on an observable is dependent only on the heliocentric angle. The center-to-limb effect on an observable is maximized in a direction perpendicular to the lines of constant heliocentric angle (cf. Figure 4.17) and nullified along the isolines of heliocentric angle. For instance, some radially varying phenomenon within the Sun will be observed at different heights in the solar atmosphere when measured at different heliocentric angles on the solar disk, and result in a center-to-limb effect. When measurements of this observable are made along lines perpendicular to lines of constant heliocentric angle, for example any diameter of the disk, the observed height differential is maximized with the consequent maximization of the center-to-limb effect on the observable of interest. Along isolines of heliocentric angle, the observed height is the same, and therefore, no center-to-limb effect is observed in

measurements along the isolines.

As a consequence, an observable measured along longitudes other than the central meridian, and latitudes other than the equator are less susceptible to the center-to-limb effect. Measurements made along $\pm 90^\circ$ longitudes will not see any center-to-limb effect, with increasing center-to-limb variation observed as target longitudes approach the central meridian (cf. Figure 4.18). For a more quantitative analysis the reader is referred to Section 4.3.5.

The above considerations are applied systematically to the time-distance analysis of HMI data spanning May 1, 2010–March 3, 2013, to ascertain if the "center-to-limb" effect discussed in Section 4.3.1 is a bonafide center-to-limb effect. The datacube is reconstructed from spherical harmonic time series as described in Section 4.2.3 and then phase-speed filtered (Section 2.2.1). $\delta\tau_{\rm ns}$ are computed along the central meridian and $\pm 45^\circ$ longitudes, and $\delta\tau_{\rm we}$ are computed along the equator and $\pm 45^\circ$ latitudes within a 20° strip (cf. Figure 4.9). $\pm 60^\circ$ longitudes would have been better for the analysis, but they are too close to the edges of the available data in the reconstructed images due to the cropping and apodization procedure carried out in the HMI data pipeline. Higher latitudes were not considered due to the lack of sufficient number of uncorrelated data points. The time-distance analysis is carried out with the CCL technique discussed in Section 4.3.2 in the 17-pairs deep-focus geometry on each daily datacube. After averaging the cross-covariance functions as discussed in Section 2.2.3, they are then averaged over the 20° strip around the latitude or longitude of choice. To further improve the signal-to-noise ratio, the cross-covariance functions are averaged over non-overlapping periods of 30 days. These are then fit with Gabor-wavelet functions and differenced (cf. Section 2.2.4) to obtain travel-time shifts for each 30-day interval. These travel-time shifts are combined over the entire 2.92-year span to yield the mean travel-time shifts and the standard errors of the mean. Travel-time shifts due to differential rotation are removed from $\delta\tau_{\rm we}$. The author had to develop a pipeline code to perform these data-intensive computations.

Figure 4.12 compares the plots of $\delta\tau_{\rm ns}$ along the central meridian and $\delta\tau_{\rm we}$ along the equator as functions of latitude and longitude respectively, for focal depths of $0.96R_\odot$, $0.92R_\odot$, $0.86R_\odot$, and $0.80R_\odot$. Figure 4.13 shows the corrected and uncorrected $\delta\tau_{\rm sn}$ along the central meridian as a function of focal depth for latitude ranges 25–35° and 40–50° north and south. The corrected $\delta\tau_{\rm sn}$ is calculated by simply subtracting $\delta\tau_{\rm ew}$ along the equator, also shown in Figure 4.13, from the uncorrected $\delta\tau_{\rm sn}$ along

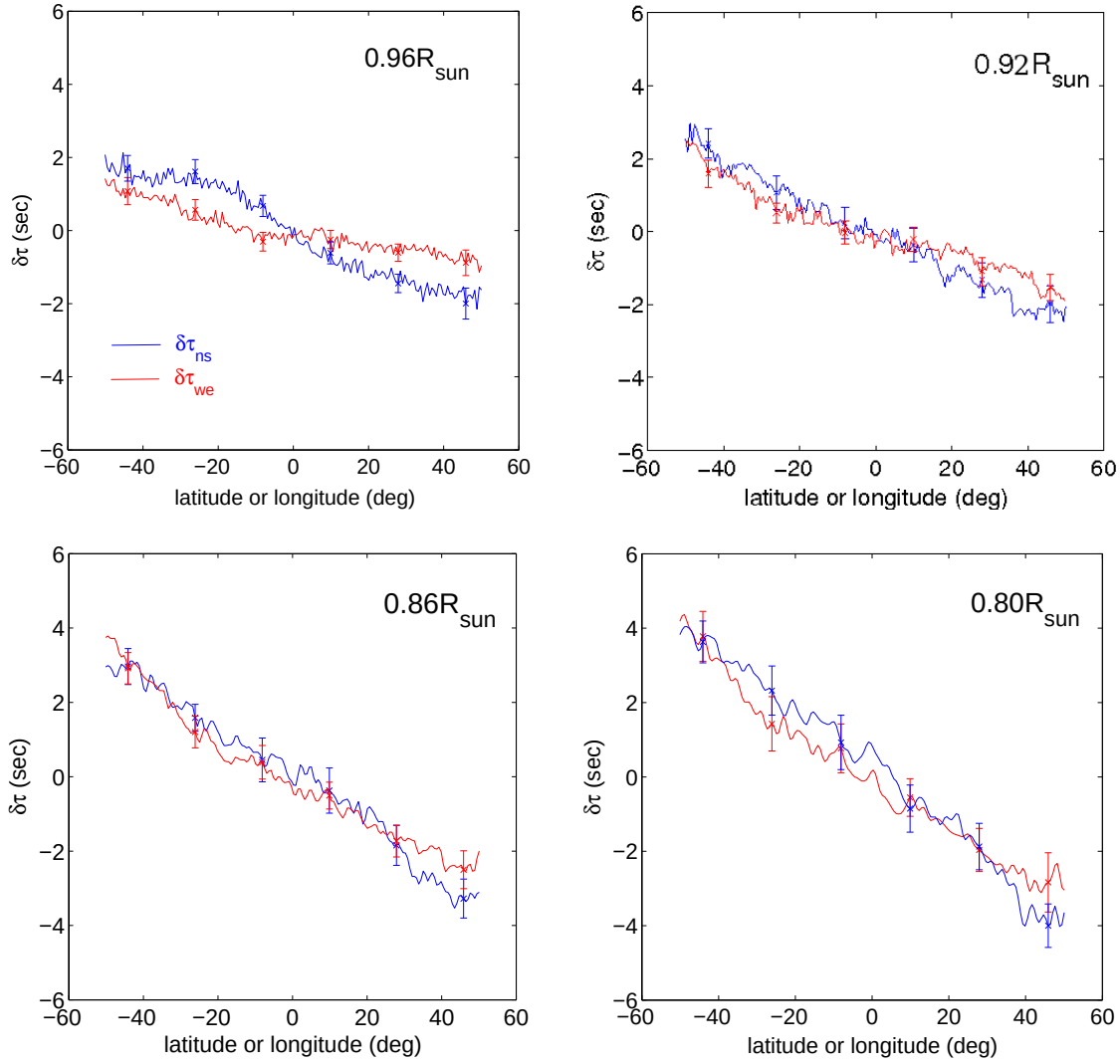

Figure 4.12: North-south ($\delta\tau_{\rm ns}$, blue) and west-east ($\delta\tau_{\rm we}$, red) travel-time shift as a function of latitude and longitude respectively, at focal depths: $0.96R_\odot$ (top left), $0.92R_\odot$ (top right), $0.86R_\odot$ (bottom left), and $0.80R_\odot$ (bottom right). Computations are done on HMI data spanning May 1, 2010–March 3, 2013. The mean travel-time shift due to differential rotation between $\pm 10^\circ$ latitudes is removed from $\delta\tau_{\rm we}$.

the central meridian, as prescribed by Zhao et al. (2012, 2013). See also Figure 3 of Kholikov et al. (2014). Since there are no clear criteria for subtracting $\delta\tau_{\rm we}$ or $-\delta\tau_{\rm ew}$, $\delta\tau_{\rm ew}$ is antisymmetrized before performing the correction. The SN/EW convention is adopted in Figure 4.13 as in Zhao et al. (2013) and Kholikov et al. (2014) instead of the NS/WE convention in the other figures, so that the travel-time shifts in the northern hemisphere and western hemisphere are positive.

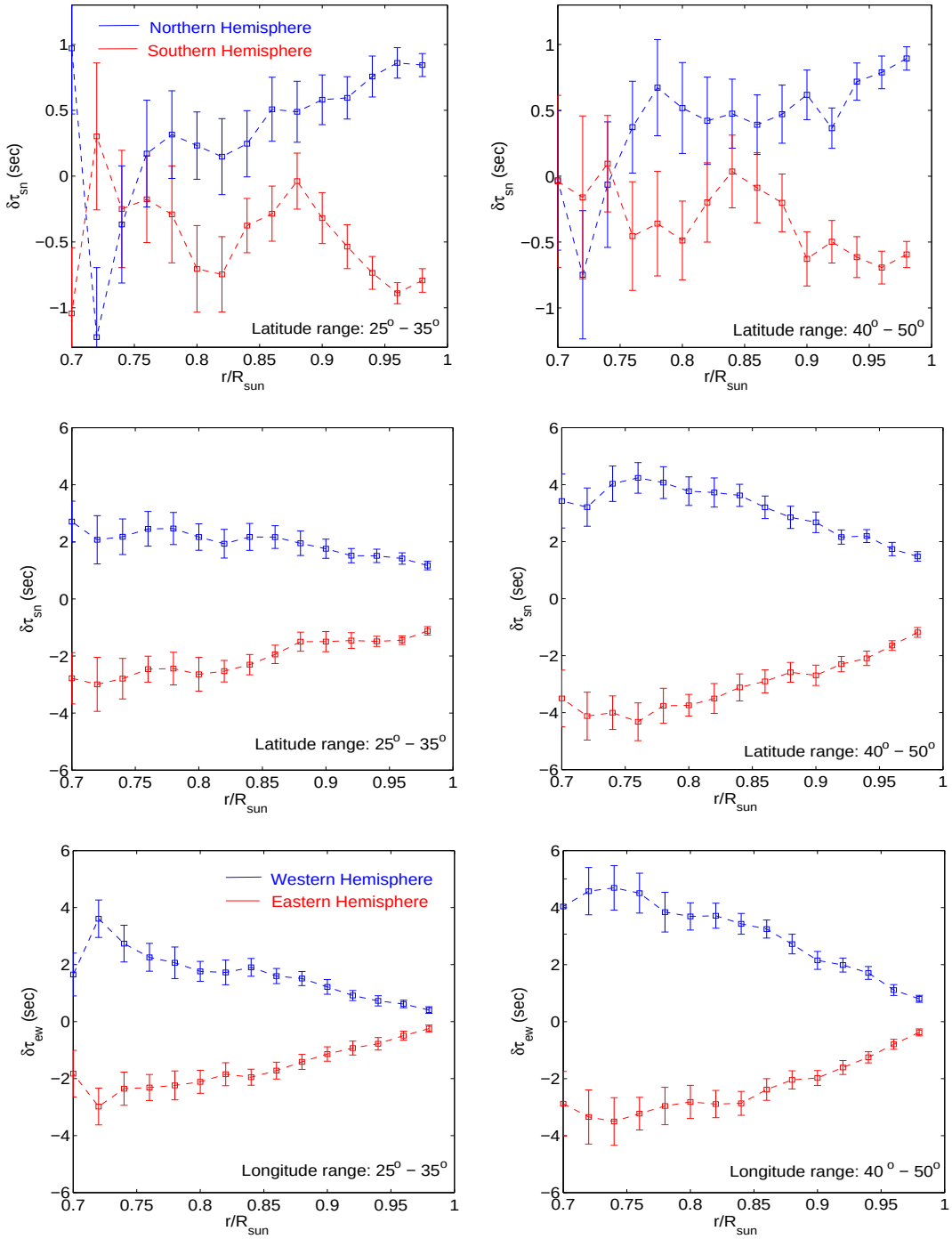

Figure 4.13: Top two panels show corrected (top) and uncorrected (middle) $\delta\tau_{\rm sn}$ as a function of focal depth ($r/R_{\rm sun}$), averaged over latitude ranges (left) 25°–35° and (right) 40°–50°. Bottom panel: $\delta\tau_{\rm ew}$ correction, averaged over longitude ranges (left) 25°–35° and (right) 40°–50°. Computations are done on HMI data spanning May 1, 2010–March 3, 2013. The top panel shows error bars of $\pm\sigma$ for visual clarity, whereas the other panels show error bars of $\pm 2\sigma$, where σ is the standard error of mean. Note the different scale of the top panel.

Figure 4.14 compares the plots of $\delta\tau_{\rm ns}$ along the central meridian and $\pm 45^\circ$ longitudes as functions of latitude, and Figure 4.15 compares the plots of $\delta\tau_{\rm we}$ along the equator and $\pm 45^\circ$ latitudes as functions of longitude, for the same focal depths as in Figure 4.12.

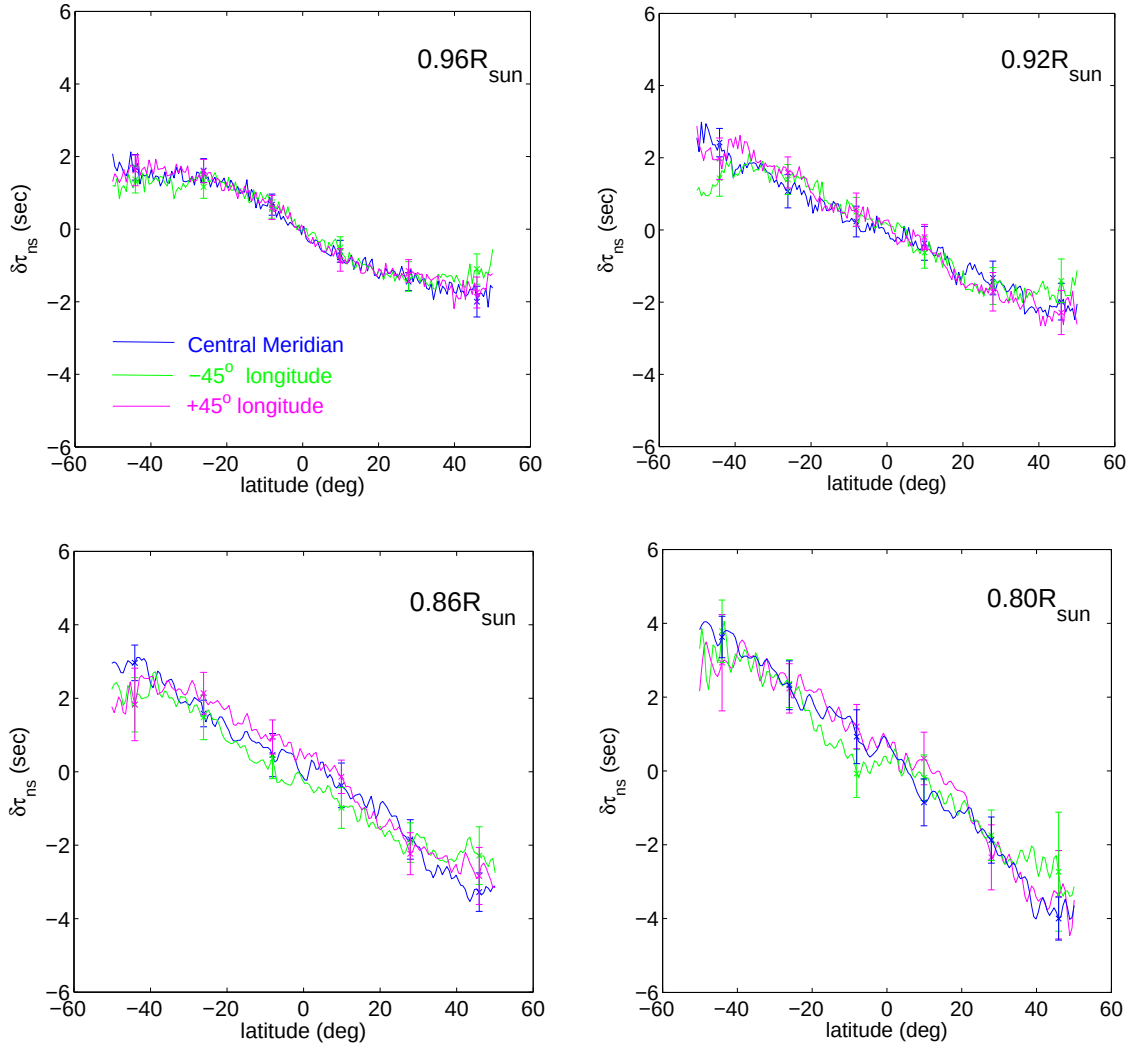

Figure 4.14: North-south travel-time shift ($\delta\tau_{\rm ns}$) as a function of latitude at the central meridian (blue), -45° (green), and +45° (magenta) longitudes, at focal depths: $0.96R_\odot$ (top left), $0.92R_\odot$ (top right), $0.86R_\odot$ (bottom left), and $0.80R_\odot$ (bottom right). Computations are done on HMI data spanning May 1, 2010–March 3, 2013.

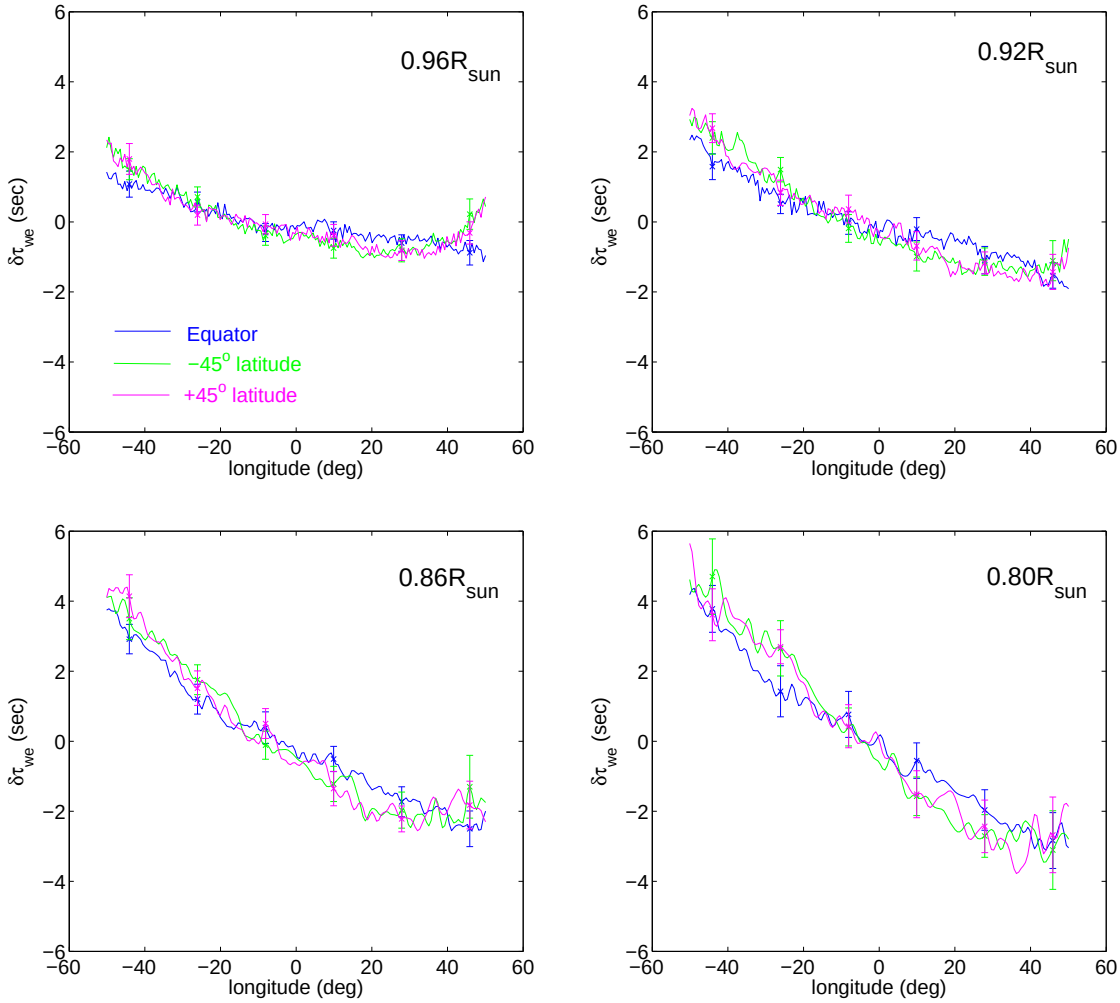

Figure 4.15: West-east travel-time shift ($\delta\tau_{\rm we}$) as a function of longitude at the equator (blue), -45° (green), and +45° (magenta) latitudes, at focal depths: $0.96R_\odot$ (top left), $0.92R_\odot$ (top right), $0.86R_\odot$ (bottom left), and $0.80R_\odot$ (bottom right). Computations are done on HMI data spanning May 1, 2010–March 3, 2013.

4.3.4 Discussion

The results in Section 4.3.3 are intriguing. This is the very first time that the full deep-focus time-distance technique is applied on spherical harmonic reconstructed and phase-speed filtered HMI velocity data to measure meridional flow induced travel-time shifts. It also marks the first use of the newly-devised CCL technique for time-distance computations. It is encouraging that these techniques yielded results consistent with the time-distance measurements of Zhao et al. (2012, 2013) and Kholikov et al. (2014).

Figure 4.12 shows that at smaller focal depths, $\delta\tau_{\rm ns}$ exceeds $\delta\tau_{\rm we}$ in amplitude,

while at larger focal depths the two become indistinguishable within error bars. This suggests that the meridional flow signal dominates at the smaller focal depths and the "center-to-limb" signal dominates at the larger focal depths. The former is to be expected from theoretical considerations, since the sensitivity of propagating acoustic waves to flows would diminish with depth due to the increase in the sound speed; the latter would require an explanation like the one provided by Baldner and Schou (2012): a phase difference that is proportional to the observed height difference, and therefore proportional to the heliocentric angle difference. There may, however, be other reasons for a heliocentric angle dependent phase.

Figure 4.13 shows what has by now become "standard" practice: the correction of the south-north travel-time shifts by subtracting out the east-west travel-time shifts or the "center-to-limb" variation. The amplitudes of the corrected travel-time shifts are of the same order of magnitude as those in Zhao et al. (2013) and Kholikov et al. (2014), and similar features are discernible, such as the generally decreasing values with depth and the humps at larger depths, even the changing sign near the base of the convection zone (cf. Kholikov et al., 2014). The asymmetry in the corrected south-north travel-time shifts between the two hemispheres is discernible. Also shown in Figure 4.13 is the east-west travel-time shift or the "center-to-limb" variation; it is almost linear with focal depth.

Figures 4.14 and 4.15 show that within error bars, $\delta\tau_{\rm ns}$ along the central meridian and $\pm 45^\circ$ longitudes are indistinguishable (except may be at the higher latitudes), and $\delta\tau_{\rm we}$ along the equator and $\pm 45^\circ$ latitudes are indistinguishable (except may be at the higher longitudes). Does this mean that the "center-to-limb" effect is not a true center-to-limb effect, or are the measurements too noisy to make that determination?

Early on, the author had calculated north-south travel-time shifts ($\delta\tau_{\rm ns}$) from HMI data spanning May 6–July 8, 2010 with quadrant 5-pairs deep-focus geometry. At that time the available spherical harmonic coefficient time series had been generated from HMI Dopplergrams that had not been corrected for Carrington inclination. Figure 4.16 compares these $\delta\tau_{\rm ns}$ values with those computed using the CCL 17-pairs deep-focus technique. The closeness of the two results are reassuring, despite the greater noise levels of the CCL technique. Most of the deviations between the two fall within each other's error bars, but the deviations appear to be systematic: they increase with increasing focal depth, and the quadrant $\delta\tau_{\rm ns}$ deviates toward lower amplitudes, noticeably at the higher latitudes. Is this merely random noise or could this be a

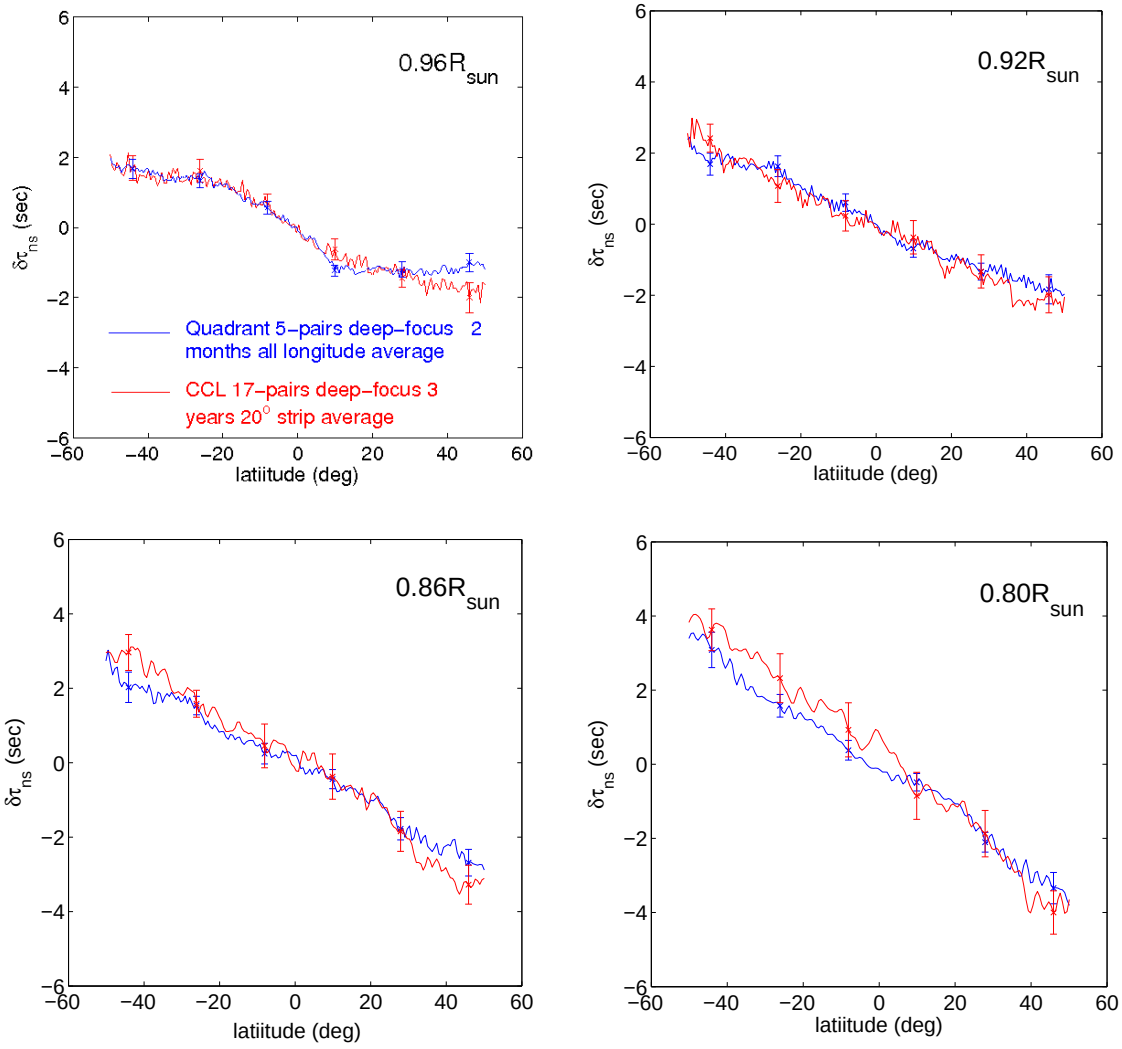

Figure 4.16: Meridional travel-time shift ($\delta\tau_{\rm ns}$) as a function of latitude with quadrant 5-pairs and CCL 17-pairs deep-focus geometry, at focal depths: $0.96R_\odot$ (top left), $0.92R_\odot$ (top right), $0.86R_\odot$ (bottom left), and $0.80R_\odot$ (bottom right). Computations with standard quadrant geometry (blue), averaged over all available longitudes, are done on HMI data without the Carrington inclination correction, spanning May 6–July 8, 2010. Computations with non-standard CCL geometry (red), averaged over 20° along CM, are done on Carrington inclination corrected HMI data spanning May 1, 2010–March 3, 2013.

manifestation of the center-to-limb effect, or rather a diminution of it in the quadrant case due to the near-limb contributions from averaging over all longitudes? The Carrington inclination correction may also be partially responsible for the differences. The size of the error bars precludes a definite conclusion.

4.3.5 Postscript: Center-to-Limb Phase Shift

Interpretation of data requires guidance from theory. In this section a simple theoretical model is constructed for the center-to-limb effect and compared with the "center-to-limb" effect apparent in the HMI data analyzed in this work.

It is postulated that the "center-to-limb" effect is due to a phase difference or phase shift experienced by propagating acoustic waves due to a radially varying phenomenon which imparts a radially and monotonically changing additive phase shift. Since the acoustic waves are observed at the "surface" of the Sun, and different heights in the solar atmosphere constitute the solar surface at different heliocentric angles (the observed height being the deepest at the disk center and becoming increasingly shallow with increasing heliocentric angle), in the absence of all other phenomena (e.g., flows, magnetic fields) the relative change in the phase shift between any two locations on the solar disk is a function of the heliocentric angles (θ_1, θ_2) of those locations. This relative phase shift manifests as a travel-time difference or travel-time shift $\delta\tau(\theta_1, \theta_2)$ in a wave propagating between these two locations. For a pair of locations (θ_1, θ_2) with angular separation Δ, the travel time for a wave propagating from location with heliocentric angle θ_1 to heliocentric angle θ_2 is given by

$$\tau_+ = \tau(\Delta) + \delta\tau(\theta_1, \theta_2)/2, \tag{4.7}$$

and for a counter-propagating wave by

$$\tau_- = \tau(\Delta) + \delta\tau(\theta_2, \theta_1)/2 = \tau(\Delta) - \delta\tau(\theta_1, \theta_2)/2, \tag{4.8}$$

where $\tau(\Delta)$ is the travel time of the wave in the absence of any perturbation. The travel-time shift between the counter-propagating waves is thus obtained:

$$\tau_+ - \tau_- = \tau(\Delta) + \delta\tau(\theta_1, \theta_2)/2 - \tau(\Delta) + \delta\tau(\theta_1, \theta_2)/2 = \delta\tau(\theta_1, \theta_2). \tag{4.9}$$

The result in Equation (4.9) is the reason why the factor of 1/2 is introduced into the phase shift $\delta\tau(\theta_1, \theta_2)$ in Equations (4.7) and (4.8). It divides out the factor of 2 in the phase shift that would have otherwise appeared in Equation (4.9).

Referencing Figure 4.17, the lines of constant heliocentric angle coincide with the lines of constant center-to-limb phase shift, as per the definition of the center-to-limb variation. This implies that the phase shift between any two points on two given

isolines is invariant with respect to the path traversed between the two points. Thus for the separation angle shown in Figure 4.17 along the 45° line of longitude, the phase shift is identical with the phase shift of the separation angle marked out on the equator and the central meridian by the same two isolines. Therefore, if $\delta\tau(\theta_1, \theta_2)$ is fully specified on the equator or the central meridian, it is fully specified everywhere on the disk. It follows from this, that $\delta\tau(\theta_1, \theta_2)$ can be determined along the 45° longitude, or any other longitude for that matter, for a restricted range of (θ_1, θ_2).

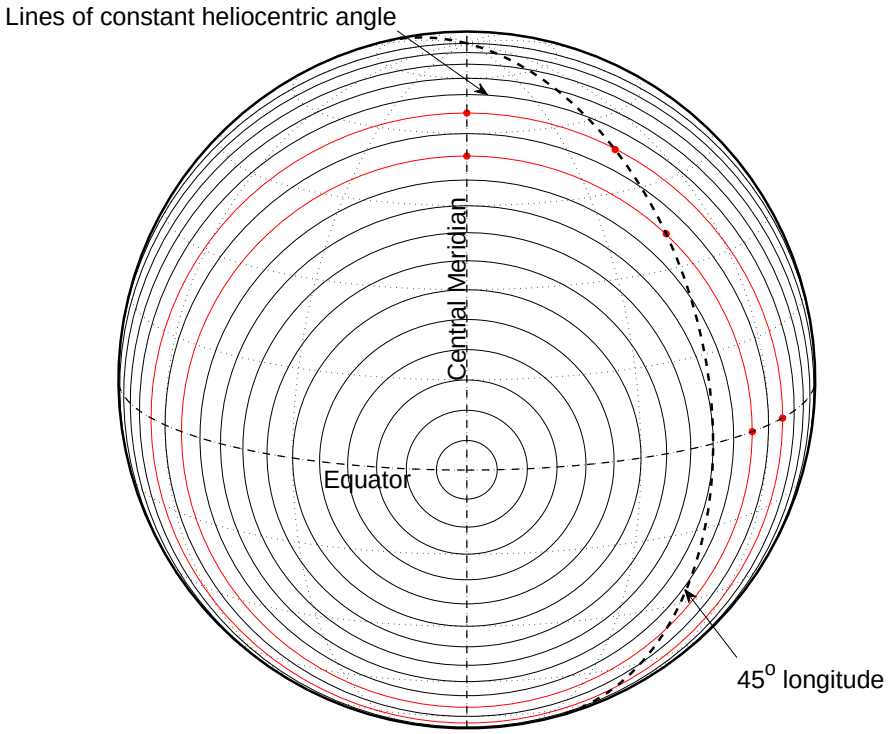

Figure 4.17: Geometry of heliocentric angle dependent center-to-limb phase shift. Indicated are the lines of constant heliocentric angle (also lines of constant center-to-limb phase shift), equator, central meridian, and 45° longitude. Two lines of constant heliocentric angle (with, e.g., heliocentric angles θ_1 and θ_2) are highlighted in red (with, e.g, center-to-limb phase shifts $\delta\tau(0, \theta_1)$ and $\delta\tau(0, \theta_2)$, respectively) to show the relationship between the separation distance and central latitude with a particular phase shift ($\delta\tau(\theta_1, \theta_2) = \delta\tau(0, \theta_1) - \delta\tau(0, \theta_2)$) on 45° longitude, and the separation distance and central longitude (latitude) with the same phase shift on the equator (central meridian). The separation distances are marked with big red dots. Note that in this figure the center of the visible solar disk is tipped downward by an angle of 15° for visual clarity and perspective. So the actual line of sight of the observer is inclined downward by 15° from the normal to the plane of this page.

However, from the data analysis what is obtained is the phase shift function, $\delta\tau(\Delta, \phi)$ or $\delta\tau(d_f, \phi)$, in terms of the separation angle Δ (or common-midpoint skip distance or focal depth d_f) between a pair of heliocentric angles, and longitude ϕ. Thus, from a given equatorial phase shift function or center-to-limb travel-time shift function or east-west travel-time shift $\delta\tau_{ew}(\Delta, \phi)$, the center-to-limb phase shift function $\delta\tau_{sn}(\Delta', \psi)$ projected along any longitude, can be fully determined, ψ being the latitude on the longitude of interest. The separation angles Δ', along any given longitude, between heliocentric-angle pairs (θ_1, θ_2), map uniquely to separation angles $\Delta = |\theta_1 - \theta_2|$ between the same heliocentric-angle pairs on the equator at a longitude of $\phi = (\theta_1 + \theta_2)/2$. This makes it possible to map $\delta\tau_{ew}(\Delta, \phi)$ to $\delta\tau_{sn}(\Delta', \psi)$ along any longitude. In this work this mapping is done onto the 45° longitude. Higher longitudes, though preferable, were not available due to the cropping and apodization scheme of the HMI global helioseismology pipeline.

Figure 4.18 shows the model center-to-limb phase shift function, and the projection of the center-to-limb phase shift function at various longitudes. In the interest of time, the author constructed a "quick and dirty" model by eyeballing the relevant measured travel-time shifts in Figures 4.12 (the north-south travel-time shifts at the

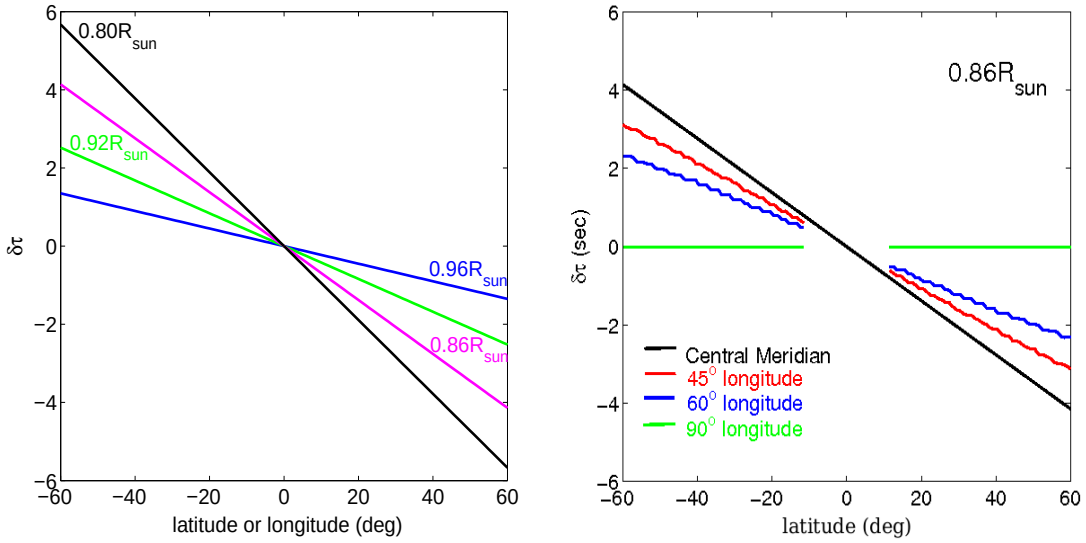

Figure 4.18: Center-to-limb phase shift model. Left panel shows the linear variation of the center-to-limb phase shift function $\delta\tau(d_f, \phi)$ with longitude (for the equator) or latitude (for the central meridian), for the different separation angles or focal depths d_f ($0.96R_{sun}$: blue; $0.92R_{sun}$: green; $0.86R_{sun}$: magenta; $0.80R_{sun}$: black). Right panel shows the projection of the center-to-limb phase shift function as a function of latitude on various longitudes: 0° (black), 45° (red), 60° (blue), 90° (green).

larger focal depths) and 4.13 (the east-west travel-time shifts). The model is kept simple by adopting a bilinear phase shift or travel-time shift variation with longitude and with the focal depth. This model closely resembles the relevant plots in Figures 4.12 and 4.13. In future work accurate models will be constructed by appropriate fitting of the aforementioned plots.

As expected in the model (as per the discussion in Section 4.3.4), the projection of the center-to-limb phase shift function shows decreasing values with increasing longitudes. However, as shown in Figure 4.19, the deviation in the data is not clearly discernible at ±45° longitudes, at the current noise levels. Therefore, it is not possible to confirm or disconfirm whether the "center-to-limb" effect corresponds to a true center-to-limb phase shift function. ±60° longitudes may provide a better test for the "center-to-limb" variation, provided that travel-time shifts with adequate signal-to-noise can be extracted at those high longitudes. With HMI the expectations remain rather high. In a few years, with longer time series, a resolution may yet be possible.

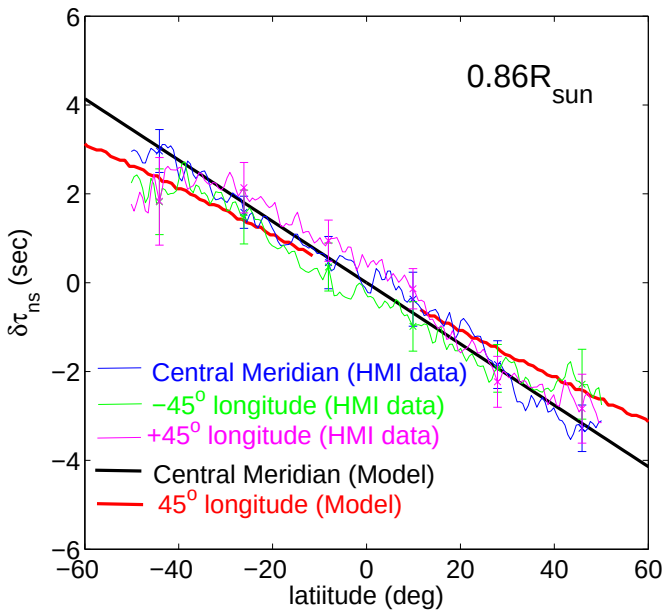

Figure 4.19: The model center-to-limb phase shift function at central meridian (black) and the projection at 45° longitude (red) are compared with the "center-to-limb" variation seen in the north-south travel-time shifts calculated from HMI velocity data at a focal depth of $0.86R_{\rm sun}$ on the central meridian (blue) and ±45° longitudes (− green; + magenta).

Chapter 5

Concluding Remarks

This chapter concludes this dissertation with a summary of the research contributions, and a perspective on the near future. The author will refrain from speculating on distant possibilities, and stick to an appraisal of strategies possible with the current state of knowledge.

5.1 Summary

This dissertation is concerned with the measurement and interpretation of travel-time shifts in the context of time-distance helioseismic measurement of meridional flow. To that end, this dissertation examines forward modeling in the ray approximation and the "center-to-limb" variation in the travel-time measurements of solar velocity data.

For accurate inversion of travel-time shifts to obtain flow velocities, the travel-time shifts have to be accurately interpreted or forward modeled. The forward modeling is done in the ray-theoretic approximation, whereby the travel times are interpreted as the travel times of waves propagating according to the rules of ray geometry, and non-vanishing travel-time shifts of counter-propagating waves result from oppositely Doppler shifted waves in the presence meridional flow. In this work, the ray-theoretic travel times in the presence of different meridional flow models are compared with travel times derived from time-distance analysis of two independent three-dimensional acoustic wave simulation data perturbed by the same meridional flow models. The full deep-focus scheme is used for the first time to measure meridional flow induced travel-time shifts on phase-speed filtered simulation data. A systematic effort is made for the first time in the context of meridional flow to incorporate some of the physics

of the simulations into the ray-theoretic computations. The investigation could not establish the adequacy of ray theory for interpreting meridional flow induced travel-time shifts. Since the sensitivity kernel needed for accurate inversions is derived from a robust forward model, the work in this dissertation cautions against an unchary acceptance of the inversion results using ray kernels.

Spherical harmonic coefficient time series (up to degree $l = 300$) from the HMI global helioseismology pipeline are used to reconstruct 2 years and 11 months of solar velocity datacube. A new constant chord-length deep-focus technique is devised to make more effective use of the method of confining the time-distance measurements along the central meridian and equator to a narrow strip. The $\delta\tau_{\rm ns}$ and $\delta\tau_{\rm we}$ measurements with this new technique also show the "center-to-limb" effect. Baldner and Schou (2012) provide a plausible physical explanation for this effect: convective turbulence near the solar surface results in an observed height dependent, and therefore a heliocentric angle dependent phase shift. This heliocentric angle dependence is tested in this dissertation by making time-distance measurements on narrow strips along the $\pm 45^\circ$ longitudes and the $\pm 45^\circ$ latitudes and comparing the results to a model center-to-limb phase shift function. The expectation is that these regions of the observed solar disk will be less sensitive to a heliocentric angle dependent center-to-limb variation. The test is unsuccessful due to the inadequate signal-to-noise ratio of the travel-time shift measurements. However, the methods devised here point the way to new and more effective tests. In the future the "strip" method may also be used to study meridional flow variation with longitude.

5.2 Strategies

It would be stating the obvious that more work needs to be done. Perhaps, that is the whole point of pursuing a doctorate and writing a dissertation: to have one's work cut out. Interpretation is an especially difficult task where errors can translate into significantly different meanings. In the case of measuring travel-time shifts the errors can lead to attributing different physical bases to the systematic errors, deciphering reversed flow at different latitudes or depths leading to a different count in the number of meridional circulation cells, and other undesirable effects.

A recapitulation of the problematic issues in this work may provide a point of departure: noise in the signal, inadequate kernels derived from ray theory, systematic

errors such as the "center-to-limb" effect, incomplete knowledge of physics of the Sun.

5.2.1 Noisy Travel Times

For starters, is there anything else that can be done to improve the signal-to-noise ratio of the measured travel-time shifts, other than phase-speed filtering, applying full deep-focus geometry, analyzing very long time series, and building superior instruments and computers of the future? According to Kholikov and Hill (2014) there is: high-m filtering. Their results show that filtering out the higher m acoustic modes yields cleaner cross-covariance functions for time-distance measurements in the north-south direction, especially at the higher latitudes.

Furthermore, one can calculate Gizon-Birch travel times (Gizon and Birch, 2004) which is robust with respect to noisy cross-covariances, instead of extracting travel times with a Gabor-wavelet fit. However, if one were to continue using Gabor wavelets, it was high time that this technology was upgraded to its latest version (Nigam et al., 2007). The new formula to estimate travel times generalizes the Gabor wavelet by taking into account the phase-speed filter, and also the horizontal component of the oscillation displacement signal, in addition to the radial component (the only component considered previously). The new formula also depends on the location of the two photospheric points being cross-correlated.

The noise covariance matrix for travel times is an important ingredient for forward modeling to estimate the noise characteristics of travel times, and ought to be calculated as outlined in Gizon and Birch (2004) but modified for the full deep-focus geometry. Knowledge of the noise covariance matrix is also required for the assignment of error bars to the inversion results.

5.2.2 From Rays to Waves

In Chapter 3, ray theory fell roughly 100 ms short of expectations. However, since the acoustic cut-off frequency is a model dependent "characteristic" quantity, the expectation that one ray theory will fit all is misguided. And here, as in all scientific endeavors, a "fit" will need to be qualified in no uncertain terms. Even if it were possible to derive ray theories for different simulations, one would still need to derive a *solar* ray theory that reflects the relevant solar physics. As solar physicists continue their studies with increasingly sophisticated tools, it is hoped that the simulations

will become more realistic and solar-like making it possible to derive a solar-like ray theory. This could then be used to derive the most realistic ray kernels that will lead to errors smaller than all the other preceding ray kernels.

Shallow plane geometry finite-wavelength kernels employing various approximations already exist. The approaches that have included wave effects are the *Born* approximation (Birch and Kosovichev, 2000), the *Rytov* approximation (Jensen and Pijpers, 2003), and the *Fresnel zone* approximation (Jensen et al., 2000). But these are not useful for perturbations at large depths where the acoustic modes become sensitive to the sphericity of the Sun. Still, it is worth mentioning that Birch and Gizon (2007) found a case involving f modes, where the ray kernel was a factor of two larger than the Born-approximation kernel, if only to demonstrate that differences do exist between the ray and wave "interpretation" of travel times. Bogdan (1997) showed that the energy density of a wave packet (comprising low radial order modes) was substantial away from the ray path, i.e., the wave packets travels along a "ray bundle". Thus perturbations located away from the ray path will influence travel times, resulting in a sensitivity kernel that has more dimensions than a ray kernel. This suggests that the next logical step in improving the accuracy of forward modeling involving deep meridional flows would be to derive a finite-wavelength kernel in the *spherical* geometry—a rather exacting task, as indicated by the single unpublished paper on the topic by Schlottmann and Kosovichev (2011) on arXiv. Since 2103 the author has heard of several people working on the problem, but has not found any publications other than the one mentioned.

5.2.3 Systematic Errors

Some systematic errors are easily avoided such as B_0-angle issues (due to the inclination of the solar equatorial plane with respect to the ecliptic; e.g., Howard and Harvey, 1970; Giles, 2000) by calculating averages over an integral number of years or by confining the computations to a time interval close to when the B_0-angle is zero. That is because the interpretation is clear and well established.

Other systematic errors such as the finite light travel time effect ought to exist but do not show up in the data-analysis, and the "center-to-limb" effect has a magnitude equal to the former effect but with the opposite sign (Duvall and Hanasoge, 2009). When this latter effect is "corrected" by subtracting $\delta\tau_{\rm we}$ along the equator from $\delta\tau_{\rm ns}$

along the central meridian, travel-time shifts measured in different observables and different instruments agree with one another (Zhao et al., 2012), and $\delta\tau_{\rm ns}$ exhibits behavior consistent with meridional circulation obeying the constraint of mass-flux conservation (Zhao et al., 2013). This broad level of consistency is taken as a sign that the correct "correction" procedure was applied, and Baldner and Schou (2012) attempted to construct a physical model that justifies the correction. This dissertation describes a method to test the validity of the mathematical model implied by the physical model of Baldner and Schou (2012). The results of the test are inconclusive due to the noise level of the measured signal.

Assuming for the moment that the mathematical model of the "correction" is correct regardless of the physical model, it is quite clear that the "correction" itself can undergo further correction. It was mentioned in Section 4.3.2 that the reason for confining the measurements and the longitudinal averaging to a narrow strip along the central meridian and the equator is that the coordinate geometry is different in the north-south and west-east directions. This presumably results in systematic differences, other than meridional flow, between $\delta\tau_{\rm ns}$ and $\delta\tau_{\rm we}$ for measurements near the limb where the respective geometries attain the maximal relative difference, thus introducing another kind of systematic error in the "corrected" travel-time shift. This can be prevented if the latitude-longitude coordinate system is rotated with respect to the solar disk in the plane of the disk. Thus before calculating $\delta\tau_{\rm we}$, the coordinate system is rotated so that the equator becomes the central meridian in the new coordinate system. The $\delta\tau_{\rm we}$ calculated in the new coordinate system is then subtracted from $\delta\tau_{\rm ns}$ calculated in the old coordinate system. In this way, there would be no need for confining strips and $\delta\tau_{\rm ns}$ can be corrected over the whole solar disk and averaged over all available longitudes resulting in increased signal-to-noise ratio and minimal systematic errors. Being able to rotate the coordinate system with respect to the solar disk will have the added benefit of permitting measurements of the "center-to-limb" effect along various angles with respect to the equator, i.e., along various diameters of the solar disk. These measurements will provide another test of the geometrical properties of the "center-to-limb" effect. The rotation of the coordinate system may be implemented as part of the spherical harmonic reconstruction algorithm such that the reconstructed images have the rotated coordinate system with phase-speed filtering carried out on the "rotated" coefficients.

Out of the discussion concerning the rotation of the coordinate system, a new

time-distance technique was born. The new method seeks to circumvent all center-to-limb variations by cross-correlating pixels along lines of constant heliocentric angle. T. L. Duvall, Jr. modified the spherical harmonic reconstruction code (cf. Section 4.2) to reconstruct images in a polar grid rather than a latitude-longitude grid, with the solar disk center at the center of the image. Three advantages follow from the new time-distance technique: it can test whether the "center-to-limb" effect in the solar data is a true center-to-limb phase variation; it can be modified to cross-correlate in directions perpendicular to the isolines, and thus enable a look at the "center-to-limb" effect along different diameters of the solar disk; it can naturally separate zonal (rotational) flows from meridional flows. This method is still in the works and the initial results show promise.

5.2.4 Inverse Problem

One cannot conclude a dissertation involving time-distance *helioseismology* without a few words on the inverse problem. While travel-time shift is an important diagnostic of meridional flow, what is desired in the end is flow velocity. Notwithstanding the importance of forward modeling, inversion techniques (cf. Gizon and Birch, 2005) are an integral part of the time-distance arsenal for obtaining three-dimensional maps of various physical quantities, in this case meridional flow velocity, in the solar interior. For sure, inversion results are as certain as the forward model used to derive the sensitivity kernel, but parallel efforts must be expended in the mutually beneficial development of forward models and inversion techniques. For an update on recent developments in inversion for local helioseismology the reader is referred to Jackiewicz et al. (2012).

Regardless of the sophistication achieved in inversion computations, helioseismologists still await a finite-wavelength kernel in spherical coordinates (cf. Section 5.2.2). This kernel will also need to account for the various filters and the full deep-focus geometry. The incorporation of the new kernel into a feasible inversion algorithm may prove to be non-trivial.

5.2.5 Interpretation Revisited

Between 1998 and 2001, S. D'Silva published three letters in The Astrophysical Journal, cautioning against playing fast and loose with the notion of travel time. In

time-distance computations the position of the peak of the envelope, or the position of one of the phase peaks, of a cross-covariance function is identified as the travel time of a wave packet between two spatially separated locations on the Sun. D'Silva (1998a) asserted that the peaks of the envelopes obtained by assuming that the envelope of the sum of the functions is the sum of the envelopes can lead to erroneous travel times. He then derived the conditions under which the envelope of a sum can be approximated to the sum of the individual envelopes so that the errors are minimal.

In D'Silva (1998b) "dispersion" is shown to adversely affect the computations of travel times of solar acoustic wave packets. Here "dispersion" is a dispersion in travel times experienced by a wave packet when the arrival times are not constant across the wave packet spectrum. When travel time is a nonlinear function of frequency, D'Silva (1998b) showed that as the width of the Gaussian spectrum is increased the envelope of the cross-covariance function can increasingly deviate from a Gaussian, and the envelope peak and phase peaks can shift, introducing additional challenges in computing travel times.

When individual cross-covariance functions are spatially averaged to improve the signal-to-noise ratio, it is tacitly assumed that the travel time of the averaged function is the average of the individual travel times. D'Silva (2001) showed that the phase travel time of the averaged signal is not equal to the average of the phase travel times. Instead, it is a solution to a nonlinear equation that depends on the amplitudes of the individual cross-covariance functions, which defeats the purpose of averaging.

The author has not seen any papers since the publication of these letters, that investigate the claims therein, to either confirm them or to dismiss them as negligible effects in the analysis of solar data. What other systematic errors could be lurking in time-distance computations due to these effects? To let these warnings go unheeded would be extremely poor strategy.

Appendix A

Colatitudinal and Radial Travel-Time Shifts

This appendix is presented because Equation (2.43) in Giles (2000) for the travel-time shift due to radial flow, or the radial travel-time shift, is incorrect. This may be assessed from the fact that if the radial flow is uniform everywhere, then the travel-time shift due to the radial velocity should be zero, as counter-propagating rays will experience the same net flow; Equation (2.43) in Giles (2000) does not reflect that fact. The correct expression is derived below.

The travel-time shift between counter-propagating rays in the presence of flow is given by (Kosovichev, 1996)

$$\delta\tau = -2\int_{\Gamma_0} \frac{\mathbf{v}\cdot \mathrm{d}\mathbf{s}}{c^2}, \tag{A.1}$$

where $\mathbf{v}$ is the flow velocity, c is the sound speed, Γ_0 is the unperturbed ray path, and $\mathbf{s}$ is the displacement vector along the ray. For the purpose of this derivation, the ray path Γ_0 is bisected at the turning point, and the preceding half of the ray path is labeled Γ_1 and the following half is labeled Γ_2. Thus, Equation (A.1) can be rewritten as

$$\delta\tau = -2\int_{\Gamma_1} \frac{\mathbf{v}\cdot \mathrm{d}\mathbf{s}}{c^2} - 2\int_{\Gamma_2} \frac{\mathbf{v}\cdot \mathrm{d}\mathbf{s}}{c^2}, \tag{A.2}$$

and the differential displacement vector may now be written as

$$\mathrm{d}\mathbf{s} = \begin{cases} -\mathrm{d}\mathbf{r} + r\mathrm{d}\boldsymbol{\theta} & \text{for ray path } \Gamma_1 \\ \mathrm{d}\mathbf{r} + r\mathrm{d}\boldsymbol{\theta} & \text{for ray path } \Gamma_2 \end{cases} \tag{A.3}$$

Inserting Equation (A.3) into (A.2) one obtains

$$\delta\tau = -2\int_{\Gamma_1} \frac{\mathbf{v}\cdot(-\mathrm{d}\mathbf{r} + r\mathrm{d}\boldsymbol{\theta})}{c^2} - 2\int_{\Gamma_2} \frac{\mathbf{v}\cdot(\mathrm{d}\mathbf{r} + r\mathrm{d}\boldsymbol{\theta})}{c^2}, \tag{A.4}$$

which after gathering the common differentials becomes

$$\delta\tau = 2\left(\int_{\Gamma_1} \frac{\mathbf{v}\cdot\mathrm{d}\mathbf{r}}{c^2} - \int_{\Gamma_2} \frac{\mathbf{v}\cdot\mathrm{d}\mathbf{r}}{c^2}\right) - 2\int_{\Gamma_0} \frac{(\mathbf{v}\cdot\mathrm{d}\boldsymbol{\theta})r}{c^2}. \tag{A.5}$$

Decomposing the flow velocity into its colatitudinal and radial components:

$$\mathbf{v} = \mathbf{v}_\theta + \mathbf{v}_r, \tag{A.6}$$

and inserting into Equation (A.5), using $\mathbf{v}_\theta \cdot \mathrm{d}\mathbf{r} = \mathbf{v}_r \cdot \mathrm{d}\boldsymbol{\theta} = 0$, one obtains

$$\delta\tau = \delta\tau_r + \delta\tau_\theta = 2\left(\int_{\Gamma_1} \frac{\mathbf{v}_r\cdot\mathrm{d}\mathbf{r}}{c^2} - \int_{\Gamma_2} \frac{\mathbf{v}_r\cdot\mathrm{d}\mathbf{r}}{c^2}\right) - 2\int_{\Gamma_0} \frac{(\mathbf{v}_\theta\cdot\mathrm{d}\boldsymbol{\theta})r}{c^2}, \tag{A.7}$$

where the colatitudinal travel-time shift ($\delta\tau_\theta$) and the radial travel-time shift ($\delta\tau_r$) are as follows:

$$\delta\tau_\theta = -2\int_{\Gamma_0} \frac{(\mathbf{v}_\theta\cdot\mathrm{d}\boldsymbol{\theta})r}{c^2}, \tag{A.8}$$

$$\delta\tau_r = 2\left(\int_{\Gamma_1} \frac{\mathbf{v}_r\cdot\mathrm{d}\mathbf{r}}{c^2} - \int_{\Gamma_2} \frac{\mathbf{v}_r\cdot\mathrm{d}\mathbf{r}}{c^2}\right). \tag{A.9}$$

Bibliography

Aerts, C., Christensen-Dalsgaard, J., and Kurtz, D. W.: 2010, *Asteroseismology*, Springer

Baldner, C. S. and Schou, J.: 2012, *Astrophys. J., Lett.* **760**, L1

Basu, S. and Antia, H. M.: 2003, *Astrophys. J.* **585**, 553

Beckers, J. M.: 1978, in *Proc. Workshop on Solar Rotation*, p. 166, Catania: Univ. of Catania

Birch, A. C. and Gizon, L.: 2007, *Astron. Nachr.* **328**, 228

Birch, A. C. and Kosovichev, A. G.: 2000, *Sol. Phys.* **192**, 193

Bogdan, T. J.: 1997, *Astrophys. J.* **477**, 475

Braun, D. C. and Birch, A. C.: 2008, *Astrophys. J., Lett.* **689**, L161

Burtseva, O., Kholikov, S., and Hill, F.: 2008, **118**, 012080

Charbonneau, P.: 2010, *Dynamo Models of the Solar Cycle*, Living Rev. Solar Phys.

Chou, D.-Y. and Dai, D.-C.: 2001, *Astrophys. J., Lett.* **559**, L175

Choudhuri, A. R., Schüssler, M., and Dikpati, M.: 1995, *Astron. Astrophys.* **303**, L29

Christensen-Dalsgaard, J., W., D., Ajukov, S. V., Anderson, E. R., Antia, H. M., Basu, S., Baturin, V. A., Berthomieu, G., Chaboyer, B., Chitre, S. M., et al.: 1996, *Science* **272**, 1286

Claverie, A., Isaak, G. R., McLeod, C. P., van der Raay, H. B., and Roca Cortes, T.: 1979, *Nature* **282**, 591

Corbard, T. and Thompson, M.: 2002, *Sol. Phys.* **205**, 211

Couvidat, S. and Birch, A. C.: 2006, *Sol. Phys.* **237**, 229

Couvidat, S., Rajaguru, S., Wachter, R., Sankarasubramanian, K., Schou, J., and Scherrer, P. H.: 2012, *Sol. Phys.* **278**, 217

Deubner, F.-L.: 1975, *Astron. Astrophys.* **44**, 371

Deubner, F.-L. and Gough, D. O.: 1984, *Ann. Rev. Astron. Astrophys.* **22**, 593

Dikpati, M.: 2014, *Mon. Not. R. Astron. Soc.* **438**, 2380

Dikpati, M., Corbard, T., Thompson, M. J., and Gilman, P. A.: 2002, *Astrophys. J., Lett.* **575**, L41

Dikpati, M. and Gilman, P. A.: 2006, *Astrophys. J.* **649**, 498

Dikpati, M. and Gilman, P. A.: 2009, *Space Sci. Rev.* **144**, 67

D'Silva, S.: 1996, *Astrophys. J.* **469**, 964

D'Silva, S.: 1998a, *Astrophys. J., Lett.* **498**, L79

D'Silva, S.: 1998b, *Astrophys. J., Lett.* **499**, L211

D'Silva, S.: 2001, *Astrophys. J., Lett.* **547**, L81

D'Silva, S. and Duvall, Jr., T. L.: 1995, *Astrophys. J.* **438**, 454

Duvall, Jr., T. L.: 1979, *Sol. Phys.* **63**, 3

Duvall, Jr., T. L.: 1995, in *GONG 94: Helio- and Astero-Seismology from the Earth and Space*, Vol. 76 of *ASP Conference Series*, pp 465–474, Astronomical Society of the Pacific

Duvall, Jr., T. L.: 2003, in *Local and global helioseismology: the present and future*, Proceedings of SOHO 12/GONG+ 2002 Workshop, pp 259–262, ESA Publications Division

Duvall, Jr., T. L. and Hanasoge, S. M.: 2009, in *Solar-Stellar Dynamos as Revealed by Helio- and Asteroseismology*, Proceedings of SOHO 21/GONG 2008 ASP Conference Series, pp 103–109, Astronomical Society of the Pacific

Duvall, Jr., T. L. and Hanasoge, S. M.: 2013, *Sol. Phys.* **287**, 71

Duvall, Jr., T. L., Hanasoge, S. M., and Chakraborty, S.: 2014, *Sol. Phys.* **289**, 3421

Duvall, Jr., T. L. and Harvey, J. W.: 1983, *Nature* **302**, 24

Duvall, Jr., T. L., Jefferies, S. M., Harvey, J. W., and Pomerantz, M. A.: 1993, *Nature* **362**, 430

Duvall, Jr., T. L. and Kosovichev, A. G.: 2001, in *Recent Insights into the Physics of the Sun and Heliosphere: Highlights from SOHO and Other Space Missions*, Proceedings of IAU Symposium 203, pp 159–166, Astronomical Society of the Pacific

Giles, P. M.: 2000, *Ph.D. thesis*, Stanford University

Giles, P. M., Duvall, Jr., T. L., Scherrer, P. H., and Bogart, R. S.: 1997, *Nature* **390**, 52

Gizon, L. and Birch, A. C.: 2004, *Astrophys. J.* **614**, 472

Gizon, L. and Birch, A. C.: 2005, *Local Helioseismology*, Living Rev. Solar Phys.

Gizon, L., Birch, A. C., and Spruit, H. C.: 2010, *Ann. Rev. Astron. Astrophys.* **48**, 289

Gizon, L., Duvall, Jr., T. L., and Schou, J.: 2003, *Nature* **421**, 43

Goldreich, P. and Keeley, D. A.: 1977, *Astrophys. J.* **212**, 243

González Hernández, I., Howe, R., Komm, R., and Hill, F.: 2010, *Astrophys. J., Lett.* **713**, L16

González Hernández, I., Patrón, J., Bogart, R. S., and the SOI Ring Diagrams Team: 1998, in *Structure and Dynamics of the Interior of the Sun and Sun-like Stars*, Proceedings of SOHO 6/GONG 98 Workshop, pp 781–786, ESA Publications Division

Gough, D. O.: 1993, *Course 7: Linear Adiabatic Stellar Pulsation*, Astrophysical Fluid Dynamics, Elsevier Science Publishers, Les Houches, Session XLVII

Gough, D. O. and Hindman, B. W.: 2010, *Astrophys. J.* **714**, 960

Haber, D. A., Hindman, B. W., Toomre, J., Bogart, R. S., Larsen, R. M., and Hill, F.: 2002, *Astrophys. J.* **570**, 855

Hanasoge, S. M. and Duvall, Jr., T. L.: 2007, *Astron. Nachr.* **328**, 319

Hanasoge, S. M., Duvall, Jr., T. L., and Couvidat, S.: 2007, *Astrophys. J.* **664**, 1234

Hanasoge, S. M., Duvall, Jr., T. L., and Sreenivasan, K. R.: 2012, *Proc. Natl. Acad. Sci.* **109**, 11928

Hanasoge, S. M., Larsen, R. M., Duvall, Jr., T. L., DeRosa, M. L., Hurlburt, N. E., Schou, J., Roth, M., Christensen-Dalsgaard, J., and Lele, S. K.: 2006, *Astrophys. J.* **648**, 1268

Hartlep, T., Zhao, J., Kosovichev, A. G., and Mansour, N. N.: 2013, *Astrophys. J.* **762**, 132

Hartlep, T., Zhao, J., Mansour, N. N., and Kosovichev, A. G.: 2008, *Astrophys. J.* **689**, 1373

Hathaway, D. H.: 1996, *Astrophys. J.* **460**, 1027

Hathaway, D. H.: 2012a, *Astrophys. J.* **760**, 84

Hathaway, D. H.: 2012b, *Astrophys. J., Lett.* **749**, L13

Hathaway, D. H., Nandy, D., Wilson, R. M., and Reichmann, E. J.: 2003, *Astrophys. J.* **589**, 665

Hathaway, D. H. and Rightmire, L.: 2010, *Science* **327**, 1350

Hathaway, D. H., Williams, P. E., Dela Rosa, K., and Cuntz, M.: 2010, *Astrophys. J.* **725**, 1082

Hazra, G., Karak, B. B., and Choudhuri, A. R.: 2014, *Astrophys. J.* **782**, 93

Hill, F., Bolding, J., Toner, C., Corbard, T., Wampler, S., Goodrich, B., Goodrich, J., Eliason, P., and Hanna, K. D.: 2003, in *Local and global helioseismology: the present and future*, Proceedings of SOHO 12/GONG+ 2002 Workshop, pp 295–298, ESA Publications Division

Hindman, B. W., Gizon, L., Duvall, Jr., T. L., Haber, D. A., and Toomre, J.: 2004, *Astrophys. J.* **613**, 1253

Howard, R.: 1979, *Astrophys. J., Lett.* **228**, L45

Howard, R. and Gilman, P. A.: 1986, *Astrophys. J.* **307**, 389

Howard, R. and Harvey, J.: 1970, *Sol. Phys.* **12**, 23

Howe, R., Christensen-Dalsgaard, J., Hill, F., Komm, R., Schou, J., and Thompson, M. J.: 2005, *Astrophys. J.* **634**, 1405

Ilonidis, S., Zhao, J., and Hartlep, T.: 2013, *Astrophys. J.* **777**, 138

Ilonidis, S., Zhao, J., and Kosovichev, A.: 2011, *Science* **333**, 993

Jackiewicz, J., Birch, A. C., Gizon, L., Hanasoge, S. M., Hohage, T., Ruffio, J.-B., and Švanda, M.: 2012, *Sol. Phys.* **276**, 19

Jackiewicz, J., Gizon, L., and Birch, A. C.: 2008, *Sol. Phys.* **251**, 381

Jefferies, S. M., Osaki, Y., Shibahashi, H., Duvall, Jr., T. L., Harvey, J. W., and Pomerantz, M. A.: 1994, *Astrophys. J.* **434**, 795

Jensen, J. M., Jacobsen, B., and Christensen-Dalsgaard, J.: 2000, *Sol. Phys.* **192**, 231

Jensen, J. M. and Pijpers, F. P.: 2003, *Astron. Astrophys.* **412**, 257

Jouve, L. and Brun, A. S.: 2007, *Astron. Astrophys.* **474**, 239

Kholikov, S. and Hill, F.: 2014, *Sol. Phys.* **289**, 1077

Kholikov, S., Serebryanskiy, A., and Jackiewicz, J.: 2014, *Astrophys. J.* **784**, 145

Kitchatinov, L. L.: 2013, in *Solar and Astrophysical Dynamos and Magnetic Activity*, Proceedings of IAU Symposium 294, pp 399–410, International Astronomical Union

Kitchatinov, L. L. and Olemskoy, S. V.: 2011, *Mon. Not. R. Astron. Soc.* **411**, 1059

Komm, R., González Hernández, I., Hill, F., Bogart, R., Rabello-Soares, M. C., and Haber, D. A.: 2013, *Sol. Phys.* **287**, 85

Komm, R., R., H., Hill, F., González Hernández, I., Toner, C., and Cobard, T.: 2005, *Astrophys. J.* **631**, 636

Komm, R. W., Howard, R. F., and Harvey, J. W.: 1993, *Sol. Phys.* **147**, 207

Kosovichev, A. G.: 1996, *Astrophys. J., Lett.* **461**, L55

Kosovichev, A. G.: 2011, in *The Pulsations of the Sun and the Stars*, Lecture Notes in Physics, pp 3–84, Springer

Kosovichev, A. G. and Duvall, Jr., T. L.: 1997, in *Solar Convection and Oscillations and their Relationship*, Proceedings of SCORe'96 Workshop, pp 241–260, Kluwer Academic Publishers

Kosovichev, A. G., Duvall, Jr., T. L., and Scherrer, P. H.: 2000, *Sol. Phys.* **192**, 159

Küker, M. and Stix, M.: 2001, *Astron. Astrophys.* **366**, 668

Larson, T. and Schou, J.: 2011, **271**, 012062

Leibacher, J. and Stein, R. F.: 1971, *Astrophys. Lett.* **7**, 191

Leighton, R. B.: 1960, in *Aerodynamic Phenomena in Stellar Atmospheres*, Proceedings of IAU Symposium 12, pp 321–325

Leighton, R. B., Noyes, R. W., and Simon, G. W.: 1962, *Astrophys. J.* **135**, 474

Miesch, M. S.: 2005, *Large-Scale Dynamics of the Convection Zone and Tachocline*, Living Rev. Solar Phys.

Miesch, M. S. and Toomre, J.: 2009, *Ann. Rev. Fluid Mech.* **41**, 317

Nandy, D., Muñoz-Jaramillo, A., and Martens, P. C. H.: 2011, *Nature* **471**, 80

Nigam, R., Kosovichev, A. G., and Scherrer, P. H.: 2007, *Astrophys. J.* **659**, 1736

Parker, E. N.: 1955, *Astrophys. J.* **122**, 293

Pipin, V. V. and Kosovichev, A. G.: 2011, *Astrophys. J.* **738**, 104

Racine, É., Charbonneau, P., Ghizaru, M., Bouchat, A., and Smolarkiewicz, P. K.: 2011, *Astrophys. J.* **735**, 46

Rädler, K.-H.: 2007, in *Magnetohydrodynamics: Evolution of Ideas and Trends*, Fluid Mechanics and its Applications, pp 55–72, Springer

Rempel, M.: 2006, *Astrophys. J.* **647**, 662

Rhodes, Jr., E. J., Ulrich, R. K., and Simon, G. W.: 1977, *Astrophys. J.* **218**, 901

Roudier, T., Rieutord, M., Malherbe, J. M., Renon, N., Berger, T., Frank, Z., Prat, V., Gizon, L., and Švanda, M.: 2012, *Astron. Astrophys.* **540**, A88

Rüdiger, G.: 1989, *Differential Rotation and Stellar Convection: Sun and Solar-type Stars*, The Fluid Mechanics of Astrophysics and Geophysics, Gordon and Breach Science Publishers

Schad, A., Timmer, J., and Roth, M.: 2011, *Astrophys. J.* **734**, 97

Schad, A., Timmer, J., and Roth, M.: 2012, *Astron. Nachr.* **333**, 991

Schad, A., Timmer, J., and Roth, M.: 2013, *Astrophys. J., Lett.* **778**, L38

Scherrer, P., Bogart, R. S., Bush, R. I., Hoeksema, J. T., Kosovichev, A. G., Schou, J., Rosenberg, W., Springer, L., Tarbell, T. D., Title, A., et al.: 1995, *Sol. Phys.* **162**, 129

Scherrer, P. H., Schou, J., Bush, R. I., Kosovichev, A. G., Bogart, R. S., Hoeksema, J. T., Liu, Y., Duvall, T. L., Zhao, J., Title, A. M., Schrijver, C. J., Tarbell, T. D., and Tomczyk, S.: 2012, *Sol. Phys.* **275**, 207

Schlottmann, R. B. and Kosovichev, A. G.: 2011, arXiv:1105.4619v2 [astro-ph.SR]

Schou, J.: 2003, *Astrophys. J., Lett.* **596**, L259

Schou, J. and Bogart, R. S.: 1998, *Astrophys. J., Lett.* **504**, L131

Schou, J., Scherrer, P. H., Bush, R. I., Wachter, R., Couvidat, S., Rabello-Soares, M. C., Bogart, R. S., Hoeksema, J. T., Liu, Y., Duvall, T. L., et al.: 2012, *Sol. Phys.* **275**, 229

Snodgrass, H. B. and Dailey, S. B.: 1996, *Sol. Phys.* **163**, 21

Spiegel, E. A. and Zahn, J.-P.: 1992, *Astron. Astrophys.* **265**, 106

Spruit, H. C.: 2011, in *The Sun, the Solar Wind, and the Heliosphere*, IAGA Special Sopron Book Series, pp 39–49, Springer

Steenbeck, M., Krause, F., and Rädler, K.-H.: 1966, *Z. Naturforsch., A* **21**, 369

Stein, R. F. and Norlund, Å.: 2001, *Astrophys. J.* **546**, 585

Stix, M.: 1987, in *The internal solar angular velocity: Theory, observations and relationship to solar magnetic fields*, Proceedings of the Eighth Summer Symposium, Sunspot, NM, Aug. 11-14, 1986, pp 329–342, D. Reidel Publishing Co.

Stix, M.: 2004, *The Sun: An Introduction*, Springer, 2nd edition

Švanda, M., Zhao, J., and Kosovichev, A. G.: 2007, *Sol. Phys.* **241**, 27

Topka, K., Moore, R., LaBonte, B. J., and Howard, R.: 1982, *Sol. Phys.* **79**, 231

Ulrich, R. K.: 1970, *Astrophys. J.* **162**, 993

Ulrich, R. K.: 2010, *Astrophys. J.* **725**, 658

van Ballegooijen, A. A. and Choudhuri, A. R.: 1988, *Astrophys. J.* **333**, 965

Vorontsov, S. V., Christensen-Dalsgaard, J., Schou, J., Strakhov, V. N., and Thompson, M. J.: 2002, *Science* **296**, 101

Wang, Y.-M., Nash, A. G., and Sheeley, Jr., N. R.: 1989, *Science* **245**, 712

Woodard, M.: 2000, *Sol. Phys.* **197**, 11

Woodard, M., Schou, J., Birch, A. C., and Larson, T. P.: 2013, *Sol. Phys.* **287**, 129

Zhao, J.: 2007, *Astrophys. J., Lett.* **664**, L139

Zhao, J., Bogart, R. S., Kosovichev, A. G., Duvall, Jr., T. L., and Hartlep, T.: 2013, *Astrophys. J., Lett.* **774**, L29

Zhao, J., Kaori, N., Bogart, R. S., Kosovichev, A. G., and Duvall, Jr., T. L.: 2012, *Astrophys. J., Lett.* **749**, L5

Zhao, J. and Kosovichev, A. G.: 2004, *Astrophys. J.* **603**, 776

Zhao, J., Kosovichev, A. G., and Sekii, T.: 2010, *Astrophys. J.* **708**, 304